Direct Evidence for Weak Flavour Mixing with the Sudbury Neutrino Observatory

by

Mark Guy Boulay

A thesis submitted to the Department of Physics

in conformity with the requirements for

the degree of Doctor of Philosophy

Queen's University

Kingston, Ontario, Canada

April, 2001

copyright ©Mark G. Boulay, 2001

to Lisa and Emma

Abstract

The Sudbury Neutrino Observatory is a large water Čerenkov neutrino detector with D_2O as the sensitive target material. SNO has been designed to provide sensitive tests for neutrino oscillations by measuring the flux and energy spectra of the solar ^{8}B neutrinos. In this thesis we present the first solar neutrino measurement in which the neutral current (NC) and charged current (CC) reactions are independently determined. The ^{8}B solar neutrino fluxes as measured with the charged current, elastic scattering, and neutral current reactions were found to be

$$\begin{aligned}
\Phi_{CC} &= 1.61\ ^{+0.08}_{-0.08}\ \text{(stat)}\ ^{+0.15}_{-0.15}\ \text{(syst)}\ \pm 0.10\ \text{(theor)} \times 10^6 \text{cm}^{-2}\text{sec}^{-1}, \\
\Phi_{ES} &= 2.13\ ^{+0.36}_{-0.38}\ \text{(stat)}\ ^{+0.19}_{-0.19}\ \text{(syst)}\ \pm 0.02\ \text{(theor)} \times 10^6 \text{cm}^{-2}\text{sec}^{-1}, \\
\Phi_{NC} &= 6.74\ ^{+0.79}_{-0.80}\ \text{(stat)}\ ^{+0.91}_{-0.88}\ \text{(syst)}\ \pm 0.40\ \text{(theor)} \times 10^6 \text{cm}^{-2}\text{sec}^{-1}.
\end{aligned}$$

We have thus found direct evidence for neutrino oscillations since the solar neutrino fluxes measured with the CC and NC reactions are different. We have also found the solar neutrino flux measured with the NC reaction is consistent with the standard solar model prediction and that the measurements with the CC and ES reactions are consistent with measurements made by the Homestake and Super-Kamiokande experiments, respectively.

Statement of Originality

This work and the results presented herein are the original work of the author except as noted here. Usage of work other than the author's is appropriately cited in the text.

The Sudbury Neutrino Observatory is a large experiment with well over a hundred collaborators and has thus far spanned over a decade. In this thesis the ideas, analysis, and results presented are the sole work of the author with the following exceptions:

The results and discussion presented in chapter two are a review of the literature and experimental results available at the time of writing this work.

Chapter three presents an overview of the design and operation of the SNO detector. The detector design and operation are the work of the SNO collaboration. The author has contributed to detector construction through several months of on-site work installing and testing PMT cables. The author has also worked on development and installation of a real-time position sensor for the acrylic vessel neck and has worked on the development and deployment of the source manipulator system. The author also contributed to the operation of the detector by working on the deployment and data acquisition of several calibration sources as well operating the detector during ν data collection.

The remainder of the thesis consists of the body of the analysis developed by the author and is original work. This includes vertex reconstruction techniques, a study of neutron transport in SNO, energy calibration, data reduction, analysis of radioactive backgrounds and the solar neutrino signal analysis. An object oriented data analysis framework incorporating the above elements was developed by the author and is being used by the Queen's SNO group. The SNOMAN Monte-Carlo used in the analysis is the work of the SNO collaboration.

Acknowledgments

I would like to thank my advisor, Aksel Hallin, for his guidance throughout the course of my studies. His passion for the thrill of discovery has served as a source of inspiration and has made my years at Queen's interesting and fun.

I am also grateful to Art McDonald, whose grounded outlook and keen understanding of the big picture have been helpful.

I would also like to thank Barry Robertson, Fraser Duncan and Phil Harvey for many useful discussions. Thanks to my fellow graduate Bryce Moffat, and former graduate students from Queen's Chris Jillings, André Hamer and Richard Ford, without whose pioneering efforts on SNO this work would not have been possible. Thanks to Peter Skensved, who not only gave me the opportunity to become a better physicist by following his example, but has always made finding and using computing resourses at Queen's interesting.

I have benefited from many useful discussions with the faculty at Queen's; I am grateful to Mark Chen, Hamish Leslie, George Ewan, Hugh Evans, and Hay-Boon Mak. I have benefited from the work of and learned a great deal from many members of the SNO collaboration. Thanks to Nick West, John Simpson, Mike Dragowski, Josh Klein, Neil McCauley and many others.

Finally, thanks to Lisa for her love, patience, and support.

Contents

List of Figures

List of Tables

List of Acryonyms and Abbreviations

ADC	Analog to digital converter
ASIC	Application specific integrated circuit
AV	Acrylic vessel containing the D_2O
bkg	background
BUTT	Berkeley underwater test photomultiplier tubes
CC	Charged current
CNO	Carbon-nitrogen-oxygen nuclear fusion cycle
DAMN	Data Analysis Mask Number used in SNOMAN data reduction
d.o.f.	degrees of freedom used in χ^2 calculation
EGS	Electron-gamma shower particle transport code
ES	Elastic scattering (of neutrinos from electrons)
FEC	Front-end card
FORTRAN	Formula translation programming language
GEANT	Geometry and tracking Monte-Carlo system
GTID	Global trigger identification number
INCO	International Nickel Company
MC	Monte-Carlo calculation
MSW	Mikheyev-Smirnov-Wolfenstein matter-enhanced ν oscillations
NC	Neutral current
NECK tubes	Four PMTs in the AV neck
NHITs	Number of hit phototubes
OWL	Outward looking phototube
PDF	Probability distribution function
p.e.	photo-electron
pp	proton-proton solar fusion chain
PMT	Photomultiplier tube
PMTIC	PMT interface card
PSUP	PMT support structure
QSNO	Queen's analysis package for SNO
QUSN7	SNO custom electronics chip
R_{fit}	Reconstructed event radius
RSP	Energy calibration processor in SNOMAN
SNO	Sudbury Neutrino Observatory
SNOD	SNO discriminator chip
SNOINT	SNO charge integrator chip
SNOMAN	SNO Monte-Carlo and analysis software

SNU	Solar neutrino unit (10^{-36} interactions per target per second)
SM	Standard particle physics model
SSM	Standard solar model
TAC	Time to amplitude converter
XSNOED	X-windows based SNO event display
ZDAB	ZEBRA formatted bank for raw SNO data
ZEBRA	CERN's memory management package for FORTRAN

Chapter 1

Introduction

Nearly four decades ago, Ray Davis Jr. undertook an experiment to verify the process of nuclear energy generation in our Sun by directly observing the solar neutrino flux [1]. The experiment successfully measured the solar neutrinoflux with its first published results in 1968 and gave rise to the field of neutrino astrophysics. The experimental results were quantitatively in conflict with the predictions; the deficit in the measured flux compared to the predicted value of close to a factor of 3 has come to be known as the *Solar Neutrino Problem*. To date, a total of five solar neutrino experiments have published results which show that the experimentally observed neutrino fluxes are lower than the standard solar model value. Homestake, SAGE, and GALLEX [2, 3, 4] have measured the solar neutrino flux with radiochemical techniques with their first publications spanning the period 1968 to the early 1990's. In 1986 the Kamiokande detector, originally designed to search for proton decay was brought online to detect solar neutrinos in real-time through neutrino-electron scattering [5]. A much larger version of the original Kamiokande detector, Super-Kamiokande began operating in 1996. The latest measurement of the ^{8}B solar neutrino flux with the Super-Kamiokande detector is still less than the standard model predicted value [6]. Since the first experimental results with the Homestake detector, much effort has gone into explaining the deficit in the measured solar neutrino fluxes. The theory of neutrino oscillations in matter, explained by Mikheyev and Smirnov [7] in 1986 based on previous work by Wolfenstein [8] has come to be widely accepted. Super-Kamiokande has recently provided evidence for oscillation of atmospheric neutrinos [9].

The SNO detector was designed primarily as a high-precision solar neutrino detector capable of providing direct evidence for neutrino oscillations. SNO is the first solar neutrino experiment to seperately measure charged current (CC) and neutral current (NC) solar neutrino event rates, which allows a measurement of both the electron neutrino (ν_e) flux and the total neutrino flux. In this thesis we present results of the first production data taken with SNO and provide the first direct evidence for solar neutrino oscillations.

Chapter 2

The Solar Neutrino Problem

If we accept that the current experimental solar neutrino capture rates from the main neutrino detectors are correct to within their quoted uncertainties, then there must be a problem either with the standard solar model, or with the electroweak theory of particle physics [10]. The first section of this chapter briefly describes these two theories and their relation to the solar neutrino problem. The final section will outline the results of the current experimental measurements and how these relate to the solar neutrino problem.

2.1 Solar Neutrino Physics

2.1.1 The Standard Solar Model

The currently accepted theory describing the evolution of our Sun is known as the *standard solar model* (SSM). It is the culmination of decades of work by numerous researchers. Certain simplifying assumptions are made in the model [10]. It is assumed that hydrostatic equilibrium exists in the Sun; the outward pressures of photon and particle radiation are exactly matched by gravity. It is also assumed that the only method for changing abundances of certain elements in the interior of the Sun is by nuclear reactions, i.e. no diffusion of elements takes place. To extract parameters from the model, it is further assumed that the Sun is initially of homogeneous composition, and that energy is generated via hydrogen fusion. The model is then allowed to evolve in time, and constrained to agree with certain parameters, namely photon luminosity, mass, radius, oblateness, and age. Table 2.1, reproduced from Bahcall [10], shows these measured parameters along with some of the parameters extracted from the model. It is known that the energy in the Sun is produced by two classes of reactions, the proton-proton (pp) chain, and the carbon-nitrogen-oxygen (CNO) cycle. In the pp chain, two protons fuse to ultimately form helium. This chain is responsible for almost all of the energy generation in the Sun, as well as the majority of the neutrino flux. The main reactions in this chain are shown in table 2.2, adapted from [10]. Table 2.3 shows the reactions in the CNO cycle. Figure 2.1 shows the energy spectrum of solar neutrinos due to these various nuclear processes, extracted from the standard solar model [10].

This model is deemed to be accurate to within its quoted uncertainties, and is able to predict p and s-mode heliovibrations (vibrations on or near the Sun's surface) to high precision [10]. Several authors have shown that no solution to the solar neutrino problem can be found by adjusting parameters in the standard solar model or even by introducing non-standard astrophysical mechanisms into any reasonable solar model [10, 11].

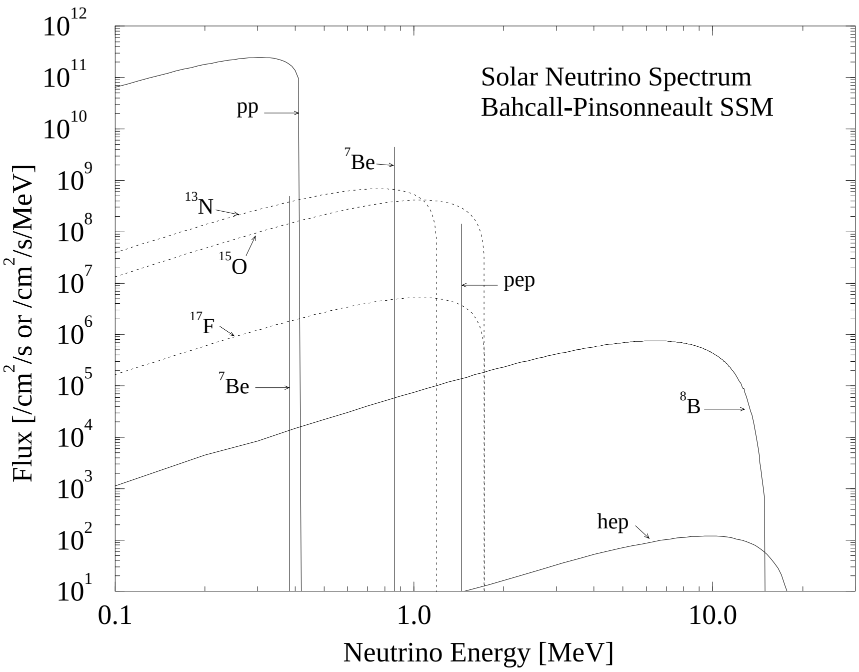

Figure 2.1: Solar neutrino spectrum predicted by the Bahcall-Pinsonneault standard solar model. The continuous spectra of solar neutrinos are given in units of [/cm^2/s/MeV], while the line sources are given in units of [/cm^2/s].

Parameter	Value
Photon luminosity ($L_\odot$)	3.86×10^{33} erg s^{-1}
Neutrino luminosity	0.023 $L_\odot$
Mass ($M_\odot$)	1.99×10^{23} g
Radius ($R_\odot$)	6.96×10^{10} cm
Oblateness [$R_{equatorial}/R_{polar}$ -1]	$\leq 2 \times 10^{-5}$
Effective (surface) temperature	5.78×10^{3} K
Moment of inertia	7.00×10^{53} g cm^2
Age	$\approx 4.55 \times 10^{9}$ years
Initial helium abundance by mass	0.27
Initial heavy element abundance by mass	0.020
Depth of convective zone	0.26 $R_\odot$ (0.015 $M_\odot$)
Central density	148 g cm^{-3}
Central temperature	15.6×10^{6} K
Central hydrogen abundance by mass	0.34
Neutrino flux from pp reaction	6.0×10^{10} cm^{-2}s^{-1}
Neutrino flux from ^{8}B decay	6×10^{6} cm^{-2}s^{-1}
Fraction of energy from pp chain	0.984
Fraction of energy from CNO cycle	0.016

Table 2.1: Table of physical characteristics of the Sun. Luminosity, mass, radius, oblateness, and age are measured values, while all others have been extracted from the standard solar model.

Reaction	**ν energy (MeV)**
$p + p \rightarrow {}^2\mathrm{H} + e^+ + \nu_e$ (pp)	≤ 0.424
or	
$p + e^- + p \rightarrow {}^2\mathrm{H} + \nu_e$ (pep)	1.422
${}^2\mathrm{H} + p \rightarrow {}^3\mathrm{He} + \gamma$	
${}^3\mathrm{He} + {}^3\mathrm{He} \rightarrow \alpha + 2p$	
or	
${}^3\mathrm{He} + {}^4\mathrm{He} \rightarrow {}^7\mathrm{Be} + \gamma$	
${}^7\mathrm{Be} + e^- \rightarrow {}^7\mathrm{Li} + \nu_e$	(90%) 0.861
	(10%) 0.383
${}^7\mathrm{Li} + p \rightarrow 2\alpha$	
or	
${}^7\mathrm{Be} + p \rightarrow {}^8\mathrm{B} + \gamma$	
${}^8\mathrm{B} \rightarrow {}^8\mathrm{Be}^* + e^+ + \nu_e$	< 15
${}^8\mathrm{Be}^* \rightarrow 2\alpha$	
or	
${}^3\mathrm{He} + p \rightarrow {}^4\mathrm{He} + e^+ + \nu_e$ (hep)	≤ 18.77

Table 2.2: Nuclear reactions in the proton-proton (pp) chain. The reactions labelled pp, pep and hep above correspond to the labelling in figure 2.1.

Reaction	ν energy (MeV)
${}^{12}\mathrm{C} + p \rightarrow {}^{13}\mathrm{N} + \gamma$	
${}^{13}\mathrm{N} \rightarrow {}^{13}\mathrm{C} + e^+ + \nu_e$	≤ 1.199
${}^{13}\mathrm{C} + p \rightarrow {}^{14}\mathrm{N} + \gamma$	
${}^{14}\mathrm{N} + p \rightarrow {}^{15}\mathrm{O} + \gamma$	
${}^{15}\mathrm{O} \rightarrow {}^{15}\mathrm{N} + e^+ + \nu_e$	≤ 1.732
${}^{15}\mathrm{N} + p \rightarrow {}^{12}\mathrm{C} + \alpha$	

Table 2.3: Nuclear reactions in the carbon-nitrogen-oxygen (CNO) cycle.

2.1.2 Neutrino Physics: The Weak Interaction

The results of the solar neutrino experiments suggest that the solution to the solar neutrino problem may involve a non-standard model of particle physics. The current standard electroweak model has three generations of massless neutrinos (ν_e, ν_μ, and ν_τ) grouped with their charged massive counterparts (e, μ, and τ).

Several non-standard particle physics solutions have been suggested, such as a non-zero neutrino magnetic moment, and neutrino decay. The simplest particle physics solution to the solar neutrino problem is known as the MSW effect, named for its discoverers Mikheyev, Smirnov, and Wolfenstein [7, 8]. In the standard electroweak model, eigenstates of the weak interaction are labelled according to "flavours". These three flavours are electron (e), muon (μ), and tau (τ). In the MSW theory, it is usually assumed that coupling occurs between the two lowest generation flavours, electron and muon neutrinos. The time evolution of two neutrino mass eigenstates ν_1 and ν_2 can be written in terms of the Hamiltonian operator $\mathcal{H}$

$$\mathcal{H}|\nu_1\rangle = |\nu_1\rangle E_1 \tag{2-1}$$

$$\mathcal{H}|\nu_2\rangle = |\nu_2\rangle E_2 \tag{2-2}$$

$$\tag{2-3}$$

where E_1 and E_2 are the energies of the mass eigenstates. In the general case the mass eigenstate of the neutrino is different from the flavour eigenstate, and we can write

$$|\nu_e\rangle = |\nu_1\rangle \cos\theta + |\nu_2\rangle \sin\theta \tag{2-4.a}$$

$$|\nu_f\rangle = -|\nu_1\rangle \sin\theta + |\nu_2\rangle \cos\theta \tag{2-4.b}$$

where

$\lvert\nu_e\rangle$	is the electron neutrino flavour eigenstate,
$\lvert\nu_f\rangle$	is a different flavour eigenstate, usually taken to be $\lvert\nu_\mu\rangle$,
$\lvert\nu_1\rangle, \lvert\nu_2\rangle$	are mass eigenstates with masses m_1 & m_2, and
θ	is the vacuum mixing angle.

An electron neutrino produced in the Sun at a time $t = 0$ will be in the definite flavour eigenstate

$$|\nu(t=0)\rangle = |\nu_e\rangle. \tag{2-5}$$

Since this was assumed not to be an eigenstate of $\mathcal{H}$, the Hamiltonian of the system, the neutrino wavefunction will undergo quantum mechanical oscillations. It can easily be shown that

$$\begin{aligned} |\nu(t)\rangle &= |\nu_1\rangle e^{-iE_1t}\cos\theta + |\nu_2\rangle e^{-iE_2t}\sin\theta && \text{(2-6.a)} \\ &= c_e(t)|\nu_e\rangle + c_f(t)|\nu_f\rangle, && \text{(2-6.b)} \end{aligned}$$

where we have used $e^{\frac{-i\mathcal{H}t}{\hbar}}$ as the time evolution operator and $c_e(t)$ and $c_f(t)$ are the relative probability amplitudes for the electron and non-electron flavour states.

The survival probability (the probability that an electron neutrino generated at

$t = 0$ remains an electron neutrino at a later time t) is given by

$$
\begin{aligned}
P(\nu_e \to \nu_e, t) &= |\langle \nu_e | \nu(t) \rangle|^2 && \text{(2-7.a)} \\
&= 1 - \sin^2(2\theta)\sin^2(\frac{(E_2 - E_1)t}{2}) && \text{(2-7.b)} \\
&= 1 - \sin^2(2\theta)\sin^2(\frac{\Delta m^2 t}{4E}), && \text{(2-7.c)}
\end{aligned}
$$

with

$$
\begin{aligned}
\Delta m^2 &= m_2^2 - m_1^2, && \text{(2-8.a)} \\
E &= \text{neutrino energy.} && \text{(2-8.b)}
\end{aligned}
$$

With this survival probability, the parameters Δm^2 and $\sin^2(2\theta)$ must lie in a fixed region for the ν_e flux to be suppressed; the only adjustable parameters in this model are these two mixing parameters. If however, we realize that by passing through matter, the Hamiltonian contains a term which singles out electron neutrinos, then this condition becomes less stringent. According to Wolfenstein, the Hamiltonian for neutrinos passing through matter is given by[1]

$$
\mathcal{H} = \begin{pmatrix} \frac{m_1^2\cos^2\theta + m_2^2\sin^2\theta}{2E} + \sqrt{2}G_F N_e & \frac{\Delta m^2}{2E}\cos\theta\sin\theta \\ \frac{\Delta m^2}{2E}\cos\theta\sin\theta & \frac{m_1^2\sin^2\theta + m_2^2\cos^2\theta}{2E} \end{pmatrix}, \tag{2-9}
$$

with

$$
\begin{aligned}
G_F &= \text{Fermi coupling constant,} \\
N_e &= \text{local electron density.}
\end{aligned}
$$

[1]The factor of $\sqrt{2}$ was incorrectly omitted in the original paper by Wolfenstein.

We note that $\mathcal{H}$ is asymmetric with respect to neutrino flavour since the only charged leptons in normal matter are electrons.

The strength of the coupling between neutrino flavours is related to N_e, the electron density of the matter through which the neutrino is traveling. Wolfenstein's original paper dealt with neutrinos passing through a slab of matter of constant density. Mikheyev and Smirnov realized that with the varying electron density profile in the Sun, the diagonal elements of this Hamiltonian become nearly degenerate for certain values of N_e, and resonant oscillations between neutrino flavours occur, thus suppressing the electron neutrino flux. Since these diagonal terms also have an energy dependence, this MSW mechanism has the ability to produce energy dependent electron neutrino flux suppressions.

Several authors have spent considerable effort integrating the propagation equation with the Hamiltonian of equation (2-9), for neutrinos produced in the Sun. An overview of MSW oscillations and recent calculations have been provided by Gonzalez-Garcia et al. [12, 13]. For various values of the two parameters, Δm^2 and $\sin^2(2\theta)$, different suppressions will lead to different expected count rates for the various neutrino detectors. In this way, the probability that these parameters lie in certain regions can be determined, by comparing these rates to experimental data. Figure 2.2, adapted from [14], shows one such MSW plot with the regions allowed after combining the measured solar neutrino rates from the Homestake, Sage, Gallex, and SuperKamiokande experiments, as well the electron recoil energy spectrum measured by SuperKamiokande. Also included in the figure is the Day-Night effect from SuperKamiokande, where neutrinos pass through different amounts of matter in the Earth during the day and night leading to different rate predictions.

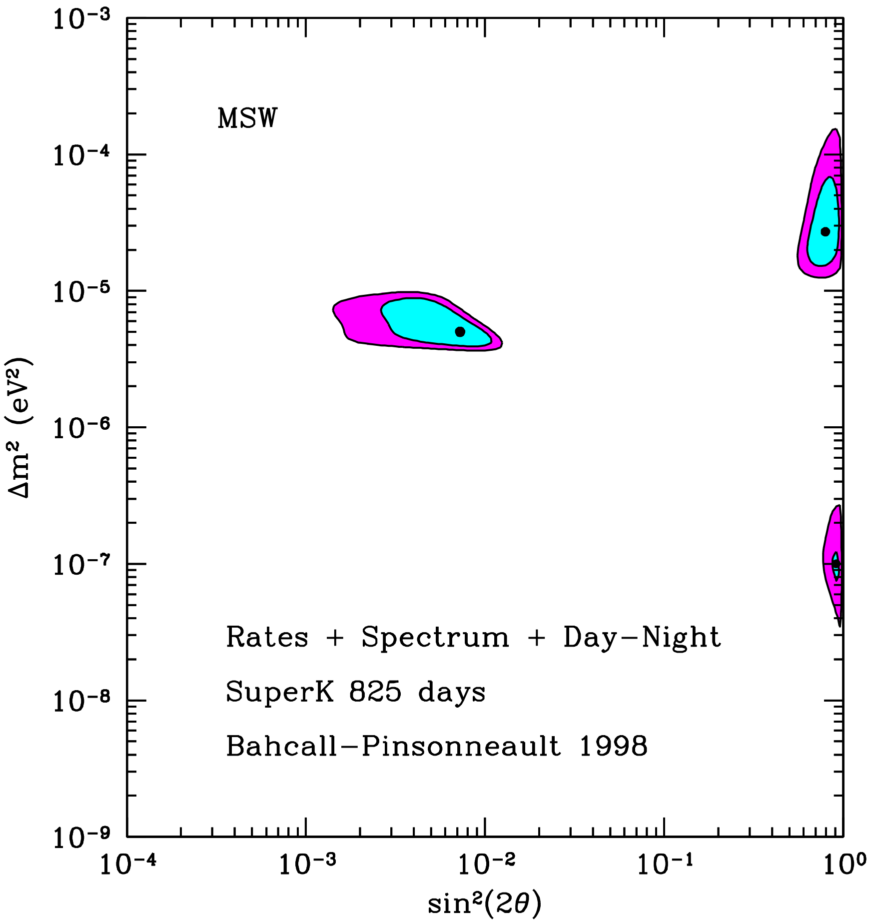

Figure 2.2: Allowed regions in the MSW plane. Figure adapted from [14]. The three allowed regions in the MSW plane (from left to right, clockwise) are known as the SMA, LMA, and LOW solutions. The contours correspond to 90% (blue) and 99% (pink) confidence intervals for each of the best-fit solutions, marked by dark circles.

2.2 Results of Solar Neutrino Experiments

The five experiments which have measured solar neutrino fluxes to date are Homestake, Kamiokande, Super-Kamiokande, SAGE, and GALLEX. Kamiokande is a light water Cerenkov detector which was succeeded by the Super-Kamiokande detector in 1996. SAGE and GALLEX both use ^{71}Ga as their sensitive detector. When quoting capture rates for neutrino detectors, the preferred unit is the SNU, or solar neutrino unit. One SNU is defined as 10^{-36} captures per target atom per second, which for the Homestake detector (with its 2.16×10^{30} ^{37}Cl target atoms) translates to 2.16×10^{-6} captures per second, or 0.19 captures per day. Tables 2.4, and 2.5 show the reaction used for each of these five experiments, their threshold energy, geographical locations, and results, along with the ratio of the experimentally observed flux of neutrinos to that predicted by the Bahcall-Pinsonneault standard solar model. There is currently no explanation other than MSW which can produce the energy dependent flux suppression required to account for the difference in these ratios [10, 11].

Experiment	Reaction	Threshold	Location
Kamiokande	$\nu_e e \rightarrow \nu_e e$	7.3 MeV	Japan
Super-Kamiokande	$\nu_e e \rightarrow \nu_e e$	5.5 MeV	Japan
Homestake	$\nu_e +^{37}\text{Cl} \rightarrow e^- + {}^{37}\text{Ar}$	0.814 MeV	USA
SAGE	$\nu_e{}^{71}\text{Ga} \rightarrow e^+ +^{71}\text{Ge}$	0.233 MeV	Russia
GALLEX	$\nu_e{}^{71}\text{Ga} \rightarrow e^+ +^{71}\text{Ge}$	0.233 MeV	Italy

Table 2.4: Experiments which have measured solar neutrinos.

Experiment	SSM	Experimental value	Exp/SSM
Kamiokande	$5.15\ (1.00^{+0.19}_{-0.14})$	$2.80 \pm 0.19 \pm 0.33$	$0.54 \pm 0.037 \pm 0.064$
Super-Kamiodande	$5.15\ (1.00^{+0.19}_{-0.14})$	$2.40 \pm 0.03^{+0.08}_{-0.07}$	$0.465 \pm 0.005^{+0.015}_{-0.013}$
Homestake	$7.7^{+1.2}_{-1.0}$	$2.56 \pm 0.16 \pm 0.16$	$0.33 \pm 0.02 \pm 0.02$
SAGE	129^{+8}_{-6}	$67.2^{+7.2}_{-7.0}{}^{+3.5}_{-3.0}$	$0.52^{+0.056}_{-0.054}{}^{+0.027}_{-0.023}$
GALLEX	129^{+8}_{-6}	$77.5 \pm 6.2\ {}^{+4.3}_{-4.7}$	$0.60 \pm 0.048\ {}^{+0.033}_{-0.036}$

Table 2.5: Results from experiments which have measured solar neutrino fluxes [2, 3, 4, 5, 6], as well as the predictions from the Bahcall-Pinsonneault standard solar model (BP98) [15]. The rates for the Kamiokande and Super-Kamiokande neutrino detectors are given in units of $10^6/\mathrm{cm}^2/\mathrm{sec}$, while all others are given in solar neutrino units (SNU's). The errors quoted for the standard model predictions are 1σ theoretical uncertainties; the errors quoted for the experimental results are 1σ statistical and systematic uncertainties.

Chapter 3

The SNO Detector

The Sudbury Neutrino Observatory has been constructed primarily for a high-precision measurement of the ^{8}B solar neutrino flux and spectrum. Detection of neutrinos is possible through the three reactions

$$\nu_e +^2 \mathrm{H} \longrightarrow p + p + e^- \tag{3-1}$$

$$\nu_x +^2 \mathrm{H} \longrightarrow \nu_x + p + n \tag{3-2}$$

$$\nu_x + e^- \longrightarrow \nu_x + e^- \tag{3-3}$$

where ν_x refers to any active neutrino flavour. The neutrino interaction signal in SNO is due to one or more electrons which produce Čerenkov photons; these photons are then detected with a phototube array. The charged current (CC) absorption of ν_e by deuterons (equation 3-1) results in an electron with an energy that is well correlated to the incoming neutrino energy and is thus suited to measuring the neutrino energy spectrum. This interaction also has a weak angular dependance which correlates the electron direction to the direction of the incoming neutrino. Since the CC reaction only occurs for electron neutrinos it allows for a measurement of the ν_e component of the neutrino flux. The neutral current (NC) reaction (equation 3-2) is equally sensitive to all neutrino flavours and is thus well suited to a measurement of the total neutrino flux. The neutron released in the NC reaction is detected in SNO when it is captured by a deuteron which results in the release of a 6.25 MeV γ-ray. This γ-ray will then interact in the heavy water and generate one or more energetic electrons. The elastic scattering (ES) of neutrinos from electrons (equation 3-3) is highly directional. The strength of this angular correlation can be used to seperate this signal from the other two. SNO is unique in that it can detect neutrinos through both charged and neutral current weak interactions, thus giving it the ability to unambiguously and directly search for neutrino oscillations, as well as precisely determine the neutrino oscillation parameters.

The detector is located at $46°28'30''$ N, $81°12'04''$ W in the INCO, Ltd., Creighton mine near Sudbury, Ontario, Canada. The center of the heavy water target is 2039 m below the surface in a cavity excavated from the 6800 foot level of the mine. The overburden of norite rock is equivalent to about 6000 meters of water shielding. At this depth the background from cosmic-ray muons is greatly reduced to about 3 muons per hour passing through the sensitive volume of the detector. The only other particles able to penetrate to this depth are neutrinos.

The lab is located approximately two kilometers from the mine shaft. All materials used in construction of the detector had to be transported through an elevator car of approximately 20 cubic meters down the mine shaft and trammed through the horizontal mining drift. Figure 3.1 shows the layout of the detector in the mine. In this chapter we provide a brief overview of the SNO detector. A detailed technical description of the detector and all of its subsystems has been published by the SNO collaboration [16].

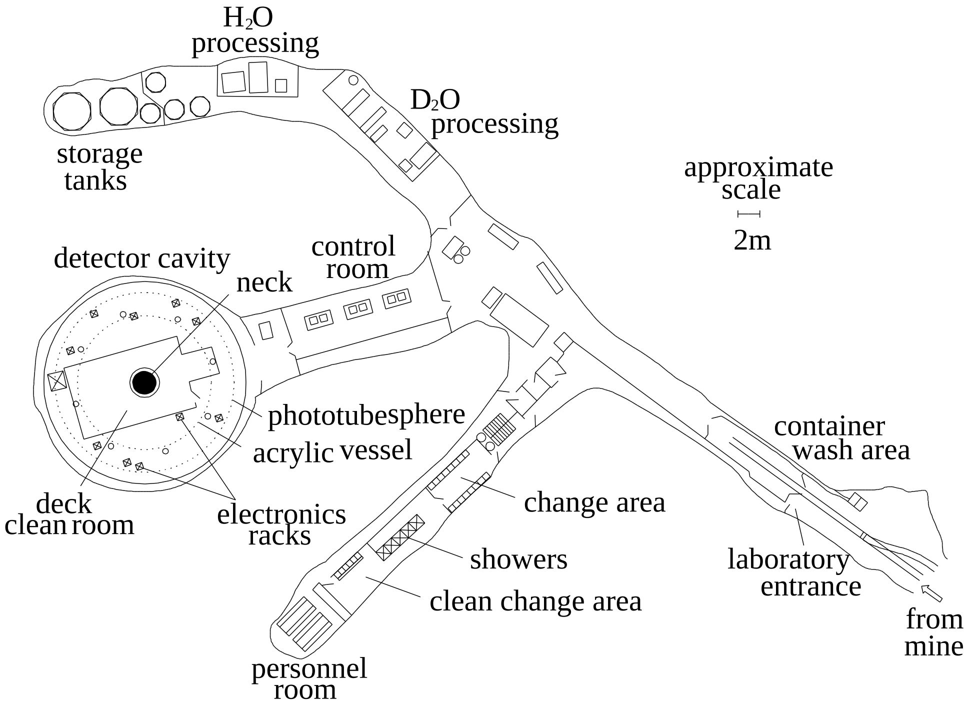

Figure 3.1: Layout of the laboratory and utility drifts.

3.1 SNO Detector

SNO is unique in that it uses a heavy water target in a spherical one kilotonne volume to detect solar neutrinos. This heavy water is contained in a transparent acrylic sphere 12 meters in diameter and 5.5 cm thick. The acrylic vessel was constructed by bonding together 122 seperate acrylic panels. To allow calibration devices to be deployed into the heavy water region of the detector, a 1.5 meter diameter acrylic chimney is located at the top of the acrylic sphere. The vessel is suspended from a deck structure by a set of ten rope loops as shown in figure 3.2. A stainless steel geodesic structure 17.8 m in diameter (shown in figure 3.3) surrounds the acrylic vessel and supports 9438 inward-looking photomultiplier tubes. The cavity in the rock is barrel shaped, 22 meters in diameter and 34 meters in height. This cavity is filled with ultrapure light water to provide support for the acrylic vessel and shielding from radioactivity in both the steel of the photomultiplier tube support structure and the rock wall.

The Čerenkov photons generated from solar neutrino interactions in the SNO detector are detected by a set of photomultiplier tubes fixed on the geodesic support structure. To maximize photon collection efficiency, a 27 cm diameter concentrator is mounted on each PMT (shown in figure 3.4) which increases the effective photocathode coverage from 31% to about 60%. The phototubes used in SNO are Hamamatsu R1408 PMT's. The glass envelopes of the phototubes have uranium and thorium concentrations of less than 40 ppb. The phototubes are operated with a bias voltage in the range 1700 V to 2100 V, producing a gain of approximately 2×10^7. The cables connecting the PMTs to the data acquisitions crates are all 32 meters in length to simplify signal timing, with a delay of 4.9 ns/m. The phototubes have been found to have an RMS timing resolution of 1.5 ns, in agreement with their specifications. The average noise rate in the phototubes in the SNO detector at 10° C is approximately 500 Hz.

The CC and NC reactions (equations 3-1 and 3-2) can occur only in the inner heavy water region, while the ES reaction (equation 3-3) can occur both in the heavy water and light water regions. In the analysis presented in this thesis we have selected an inner region of radius 540 cm with which to study the solar neutrino signals so that the contamination from background events is small.

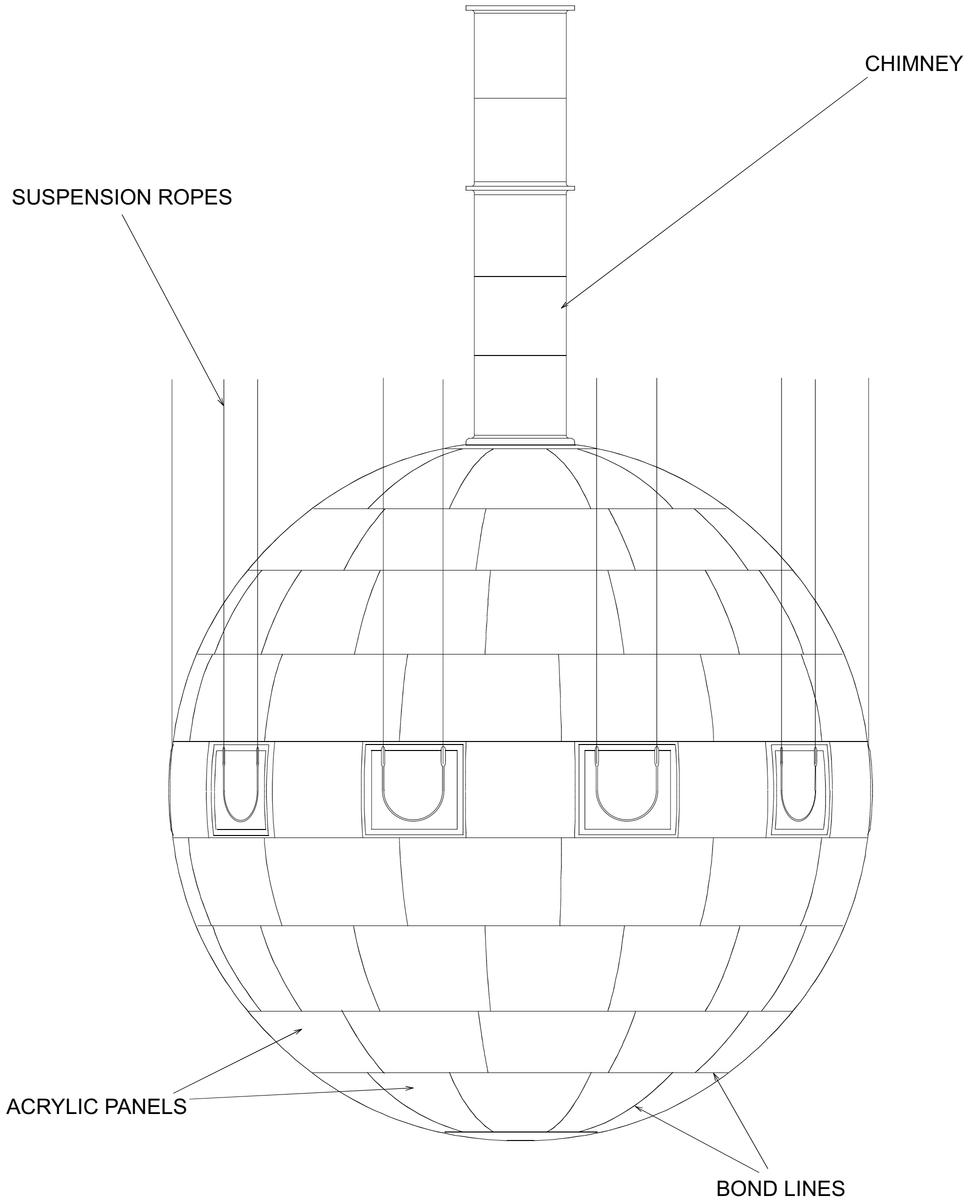

Figure 3.2: Acrylic heavy water containment vessel. The vessel was constructed by bonding together 122 acrylic tiles and is suspended from a deck by a set of ropes. The chimney allows access to the heavy water region for calibration.

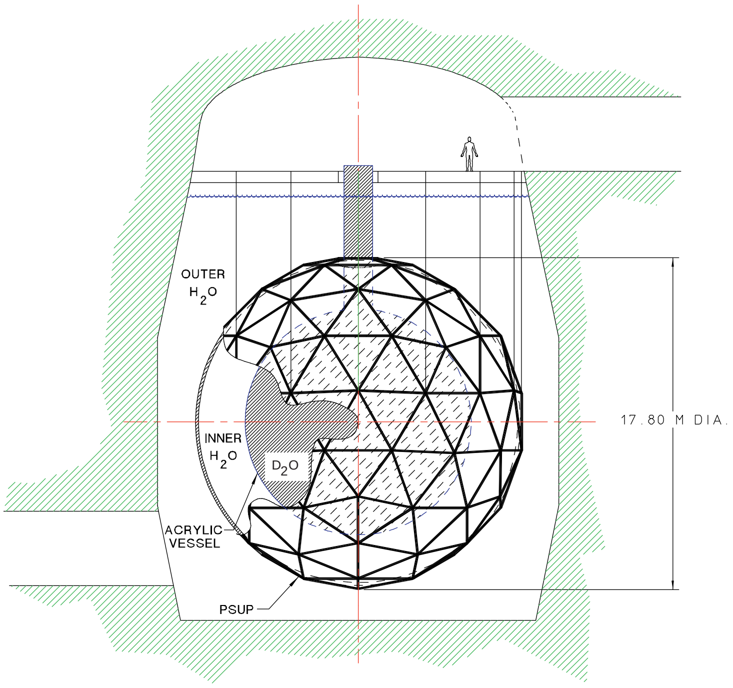

Figure 3.3: Photomultiplier tube support structure (PSUP). The PSUP holds the 9438 photomultiplier tubes in place. Ultrapure light water between the rock wall and the PSUP and between the PSUP and the inner D_2O volume provides shielding from radioactive backgrounds.

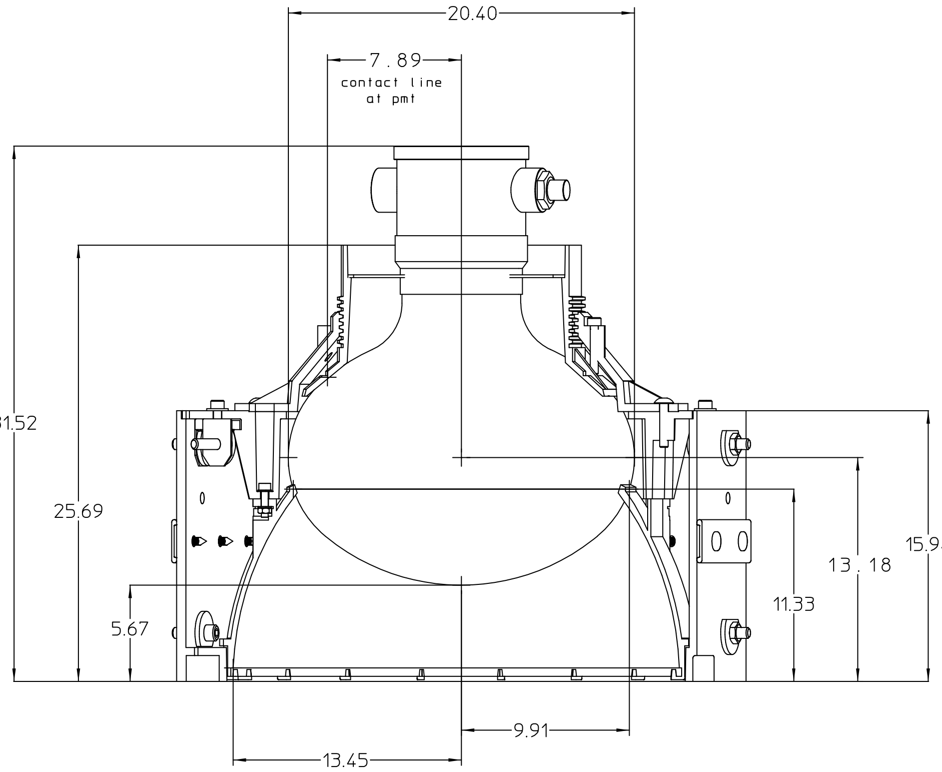

Figure 3.4: Phototube and reflector assembly. The Hamamatsu R1408 PMTs used in SNO have a diameter of approximately 20 cm. The concentrators mounted to each PMT increase the effective photocathode coverage of the detector from 31% to about 60%.

3.2 Electronics and Data Acquisition

The SNO electronics system is designed to provide sub-nanosecond time measurements and a wide dynamic range of charge measurements for all of the approximately 9500 PMTs. The trigger and data acquisition system is also designed to be effectively free of deadtime. Even though the solar neutrino signal rate is very low, the data acquisition system must be able to handle very high background rates and potential high rate bursts of events from supernovae.

The electronics subsystem occupies 19 crates, with each crate processing signals from 512 PMTs. A waterproof coaxial cable carries the signal from each PMT to a PMT interface card (PMTIC). Each of these cards receives signals from groups of 8 PMTs and is connected to a front end card (FEC), where the signals are further processed by application specific integrated circuits (ASICs). One FEC digitizes signals from 32 PMTs, and stores the results in a 4MB on-board memory buffer. The analog signal from the PMT is fed into a four channel discriminator chip (SNOD) where the leading edge is observed by a fast discriminator to determine accurately the time at which the phototube has fired. To allow for a large dynamic range in the measured charge deposited in the phototube, the current is split into two branches (with a ratio of approximately 1:16) and fed into two separate channels of an eight-channel charge integrator (SNOINT). Timing diagrams for the SNOD and SNOINT chips are shown in figure 3.5. A seperate chip set (QUSN7) provides analog memory for the time and charge signals from the SNOD and SNOINT chips, a time to amplitude converter (TAC), and logic for the SNO detector trigger system. This memory is 16-deep and samples the low and high gain channels of the SNOINT chip for early and late times so that there are four possible charge measurements. The

QUSN7 chip also receives the discriminator signal (from SNOD) which is used as the start of a time-measurement cycle and generates two trigger primitive signals. These signals are a short coincidence signal (roughly 20 ns) and a long coincidence signal (roughly 100 ns). Since the phototube array is approximately 17 m in diameter, direct photons from a Čerenkov event in the heavy water region can differ in travel times by as much as about 70 ns depending on the position in the detector. Thus the primary trigger resolving time is set to about 100 ns so that all direct photons in a single event can be counted toward a possible trigger. The 20 ns trigger window can be used to select events near the center of the heavy water volume. This allows for a lower hit threshold since only events in restricted volume will generate a trigger, thus reducing the overall event rate. The nominal operating mode of the SNO detector for the data set analyzed in this thesis is with the primary 100 ns trigger (NHIT_100_MED) set to about 17 hits. When the overlap of this 100 ns trigger pulse is greater than this number of hits, a global trigger signal (GT) is generated and sent back through the electronics system. The timing sequence shown in figure 3.5 and TAC are initiated for each channel on the leading edge of a signal from SNOD. The TAC is started when the PMT fires the discriminator and is stopped when a global trigger signal is detected or if the time elapsed is greater than an internal timeout, set to about 400 ns.

For each valid global trigger of the detector, the end result is a digitized time and three digitized charges (in 12-bit ADC units) for each PMT which has fired in the event. Also stored are a unique global trigger identification number (GTID), global trigger time as recorded by both a 10 Mhz and 50 Mhz clock, and a unique identifier for each PMT. These data will eventually be passed through an event builder and written to tape as ZDAB structures (the data structure used in the SNOMAN and

QSNO analysis software) for off-line analysis.

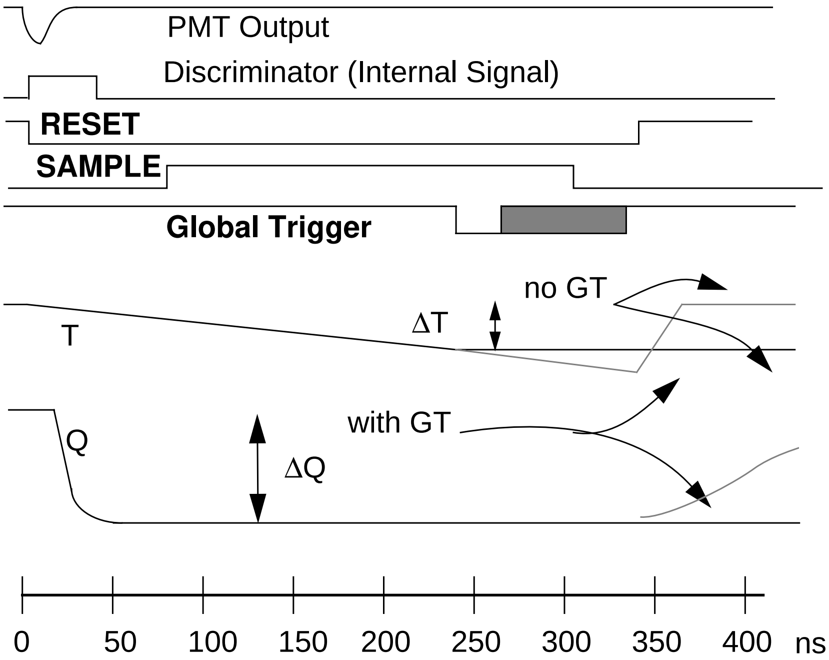

Figure 3.5: Timing diagram for the SNO electronics system.

3.3 Calibration Sources and Deployment System

The raw quantities measured with the SNO detector are phototube times and charges. A series of calibrations are required to take these signals and describe interactions in the detector in terms of event energy, position and direction for higher order analyses of solar neutrino signals. The primary calibration sources used in SNO, and those whose data were used in the production of this thesis are the laserball source, an ^{16}N source, and a ^{252}Cf source. The laserball source [17] consists of an N_2/dye laser and diffuser ball which provides a point source of isotropic monochromatic light in the detector. This source is used to determine the absolute PMT time and charge calibration and to accurately determine the optical properties of light and heavy water and the acrylic vessel, as well as the phototube angular response function. The ^{16}N source [18] is the primary source for calibration of Čerenkov events in SNO. ^{16}N decay results in the release of a 6.13 MeV γ-ray. The ^{16}N source delivers these γ-rays into the detector and tags them by signalling the presence of a β-particle which accompanies the γ-ray. ^{16}N source data are used to study vertex reconstruction of Čerenkov events in chapter 4 of this thesis. The absolute energy calibration and detector response to Čerenkov events at various positions in the detector are studied in chapter 6, and the effect of data reduction cuts on Čerenkov signals is studied in chapter 7. The ^{252}Cf is used to study neutron transport in SNO and is discussed in chapter 5.

A general purpose calibration source manipulator is employed by SNO to allow calibration sources to be deployed at many positions in the detector. The system allows source deployment at accurately known positions in two orthogonal planes in the D_2O. The source manipulator is a carriage restricted in a plane by two Vectran ropes as shown in figure 3.6 that run down the neck of the acrylic vessel and through pulleys on the carriage to fixed points on the inside of the acrylic vessel. A central rope connects directly to the carriage, thus allowing motion over a large portion of the constrained plane. A waterproof umbilical cord provides power and signal lines to the calibration sources. The manipulator system has an absolute position accuracy of 5 cm and can reach about 65% of the plane.

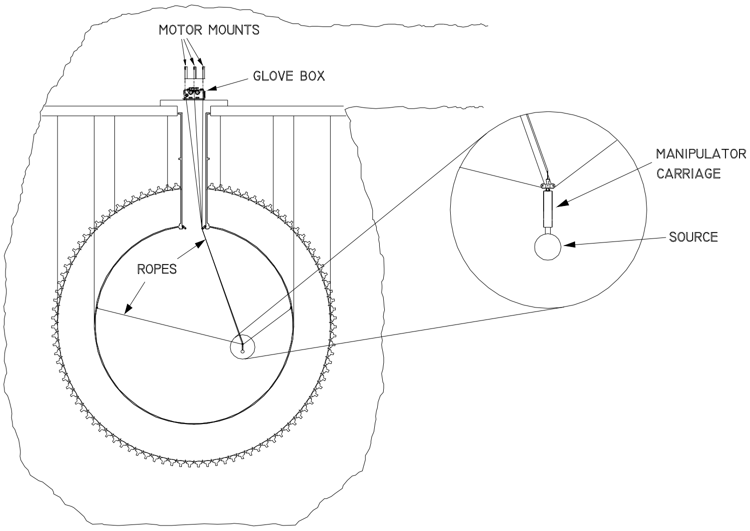

Figure 3.6: The calibration source manipulator system. A source carriage is controlled by a set of three ropes which allow it to be accurately positioned (to within about 5 cm) in one of two planes in the 12 m diameter spherical heavy water region. Calibration guide tubes allow calibration sources to be placed at many positions in the light water regions of the detector.

Chapter 4

Event Vertex Reconstruction

All measured signals in SNO are due to Čerenkov photons generated by energetic electrons. These electrons may have been produced directly by neutrino interactions or they may be secondary particles resulting from γ-rays or free neutrons in the detector. We define an *event* as any primary particle (e.g. ν, e^-, n, or γ-ray) which interacts and results in a trigger of the detector, where trigger is defined as any 17 PMTs firing with 100 ns of each other. To determine the position and direction of Čerenkov events in the SNO detector we apply vertex reconstruction techniques. This chapter describes event vertex reconstruction based on the phototube timing signals. We can then use the reconstructed event vertices to select a restricted fiducial volume for analysis which greatly reduces the background contamination. The direction of the Čerenkov events will also be used to identify and separate the solar neutrino signals.

4.1 Reconstructing Event Position

Vertex reconstruction is done based on the time at which inward looking PMTs have fired. For each event which triggers the SNO detector, the times and charges of all PMTs which have fired are stored. Figure 4.1 shows a typical ^{16}N event in which about 60 PMTs have fired. All PMTs which have fired in a window of approximately 420 ns have their charges and times digitized and are written to tape. Figure 4.2 shows the relative times at which photons have arrived at the phototubes for this event.

Figure 4.3 shows the vectors used to describe reconstructed event positions and directions. The vector $\vec{x}_{fit}$ is a vector from the detector origin to the fitted event vertex, $\vec{u}_{fit}$ is the reconstructed event direction, and θ_r is the angle between $\vec{x}_{fit}$ and $\vec{u}_{fit}$.

To reconstruct the event vertex from the timing information, we define a time residual for each PMT which fired in an event

$$
\begin{aligned}
T_{res} &= \text{Time-of-flight corrected PMT time} && \text{(4-1)}\\
&= T_{pmt} - T_{fit} - \frac{|\vec{x}_{fit} - \vec{x}_{PMT}|}{c_{avg}} && \text{(4-2)}
\end{aligned}
$$

with

$$T_{pmt} = \text{time at which PMT fired} \tag{4-3}$$

$$T_{fit} = \text{fitted event time} \tag{4-4}$$

$$\vec{x}_{fit} = \text{fitted event position} \tag{4-5}$$

$$\vec{x}_{PMT} = \text{phototube position} \tag{4-6}$$

$$c_{avg} = \text{mean photon group velocity} \tag{4-7}$$

We can then find the event vertex $\{T_{fit}, \vec{x}_{fit}\}$ for which the time residuals are minimized. Maximum likelihood techniques are used to find this best-fit vertex. A time residual histogram derived from a combination of Monte-Carlo calculations and laserball calibration timing data is used as the probability distribution function; this spectrum is shown in figure 4.4. The width of the primary peak in this spectrum is due to the intrinsic PMT timing resolution of about 1.5 ns. The other small peaks are due to phototube pre-pulsing and after-pulsing. Since the structure of the late peaks in this spectrum will depend on the event position and a detailed knowledge of scattering and reflections in the detector, we have approximated the distribution by a constant for time residuals greater than 15 ns, which is approximately the correct amplitude for the total amount of late light. For times which are earlier than the first pre-pulsing peak the spectrum is comprised only of random PMT firings. The distribution is scaled to approximately the dark PMT noise rate.

We define the likelihood function as

$$\mathcal{L}_{vertex} = \prod_{i=0}^{Nhits} P(T_{res_i}) \tag{4-8}$$

where $P(T_{res_i})$ is the probability distribution (as shown in figure 4.4) for PMT i.

We can take the logarithm of equation 4-8, and redefine the likelihood function as

$$\mathcal{L}_{vertex} = -2 \sum_{i=0}^{Nhits} log(P(T_{res_i})) \tag{4-9}$$

We can thus minimize equation 4-9 for a given event to find the most likely event vertex.

4.1.1 Scattered Light and Noise Hits

In all Čerenkov events in SNO some of the photons are scattered off of the direct line path between the event and the phototube. There are also approximately two random PMT hits per event due to the dark PMT noise rate of about 500 Hz. Some of the scattered light and noise hits are removed from the reconstruction algorithm by excluding PMTs which are out-of-time. The method used is to find the median PMT time in the event, and remove PMTs which are more than one half of one complete detector travel time (PSUP-PSUP) away from this. The actual time cut imposed is ±50 ns away from the median, which corresponds to about 1100 cm.

4.1.2 Finding the Global Minimum

The shape of the maximum likelihood surface is not smooth, as seen in figure 4.5. Many local minima are present which could severely affect our reconstruction accuracy. To avoid local minima, the following algorithm is used:
A seed vertex (in x, y, z, and t) is chosen at random within the volume of the SNO detector. This point is chosen from a uniform probability distribution defined over a sphere of radius 8 meters. The seed time is chosen from a uniform time distribution

between the median PMT time +/- about one half of one PSUP-PSUP travel time. Levenberg-Marquardt minimization is then used to find the minimum in the likelihood surface with this seed vertex. We denote

$$\vec{s_i} = \text{seed vertex i} \tag{4-10}$$

$$\vec{x_i} = \text{fit vertex for above seed} \tag{4-11}$$

$$\vec{x_s} = \text{intermediate best fit vertex} \tag{4-12}$$

$$\vec{x_g} = \text{fit vertex at global minimum} \tag{4-13}$$

$$N_{iter} = \text{number of iterations} \tag{4-14}$$

$$N_{same} = \text{number of times same minimum was found} \tag{4-15}$$

We then continue the process of choosing a random seed vertex ($\vec{s_i}$) and finding the corresponding $\vec{x_i}$. N_{same} is defined as the number of times we have converged to the same minimum (the intermediate best fit vertex $\vec{x_s}$) for different seed vertices if this minimum is indeed the lowest part of the likelihood function we have yet sampled. The fit is deemed to have converged when N_{same} reaches some large value. We hypothesize that

$$\lim_{N_{same}\to\infty} \vec{x_s} = \vec{x_g} \tag{4-16}$$

In practice, we have chosen the value $N_{same} = 6$ as a reasonable trade-off between finding the correct global minimum and available CPU cycles, which results in an average N_{iter} of about 15 for ^{16}N events.

Shown in figure 4.6 are the distributions of reconstructed events for the ^{16}N calibration source. The top frame shows all events, including ^{16}N decays in the gas transport umbilical. In the bottom frame only events in the inner decay chamber are selected by requiring a trigger signal. We can thus use event vertex reconstruction to localize events in the SNO detector.

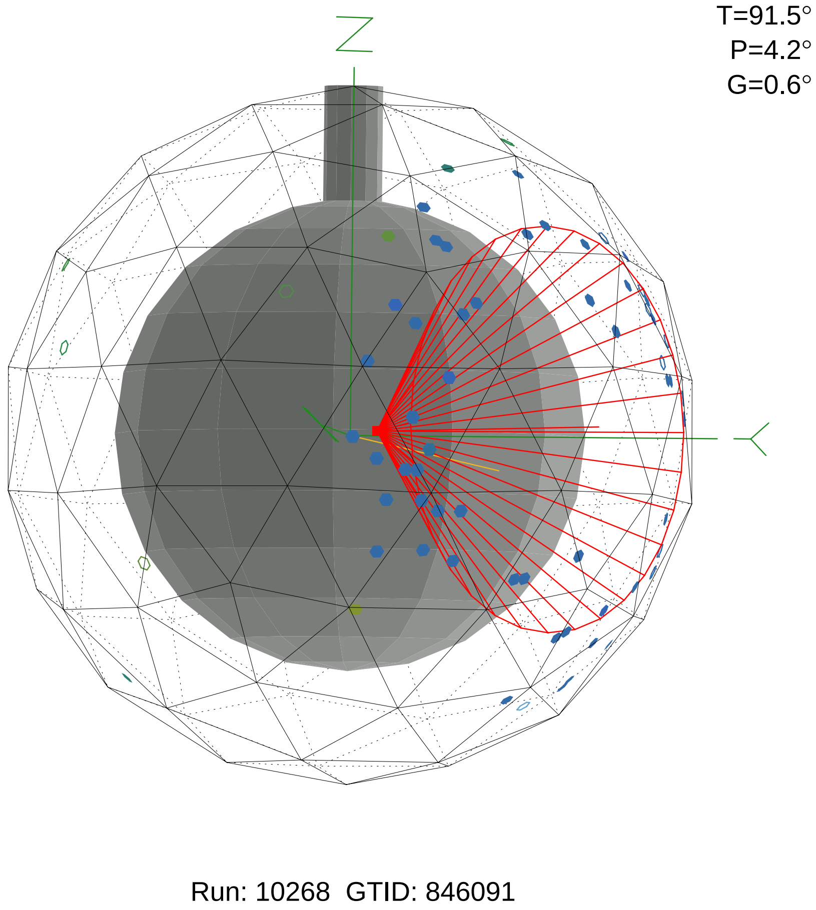

Figure 4.1: Hit pattern for a typical ^{16}N event from the XSNOED [19] event display. Shown are the positions on the PSUP of all PMTs which have fired in the event, as well as a cone from the fit vertex with the Čerenkov angle in D_2O.

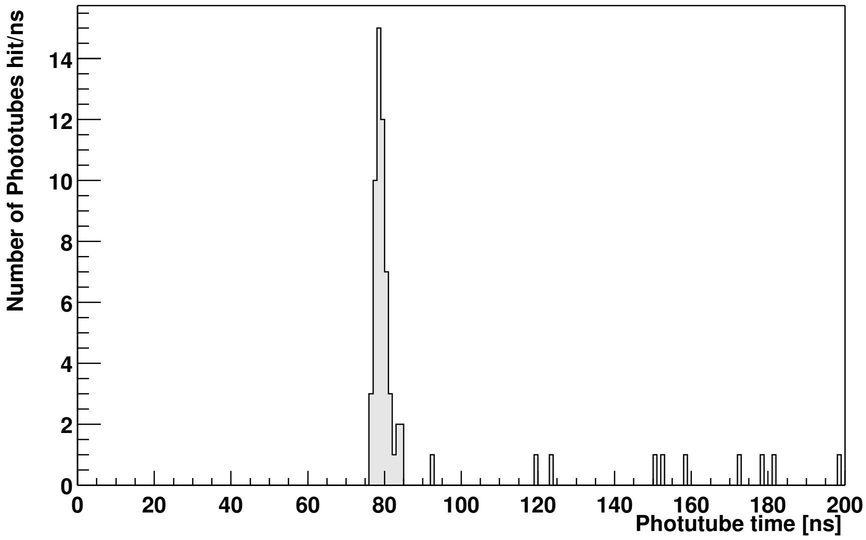

Figure 4.2: Timing spectrum for a typical ^{16}N event. Shown is the distribution of TAC times for each PMT which fired in the event.

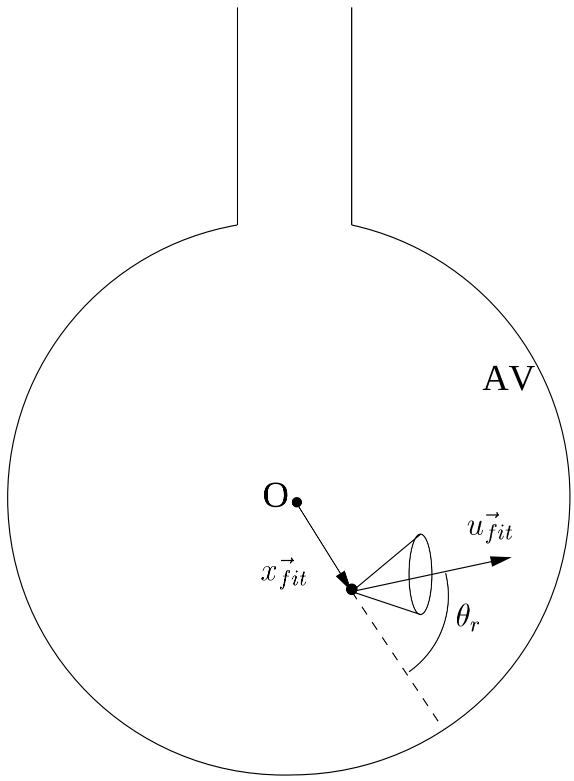

Figure 4.3: Definition of fitted vertex and direction. $\vec{x}_{fit}$ is the vector from the detector center to the fitted vertex, $\vec{u}_{fit}$ is the fit direction of the event, and θ_r is the angle between $\vec{x_{fit}}$ and $\vec{u_{fit}}$.

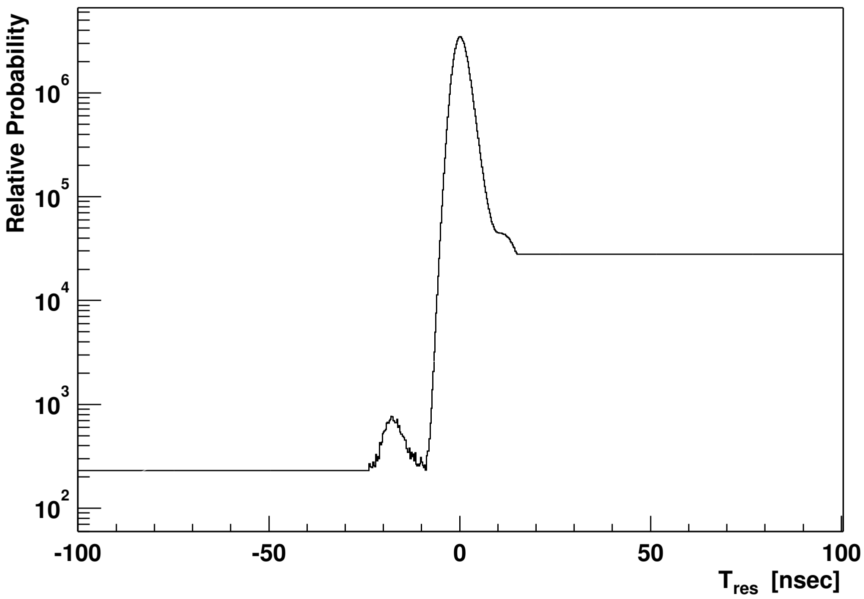

Figure 4.4: Time residual distribution used for maximum likelihood event vertex reconstruction.

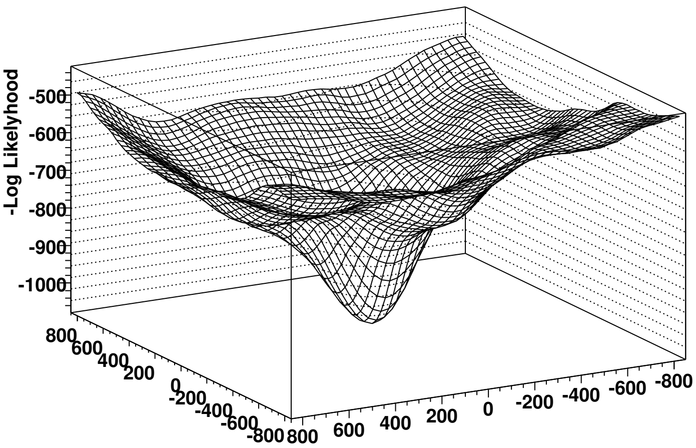

Figure 4.5: Likelihood surface for an ^{16}N event. Shown on the z-axis is the value of the likelihood function as a function of the x and y-coordinates (in cm) in the detector.

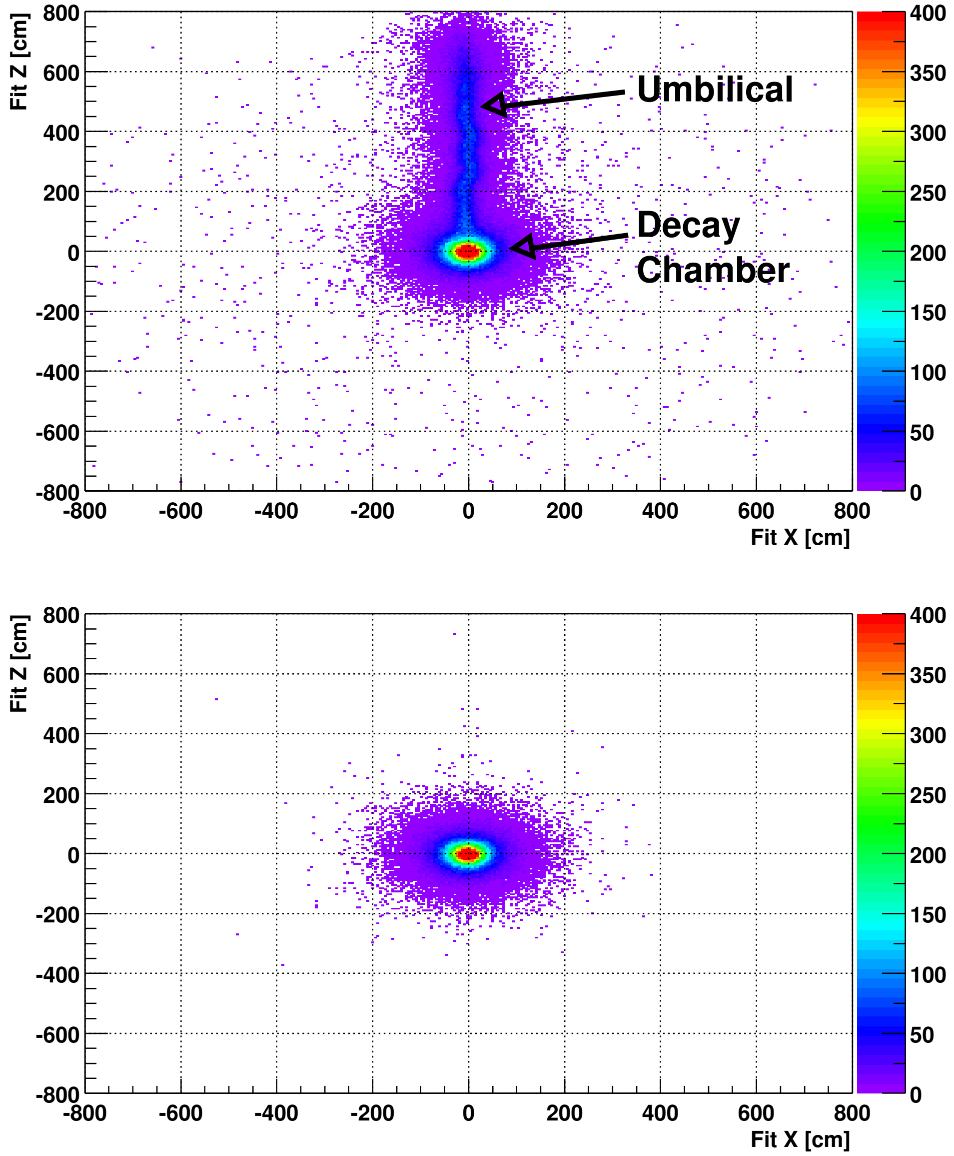

Figure 4.6: Reconstruction of ^{16}N events in SNO for the source at the detector center. All events are shown in the top frame where decays in the gas transporting umbilical can be seen. The bottom frame is for events where the β-tag is seen. Z is the vertical detector axis.

4.2 Reconstructing Event Direction

In addition to the event vertex, we need to determine the trajectory of the electron or γ-ray that produced the Čerenkov signal. The method used to estimate the direction of the primary electron in an event is to find that direction which best reproduces the angular distribution of the photons in the event. We use a model angular distribution based on a Monte-Carlo calculation for 8 MeV electrons. To avoid complications due to scattered light, a time window is selected such that only photons with

$$-10 < T_{res} < 10 \text{ ns} \tag{4-17}$$

(i.e. prompt photons) are selected. We define

$$\hat{u} = \text{event direction}(\theta_{fit}, \phi_{fit}) \tag{4-18}$$

$$\hat{p} = \text{direction to phototube i}(\theta_p, \phi_p) \tag{4-19}$$

and

$$\cos\theta_i = \hat{u} \cdot \hat{p} \tag{4-20}$$

$$\phi_i = \phi_p \tag{4-21}$$

With the vertex fixed at $\vec{X}_{fit}$ determined above, we define the direction likelihood as

$$\mathcal{L}_{dir} = \prod_{i=0}^{N_{win}} P_{dir}(\theta_i, \phi_i, \theta_{fit}, \phi_{fit})\Omega \tag{4-22}$$

where we have summed over in-time photons defined by equation 4-17 for the probability distribution $P_{dir}(\theta_i, \phi_i, \theta_{fit}, \phi_{fit})$ shown in figure 4.7 and Ω is a solid angle correction

$$\begin{aligned}
\Omega &= \frac{\cos\theta_{pmt}}{d_{pmt}^2}, && (4\text{-}23)\\
\cos\theta_{pmt} &= \text{phototube incident angle} && (4\text{-}24)\\
d_{pmt} &= \text{distance from fit vertex to phototube} && (4\text{-}25)
\end{aligned}$$

We apply the usual convention of redefining the likelihood function as

$$\mathcal{L}_{dir} = -2\sum_{i=0}^{N_{win}} log[P_{dir}(\theta_i, \phi_i, \theta_c, \phi_c)\Omega] \qquad (4\text{-}26)$$

We then minimize equation 4-26 to find the fit direction of the event, $(\theta_{fit}, \phi_{fit})$.

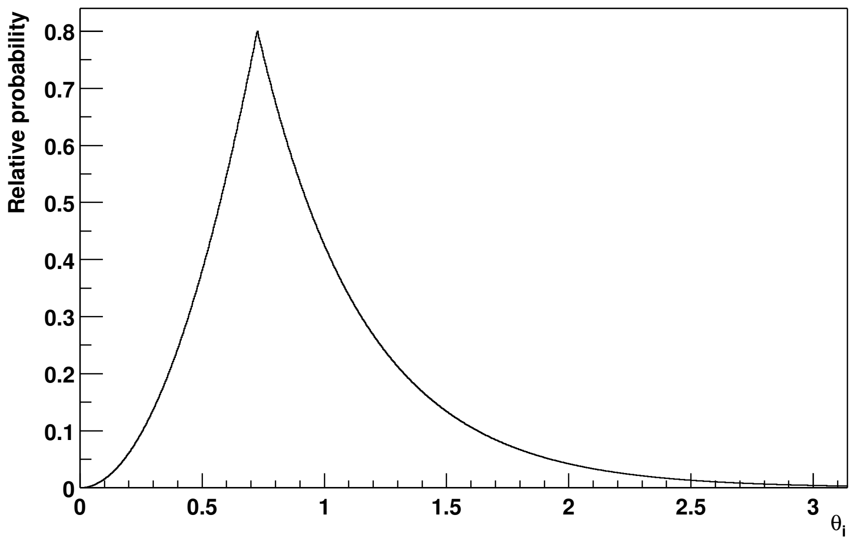

Figure 4.7: Direction probability function derived from a Monte-Carlo calculation for 8 MeV electrons. Shown is the distribution of photons versus θ_i; the distribution is flat in azimuthal angle ϕ_i. The peak at $\theta_i = 0.72$ corresponds to the Čerenkov angle in D_2O. Scattering of the electron smears the photon direction about the mean Čerenkov angle.

4.3 Reconstruction Resolution

The uncertainties in fitted position and direction of an event are required to determine the systematic uncertainties in the solar neutrino analysis. In this section we define fitter vertex and resolution functions and determine the function parameters with Monte-Carlo calculations. In section 4.4 ^{16}N calibration data are used to extract the uncertainties in the response function parameters.

4.3.1 Vertex Resolution

A position resolution function can be defined as

$$R(x) = \frac{1-\alpha_e}{\sqrt{(2\pi)}\sigma_p} \exp\left[-\frac{1}{2}\left(\frac{x-\mu_p}{\sigma_p}\right)^2\right] + \frac{\alpha_e}{2\tau_p} \exp\left[\frac{-|x-\mu_p|}{\tau_p}\right] \tag{4-27}$$

This function (shown in figure 4.8) is composed of a Gaussian distribution with exponential tails and has the following parameters:

$$\alpha_e \quad \text{is the fractional exponential component} \tag{4-28}$$

$$\sigma_p \quad \text{is the Gaussian width} \tag{4-29}$$

$$\mu_p \quad \text{is the Gaussian shift, and} \tag{4-30}$$

$$\tau_p \quad \text{is the exponential slope.} \tag{4-31}$$

The other terms are normalization factors such that the integral of the resolution function over all x is unity.

Monte-Carlo calculations were performed for electrons with various energies and

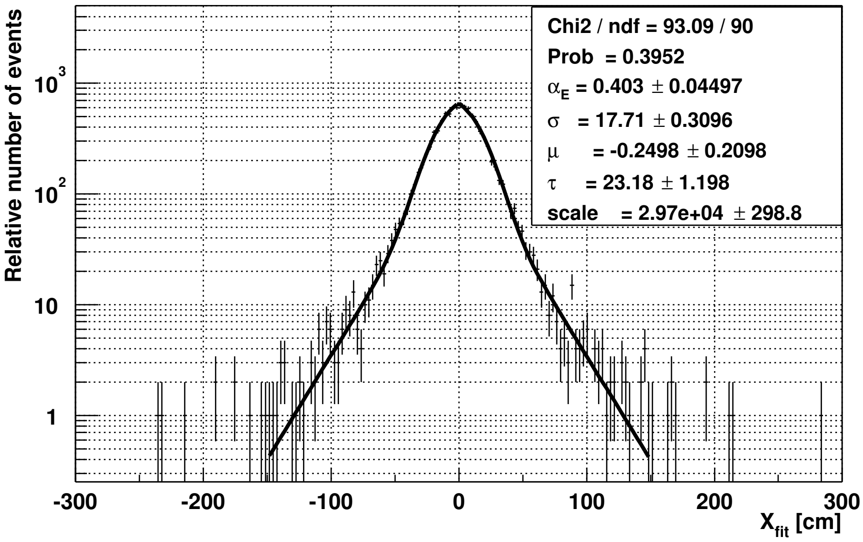

Figure 4.8: Position resolution from a Monte-Carlo calculation with 5 MeV electrons at the detector center.

the resolution parameters were extracted. Figure 4.9 shows the fit values of α_e as a function of electron energy. We see that this parameter does not depend on electron energy in our energy region of interest. We thus fix α_e in the position resolution function. Figure 4.10 shows the distributions of the other relevant parameters for the resolution function (σ_p, τ_p) as a function of electron energy. We note that above 6 MeV there is little dependence of the width of the resolution function on electron energy.

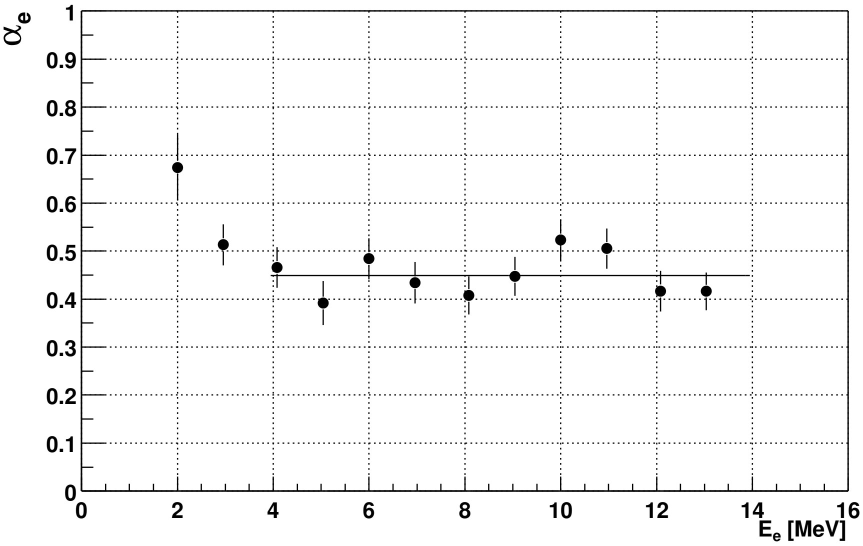

Figure 4.9: α_e fitter resolution parameter from 4 parameter fit to MC calculations for electrons. Since α_e is approximately constant, it is fixed to 0.45.

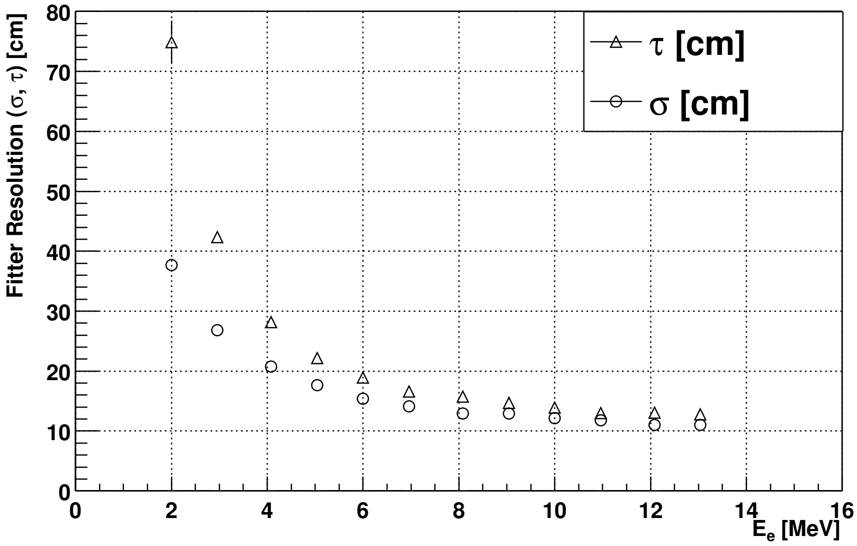

Figure 4.10: Fitter resolution parameters σ_p and τ_p for electrons derived from Monte-Carlo calculations.

4.3.2 Angular Resolution

To use the directional information from the Čerenkov events in SNO we must understand the angular resolution of the detector. For a given Čerenkov event, we define the error in the reconstructed event direction as

$$\theta_e = \vec{u_{fit}} \cdot \vec{u_e} \tag{4-32}$$

where

$$\vec{u_e} \quad \text{is the initial electron direction, and} \tag{4-33}$$

$$\vec{u_{fit}} \quad \text{is the fitted direction.} \tag{4-34}$$

To study the angular resolution of the SNO detector, we use the normalized resolution function described by Jillings [20]

$$P(\cos\theta) = \alpha_M \frac{\beta_M \exp[\beta_M(1-\cos\theta)]}{1-\exp(-2\beta_M)} + (1-\alpha_M)\frac{\beta_S \exp[\beta_S(1-\cos\theta)]}{1-\exp(-2\beta_S)} \tag{4-35}$$

This function has two components : a main peak due to the true angular resolution of the detector and a broad tail due to multiple scattering of electrons. The resolution function has three free parameters. These are the slopes of the two exponentials describing the main peak (β_S) and multiple scattering component (β_M), and the relative fraction of these (α_M). Shown in figure 4.11 is the distribution of θ_e for a Monte-Carlo calculation of 5 MeV electrons in SNO, along with the fit to the angular resolution function. Figure 4.12, also derived from Monte-Carlo calculations, shows the dependence of the angular resolution function on electron energy. We see that there is a weak dependence of the width of the resolution function (β_M, β_S) on energy, and a strong dependence of the multiple scattering component. The parameter α_M, the relative fraction of the multiple scattering component is seen to decrease with increasing energy as expected for multiple scattering.

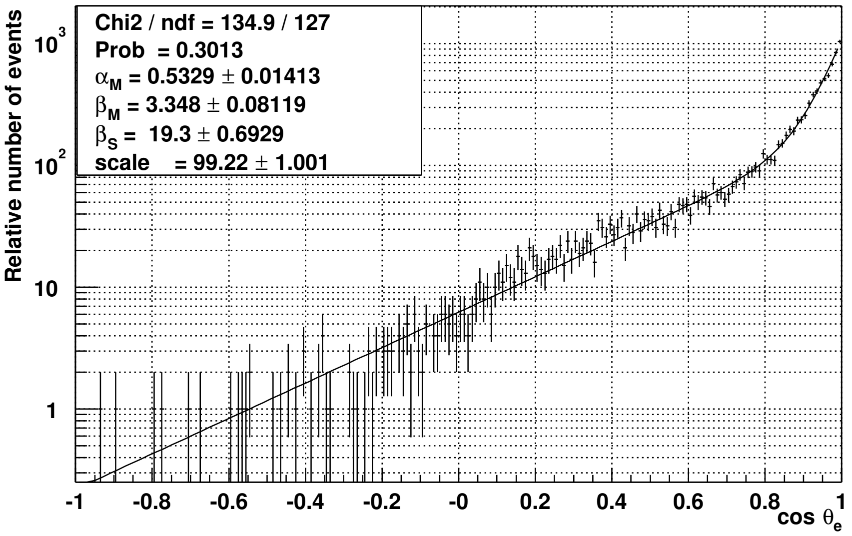

Figure 4.11: Distribution of θ_e defined by equation 4-32 from a Monte-Carlo calculation with 5 MeV electrons at the detector center. Also shown are the angular resolution parameters (α_M, β_M, and β_S) resulting from a fit to equation 4-35.

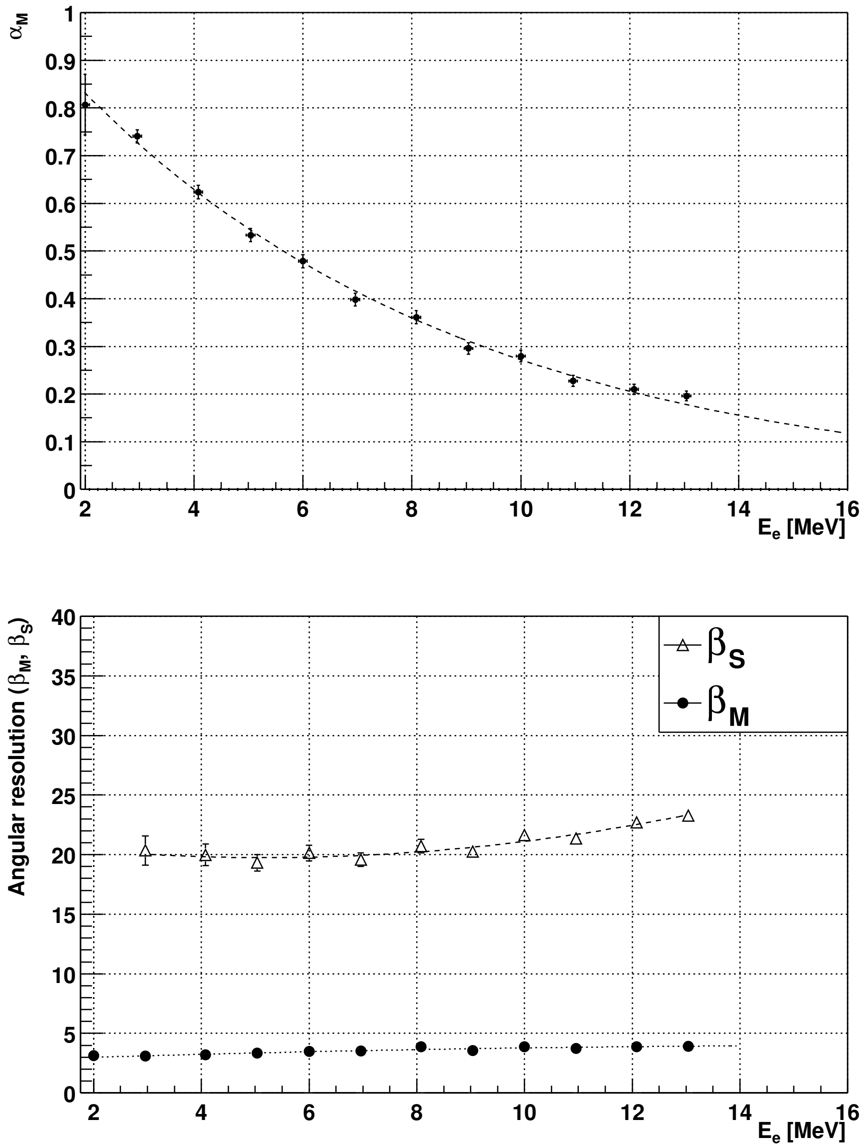

Figure 4.12: Angular resolution parameters derived from a Monte-Carlo calculation with mono-energetic electrons. We see a weak energy dependence of the angular resolution (β_M and β_S) on energy and a strong dependence of the multiple scattering component α_M.

4.4 Extracting Fitter Resolution from Calibration Data

In order to verify the Monte-Carlo calculations and assign systematic uncertainties in our neutrino analysis we must study fitter resolution with calibration sources in SNO. In this section we use ^{16}N events in the SNO detector to extract the vertex and angular resolution function parameters. The variation of resolution function parameters for various ^{16}N runs at different positions within the SNO detector is then used as an estimate of the systematic uncertainties in the derived resolution functions. These uncertainties can then be used as input to the solar neutrino analysis and used in generating the systematic uncertainties in derived neutrino fluxes.

4.4.1 Extracting Vertex Resolution

In this section we describe the extraction of the vertex resolution parameters from ^{16}N data. Since the ^{16}N source is a γ-ray source, the Čerenkov events are distributed around the source with a mean interaction length of about 34 cm. To study the vertex resolution function for electrons, we first generate the equivalent electron distribution with a Monte-Carlo calculation. The distribution of electron energies derived from an ^{16}N Monte-Carlo calculation is shown in figure 4.13. The distribution of vertices where these electrons are generated is shown in figure 4.14, projected onto the x-axis. We will treat the ^{16}N source as an electron source with a known spatial distribution. For a given electron spatial distribution S(x) and a vertex resolution function R(x), the apparent spatial distribution will be given by

$$N_r = \frac{dN}{dx_R} = \int_{-\infty}^{\infty} S(x)R(x_{fit} - x)dx \tag{4-36}$$

Equivalently, the spatial distribution projected onto a given axis will be given by

$$N_{fit} = \frac{dN}{dx_{fit}} = \text{Distribution of fit vertices projected onto } x_{fit} \text{ axis} \tag{4-37}$$

The S(x) distribution does not involve reconstruction resolution and is purely determined by the interaction of electrons and γ-rays in the detector. We are confident that the Monte-Carlo calculation (which uses EGS) correctly models these interactions [21]. For a given set of ^{16}N data, we directly calculate N_{fit} above, and use the S(x) distribution to extract the fitter resolution function by defining the χ^2 function

$$\chi^2 = \sum_{i=0}^{N_{bins}} \left(\frac{N_r - N_{fit}}{\sigma_i} \right)^2 \tag{4-38}$$

and finding the resolution parameters $\{\sigma_p, \tau_p\}$ which will minimize χ^2.

Shown in figure 4.15 are the extracted fitter resolution parameters for an ^{16}N calibration run at the detector center (top frame) and a Monte-Carlo calculation for the ^{16}N source using equation 4-38. We find very good agreement between the data and Monte-Carlo, as shown in table 4.1. Figure 4.16 shows the resolution widths extracted from a set of ^{16}N calibration runs at various radii within the detector. We find that fitter resolution is nearly constant throughout the sensitive detector volume.

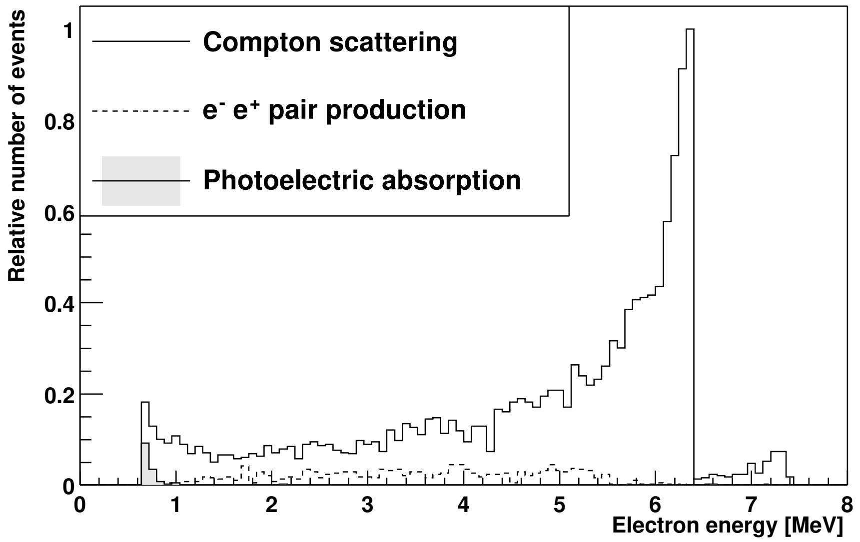

Figure 4.13: Electron energy spectra from the first interaction of γ-rays from ^{16}N decay with detector materials derived from a Monte-Carlo calculation. The contributions from Compton scattering, pair production, and photoelectric absorption are shown.

	α_e (fixed)	σ_p [cm]	τp [cm]
data	0.55	17.2 ± 0.5	32.3 ± 0.4
MC	0.55	15.5 ± 0.4	33.7 ± 0.3

Table 4.1: Comparison of vertex resolution parameters for ^{16}N calibration data and Monte-Carlo results. The parameter α_e was fixed to 0.55 for ^{16}N to reduce correlations between σ_p and τ_p; the vertex resolution function with this fixed parameter reproduces the data and Monte-Carlo distributions.

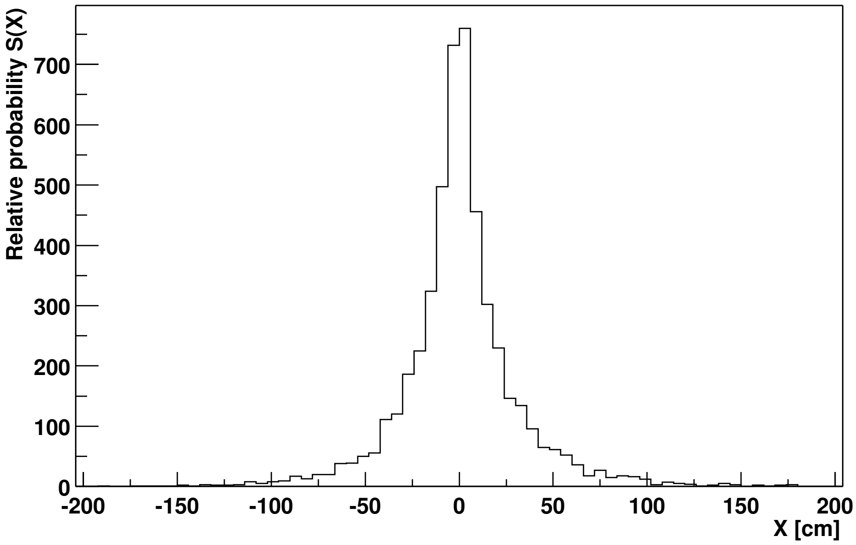

Figure 4.14: Distribution of first ^{16}N interaction point ($S(x)$ in equation 4-36) derived from a Monte-Carlo calculation.

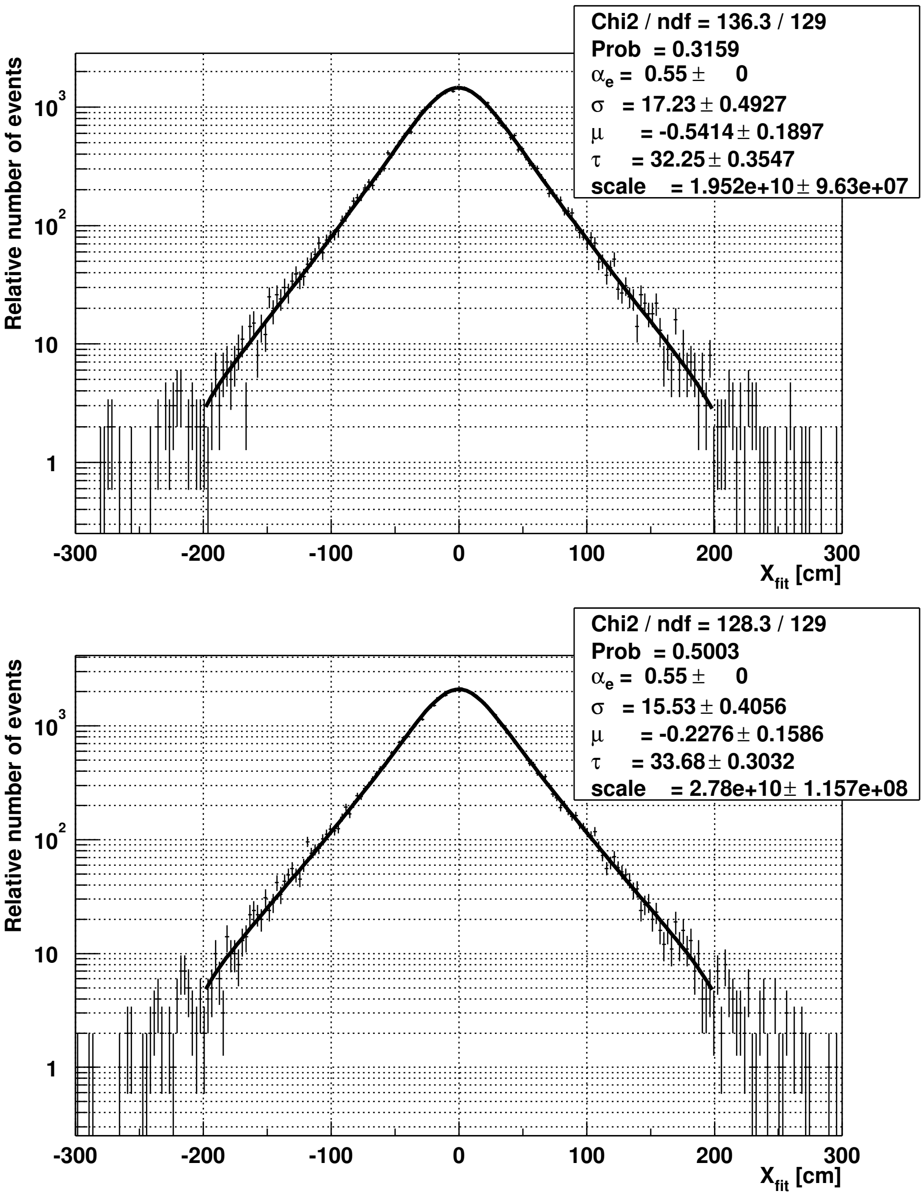

Figure 4.15: Vertex resolution from ^{16}N calibration data with the source at the detector center (top frame). Shown in the bottom frame is the result for a ^{16}N Monte-Carlo calculation.

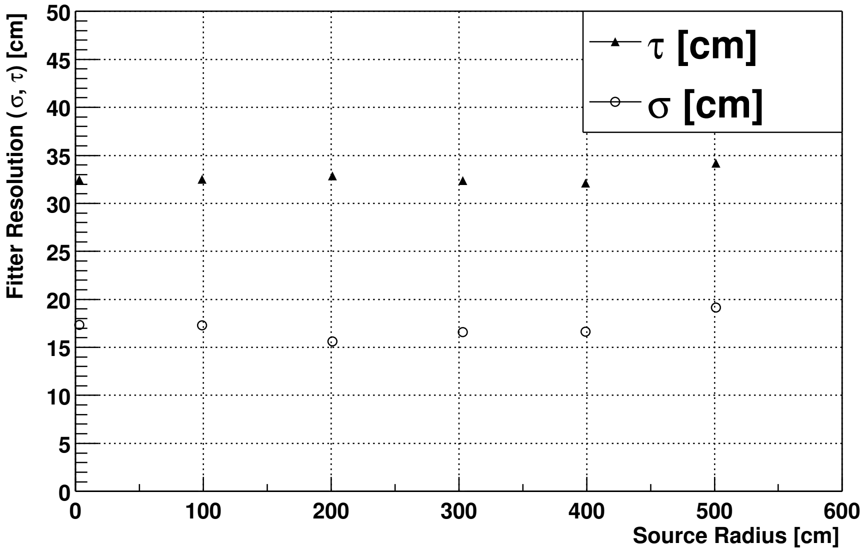

Figure 4.16: Fitter resolution parameters extracted from ^{16}N source data. The Gaussian (σ_p) and exponential (τ_p) components of the resolution function are not strongly dependent on source radius for positions inside our fiducial volume.

4.4.2 Reconstruction Efficiency

In the solar neutrino analysis we will convolve the recoil electron spatial distribution expected for a given neutrino source with the vertex resolution function of the detector. In this section we study the reconstruction efficiency which we define as the fraction of the signal which after reconstruction is well described by the resolution function. We define the reconstruction efficiency

$$\epsilon_F = \frac{\mathcal{N}_R}{\mathcal{N}_{fit} + \mathcal{N}_{failed}} \tag{4-39}$$

where

$$\begin{aligned} \mathcal{N}_{fit} &= \int_{-\infty}^{\infty} \frac{dN}{dx}_{fit} dx & (4\text{-}40) \\ \mathcal{N}_{failed} &= \text{Number of events for which no vertex was found} & (4\text{-}41) \\ \mathcal{N}_R &= \int_{-\infty}^{\infty} \frac{dN}{dx}_R dx, & (4\text{-}42) \end{aligned}$$

where $\frac{dN}{dx_R}$ is the spatial distribution predicted by the resolution function, from equation 4-36.

Shown in figure 4.17 is the reconstruction efficiency defined by equation 4-39 for the ^{16}N calibration source at various positions in the detector. We see that the reconstruction efficiency is independent of source radius for points inside our fiducial volume and is greater than 99.5%. We will thus ignore the effects of reconstruction inefficiencies in the solar neutrino analysis.

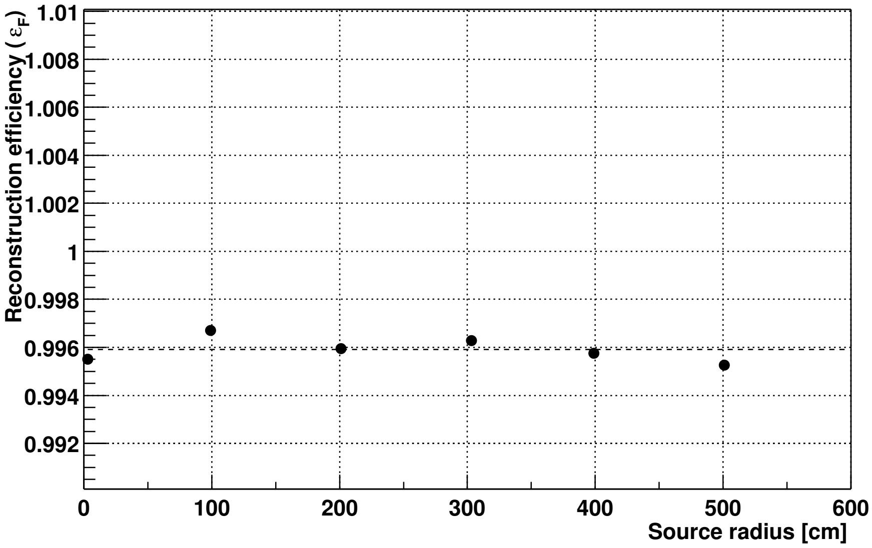

Figure 4.17: Fitter reconstruction efficiency measured with ^{16}N source data. The efficiency (calculated with equation 4-39) is independent of source radius for positions inside our fiducial volume.

4.4.3 Extracting Angular Resolution

In this section we describe the extraction of angular resolution parameters from ^{16}N data. Figure 4.18 demonstrates the method of determining the angular resolution of SNO with the ^{16}N source source described by Jillings [20]. ^{16}N events are selected which reconstruct greater than 120 cm from the source. We then use the vector from the source to the fitted vertex as an estimate of the original γ-ray direction. The θ_e distribution is then calculated for the selected events, and the angular resolution function parameters are derived from that distribution.

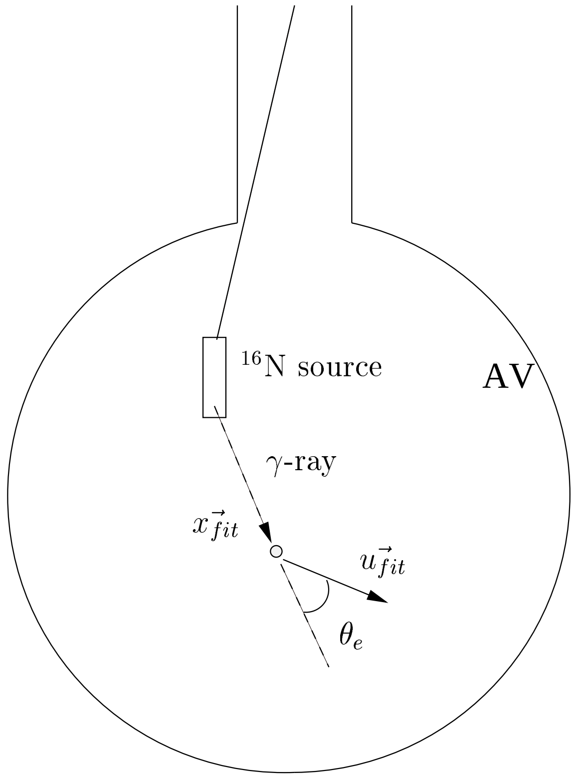

Figure 4.18: Angular resolution determined with the ^{16}N source.

Figure 4.19 shows the distribution of θ_e defined by equation 4-32 for ^{16}N calibration data and a Monte-Carlo calculation with the source at the detector center. We find very good agreement between the data and the Monte-Carlo calculation, as shown in table 4.2. Shown in figure 4.20 are the angular resolution parameters for a set of ^{16}N calibration data at different positions in the SNO detector. We find that the angular resolution is insensitive to the position for points inside the fiducial volume.

	α_M (fixed)	β_M	β_S
data	0.5	4.1 ± 0.1	18.8 ± 0.8
MC	0.5	3.9 ± 0.1	18.2 ± 0.6

Table 4.2: Comparison of angular resolution parameters for ^{16}N calibration data and Monte-Carlo results. The parameter α_M was fixed to 0.5 for ^{16}N to reduce correlations between β_M and β_S; the angular response function with this fixed parameter reproduces the data and Monte-Carlo distributions.

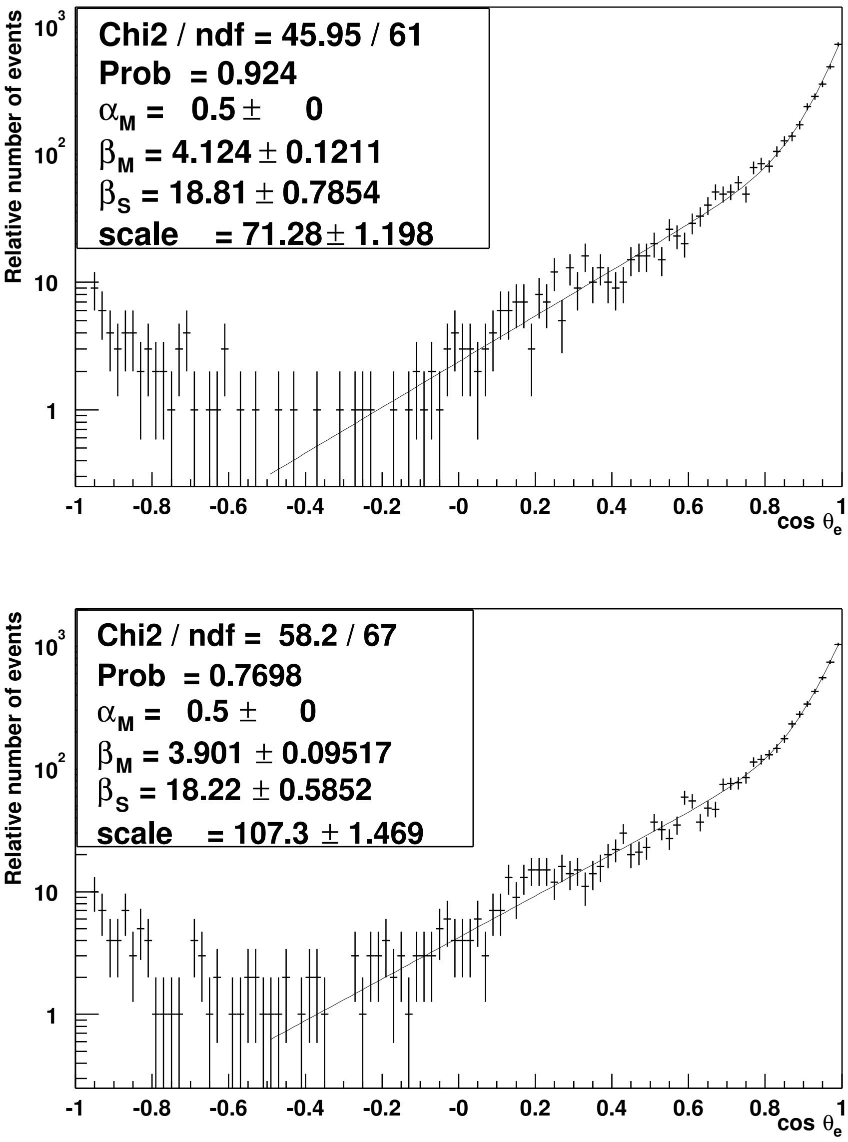

Figure 4.19: θ_e distributions and the fitted angular resolution functions from ^{16}N calibration data with the source at the detector center (top frame). Shown in the bottom frame is the result for a ^{16}N Monte-Carlo calculation. The peaks in the spectra near $\cos\theta_e = -1$ are due to mislocation of the ^{16}N events and do not affect the extracted angular resolution parameters.

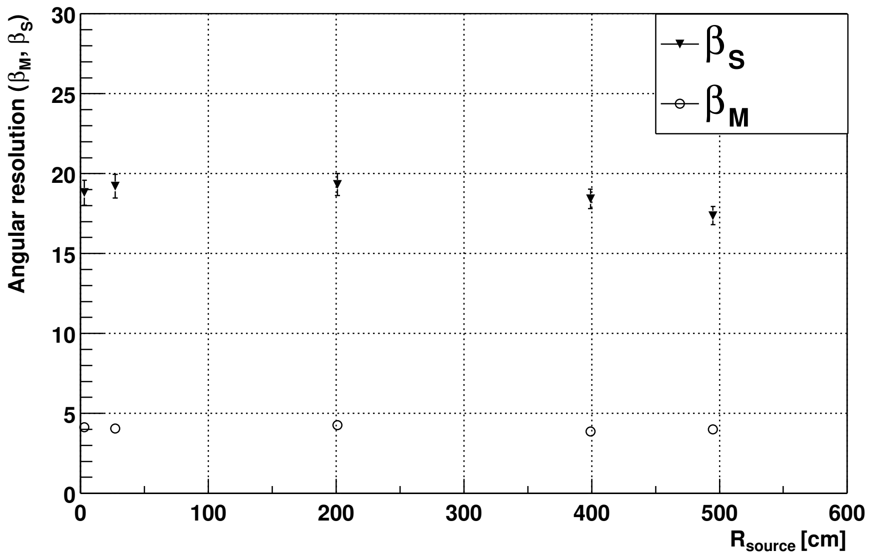

Figure 4.20: Angular resolution parameters extracted from ^{16}N source data.

4.4.4 Uncertainties in Vertex and Angular Resolution

Based on the results of sections 4.4.1 and 4.4.3, we will assign uncertainties in the vertex and angular resolution parameters by using the maximum of the deviations between the Monte-Carlo calculations and the source data at various positions in the detector. In the solar neutrino analysis we take the conservative approach of assigning standard 1σ uncertainties to the fit results based on these uncertainties in the resolution function parameters. We have found that vertex and angular resolution of Čerenkov events from the ^{16}N calibration source in SNO agree with the Monte-Carlo predictions. These derived uncertainties are shown in table 4.3. We will also neglect any inefficiencies in reconstructing Čerenkov events, since we have found that the distribution of fit vertices for the calibration data are described well by the fitter resolution functions.

σ_p	τ_p	β_M	β_S
0.12	0.07	0.06	0.12

Table 4.3: Fractional uncertainties in the fitter vertex and angular resolution parameters.

4.5 Effect of Systematic Uncertainties in Vertex and Angular Resolution

To estimate what effect the uncertainties in table 4.3 will have on the solar neutrino analysis, we will generate the radial and angular profiles by allowing the parameters to vary by one standard error (1σ).

We define the radial profile for a source distribution $S(r)$ by

$$\frac{dN}{dR_{fit}} = \int_{r=0}^{\infty} S(r)R(r, R_{fit})dr \tag{4-43}$$

where we have integrated over the vertex response function $R(r, R_{fit})$, and R_{fit} is the reconstructed event radius. For a uniform source we have that $S(r) = r^2$, so we write

$$\begin{aligned} S(r) &= r^2 \text{ for } r <= 600 \text{ cm} && \text{(4-44)} \\ &= 0 \text{ for } r > 600 \text{ cm} && \text{(4-45)} \end{aligned}$$

for charged current events, and

$$\begin{aligned} S(r) &= r^2 \text{ for } r <= 841 \text{ cm} && \text{(4-46)} \\ &= 0 \text{ for } r > 841 \text{ cm} && \text{(4-47)} \end{aligned}$$

for elastic scattering events.

For neutral current events we define $S(r)$ by calculating the radial distribution of the first electron after neutron capture on deuterium with Monte-Carlo. Figure 4.21 shows the result for a calculation with neutrons distributed uniformly throughout the D_2O.

The radial profiles for CC and NC events in the D_2O calculated with equation 4-43 are shown in figures 4.22 and 4.24, along with the profiles for the measured $\pm 1\sigma$ uncertainties in vertex resolution. We find that there is little variation in the radial profiles for the measured vertex resolution uncertainty. Figure 4.23 shows the calculated radial distribution for a uniform neutron source along with the distribution derived from a Monte-Carlo calculation, where we see there is good agreement. Since the ES events are produced uniformly in both the heavy and light water regions of the detector, the radial profile for these is uniform in volume throughout the D_2O and is unaffected by uncertainties in the vertex resolution function.

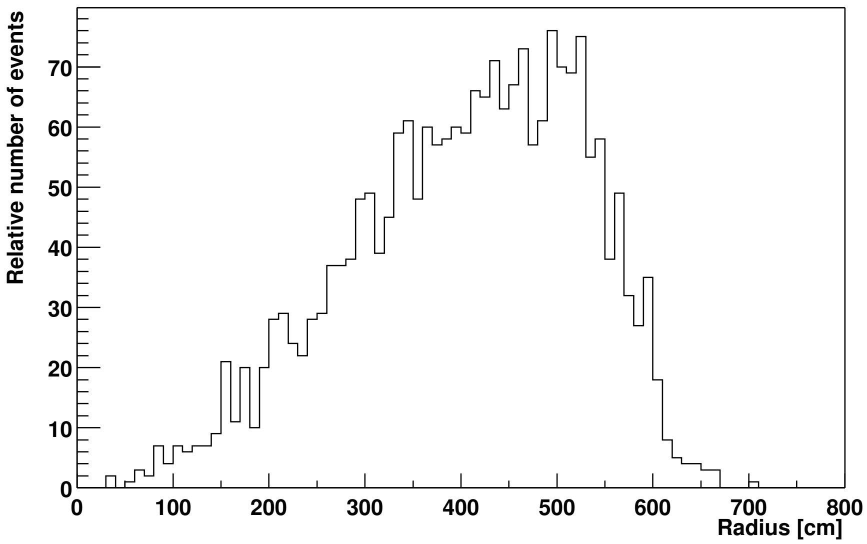

Figure 4.21: Radial distribution of electrons following neutron captures on deuterium derived from a Monte-Carlo calculation.

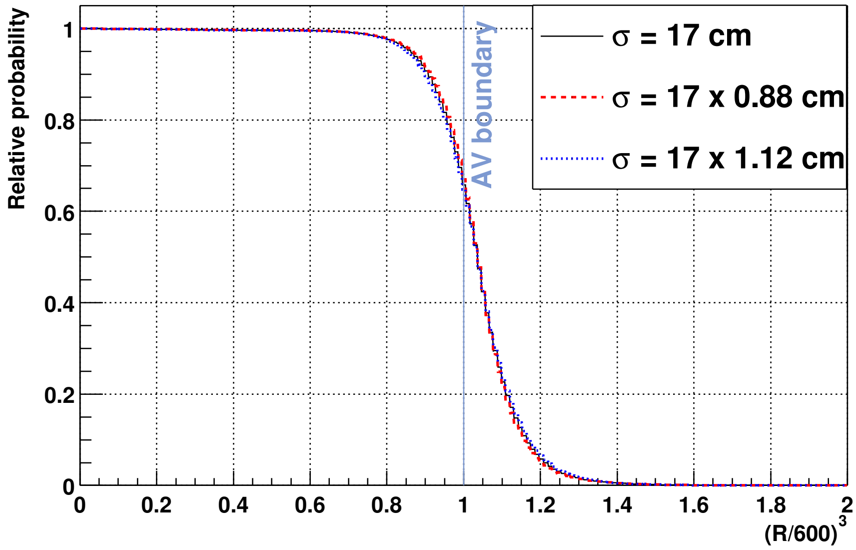

Figure 4.22: Reconstructed radial distribution predicted by equation 4-43 for a uniform source in the D_2O for the measured fitter resolution and $\pm 1\sigma$ uncertainties. The uncertainty in the radial profile is seen to be small.

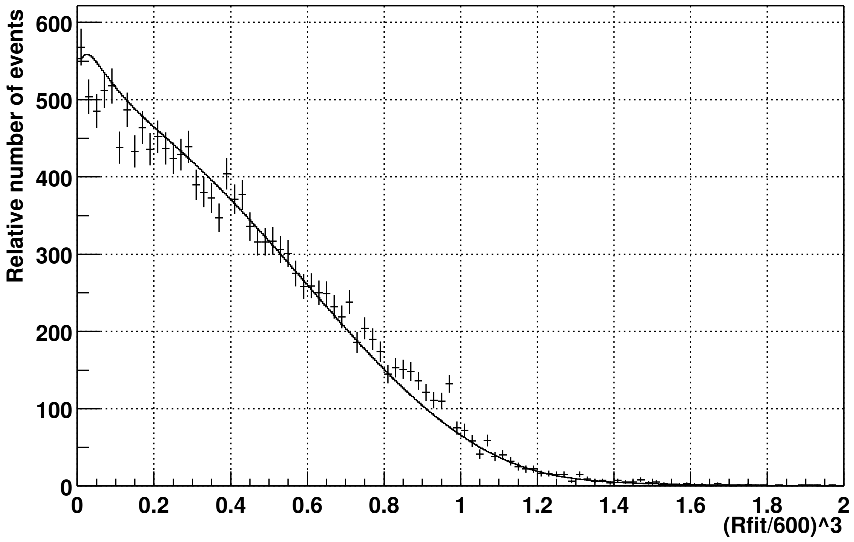

Figure 4.23: Reconstructed radial distribution predicted by equation 4-43 for a uniform source of neutrons in the D_2O. Although the neutrons are distributed uniformly throughout the D_2O, the neutron captures on ^2H and resulting γ-rays are not, as shown in figure 4.21, leading to a distribution different than shown in figure 4.22. Shown is the Monte-Carlo result (histogram) and the analytic result of equation 4-43 with $\sigma_p = 17$ cm.

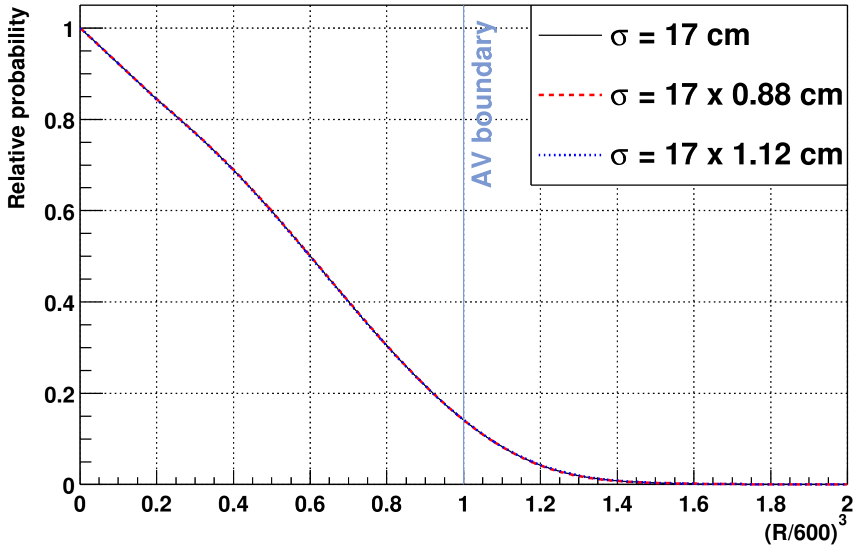

Figure 4.24: Reconstructed radial distribution predicted by equation 4-43 for a uniform source of neutrons in the D_2O. Shown are the results for the nominal resolution of 17 cm, and the +/- 1σ limits.

Chapter 5

Neutron Transport in SNO

To extract the solar neutrino neutral current signal, we must understand in detail thermal neutron transport and neutron capture in the detector. The use of the distinctive neutral current signal radial profile in SNO has been studied by Simpson and Wang [22, 23] and shown to be useful in extracting the neutral current signal from SNO in the pure D_2O phase. The study by Simpson and Wang [22] provided the author of this work the original motivition for extracting the NC signal from the pure D_2O phase of SNO. In this section we present results of two Monte-Carlo calculations, using MCNP [24], and GEANT-4 [25], as well as a comparison between neutron calibration data from a ^{252}Cf source and Monte-Carlo. The cross section data used for both calculations were taken from the ENDF/B-VI [26] library.

Figure 5.1 shows the relevant cross sections for neutron capture in the SNO detector. Table 5.1 shows the average cross sections at thermal energies with weighting by isotopic abundance for materials in our fiducial volume. We would thus expect about half of the neutrons in an infinite volume of D_2O to capture on ^{2}H. The capture of neutrons on ^{2}H generated uniformly in the D_2O volume will be somewhat lower than this value since there is a large cross-section for capture on ^{1}H, either in the heavy water itself, or the acrylic vessel and light water which act as a neutron sink. This capture on ^{2}H is an important one since it is followed by the release of a 6.25 MeV γ-ray which serves as a detectable signal for neutrons in pure D_2O. Captures on other detector materials do not result in detectable Čerenkov signals above an analysis threshold of 6 MeV.

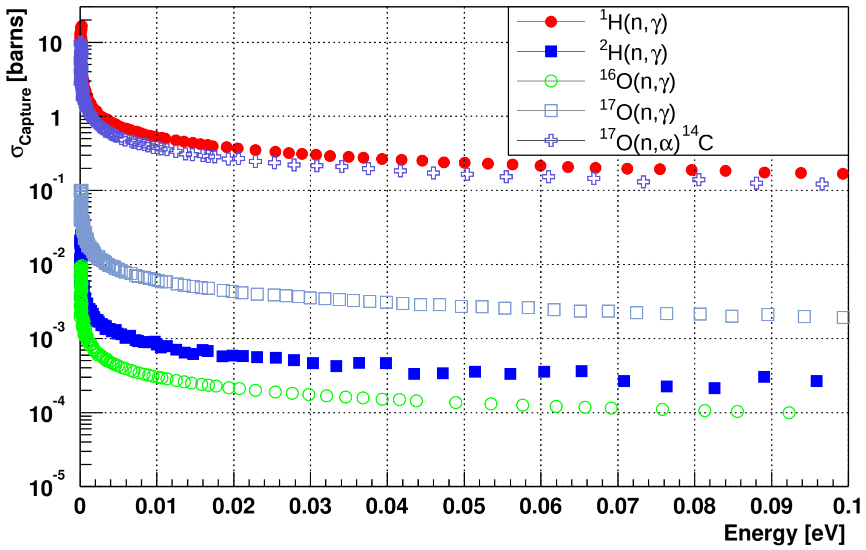

Figure 5.1: Tabulated neutron cross sections from [26] for materials in our fiducial volume.

Isotope	Reaction	Thermal cross section [mb]	Isotopic Abundance	Relative Probability
^{1}H	(n,γ)	333	0.0008888	0.303
^{2}H	(n,γ)	0.52	0.9991112	0.532
^{16}O	(n,γ)	0.19	0.99945	0.0972
^{17}O	(n,γ)	3.83	0.00076	0.0011
^{17}O	(n,α)	235	0.00076	0.0662

Table 5.1: Thermal neutron cross sections and isotopic abundances for materials in our fiducial volume.

5.1 ^{252}Cf Neutron Calibration Source

To study the response of the SNO detector to neutrons and validate the Monte-Carlo calculations, SNO makes use of a ^{252}Cf source. The activity is encapsulated in an acrylic puck with a diameter and thickness of approximately 2.5 cm. This puck is then attached to a combination of acrylic and stainless steel hardware for deployment into the detector, as shown in figure 5.2.

^{252}Cf decays by both α-particle emission and spontaneous fission. Several neutrons are released per spontaneous fission. Table 5.2 shows the neutron multiplicities and branching ratios for ^{252}Cf [27, 28]. Table 5.3 shows the measured activity and inferred neutron flux for the ^{252}Cf source used in SNO [29].

The energy spectrum of neutrons emitted in the spontaneous fission of ^{252}Cf is well described by a Maxwellian distribution with T = 1.42 MeV [30]. This energy spectrum is shown in figure 5.3 and was used in the GEANT Monte-Carlo calculations, although the deduced neutron capture efficiency and radial profiles depend very little on this spectrum since the neutrons are thermalized after traveling only a few centimeters in the heavy water.

$t_{\frac{1}{2}}$ (years)	α-decay branching ratio	Spontaneous fission branching ratio	Neutron multiplicity $\bar{\nu}$
2.645	0.96908	0.03092	3.7676 ± 0.0047

Table 5.2: Relevant properties of ^{252}Cf.

α-decay rate [sec^{-1}]	Spontaneous fission rate [sec^{-1}]	Neutron flux [n's sec^{-1}]
176 ± 17.6	5.15 ± 0.52	19.4 ± 1.9

Table 5.3: Activity of the ^{252}Cf calibration source used in SNO, measured on September 1, 2000 [29].

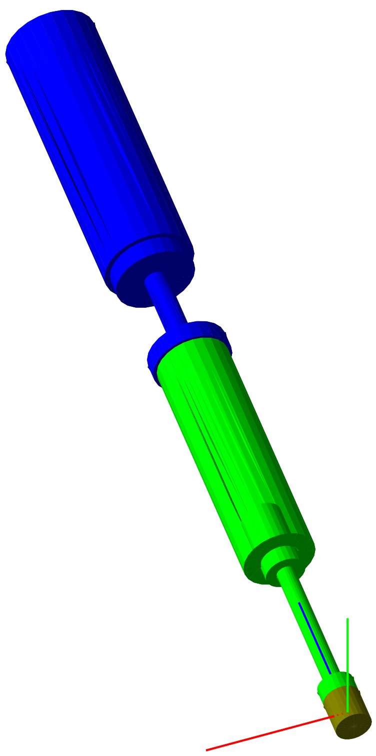

Figure 5.2: Source geometry used in the Monte-Carlo calculations. Shown are the stainless steel attachment hardware (blue), acrylic attachment hardware (green), and acrylic source puck (grey). The axes drawn are 10 cm in length.

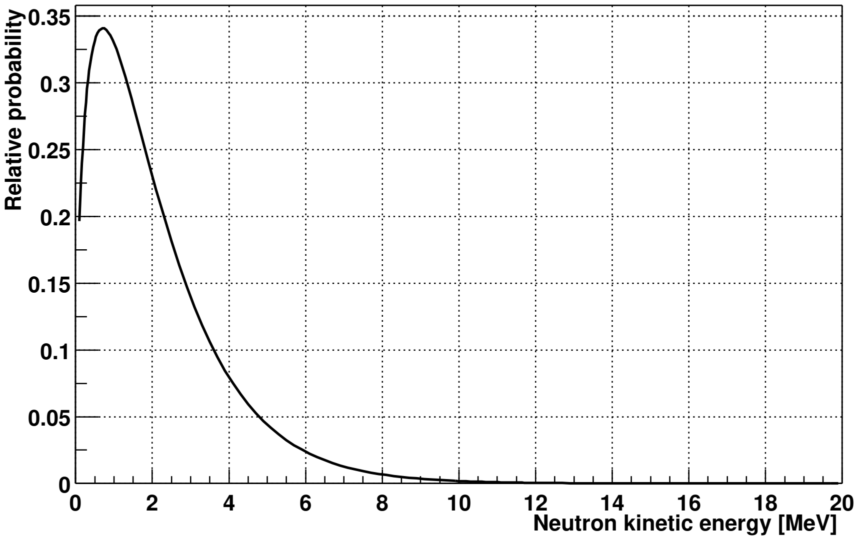

Figure 5.3: Neutron kinetic energy spectrum from spontaneous fission of ^{252}Cf. This distribution was used as input to the GEANT Monte-Carlo calculations.

5.2 Source Monte-Carlo

In this section results of Monte-Carlo calculations of neutron transport in SNO are presented. To verify the SNOMAN Monte-Carlo, which uses MCNP for neutron calculations, a separate GEANT-4 Monte-Carlo calculation was performed. We have found that both Monte-Carlo calculations agree to a few percent.

To study the effects of the source mounting hardware we have performed a Monte-Carlo calculation which included the full source geometry shown in figure 5.2. Table 5.4 shows the relative capture probabilities for the source at r = 300 cm, where we find that the acrylic puck and source mounting hardware are responsible for only about 0.3% of the neutron captures. We thus ignore the effects of the source hardware in the remainder of the analysis. The radial profiles for captures on various isotopes derived from this Monte-Carlo calculation are shown in figure 5.4.

$(n,\gamma)^1$H in D_2O	$(n,\gamma)^1$H in AV	$(n,\gamma)^1$H in source	$(n,\gamma)^2$H	$(n,\gamma)^{16}$O	$(n,\gamma)^{17}$O	$(n,\alpha)^{17}$O
0.262	0.171	0.00334	0.427	0.0770	0.0011	0.0611

Table 5.4: Relative capture efficiencies on various materials for a source Monte-Carlo with the source at a radius of 300 cm. The acrylic in the source and mounting hardware is responsible for only about 0.3% of the neutron captures.

Table 5.5 shows the relative capture efficiencies on the various isotopes in the detector for a source of neutrons at r = 0 cm. The Monte-Carlo calculations predict that approximately half of the neutrons released at the detector center will capture on deuterium for the isotopic abundances in the heavy water shown in table 5.1. Shown in table 5.6 are the capture efficiencies for a uniform source of neutrons in the D_2O. We find that approximately 30% of neutrons released uniformly in the heavy water

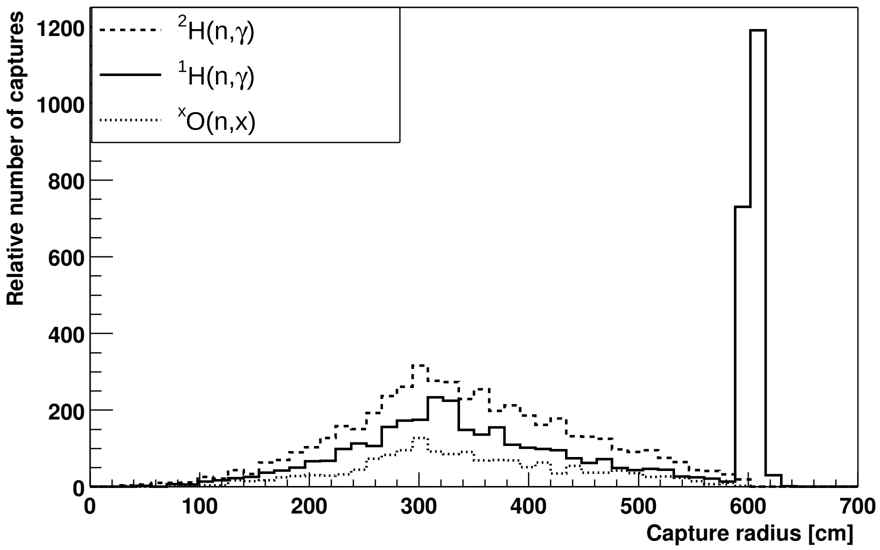

Figure 5.4: Distribution of capture radii on various materials for a source Monte-Carlo with the source at a radius of 300 cm.

region will capture on deuterium. The reconstructed radial profile for this uniform source is shown in figure 5.5.

Code	$(n,\gamma)^1$H in D_2O	$(n,\gamma)^1$H in acrylic	$(n,\gamma)^2$H	$(n,\gamma)^{16}$O	$(n,\gamma)^{17}$O	$(n,\alpha)^{17}$O
G4	0.277	0.0794	0.485	0.0865	0.0011	0.0707
SNOMAN	0.293	0.0570	0.496	0.0897	0	0.0642

Table 5.5: Relative capture efficiencies on our detector materials as predicted by the two Monte-Carlo calculations for neutrons at r = 0. The agreement between the two codes is within a few percent.

Code	$(n,\gamma)^1$H in D_2O	$(n,\gamma)^1$H in acrylic	$(n,\gamma)^2$H	$(n,\gamma)^{16}$O	$(n,\gamma)^{17}$O	$(n,\alpha)^{17}$O
G4	0.167	0.452	0.288	0.0521	0.0008	0.0376
SNOMAN	0.186	0.422	0.298	0.0562	0	0.0376

Table 5.6: Relative capture efficiencies on our detector materials as predicted by the two Monte-Carlo calculations for neutrons uniform in the D_2O. The two codes agree to a few percent.

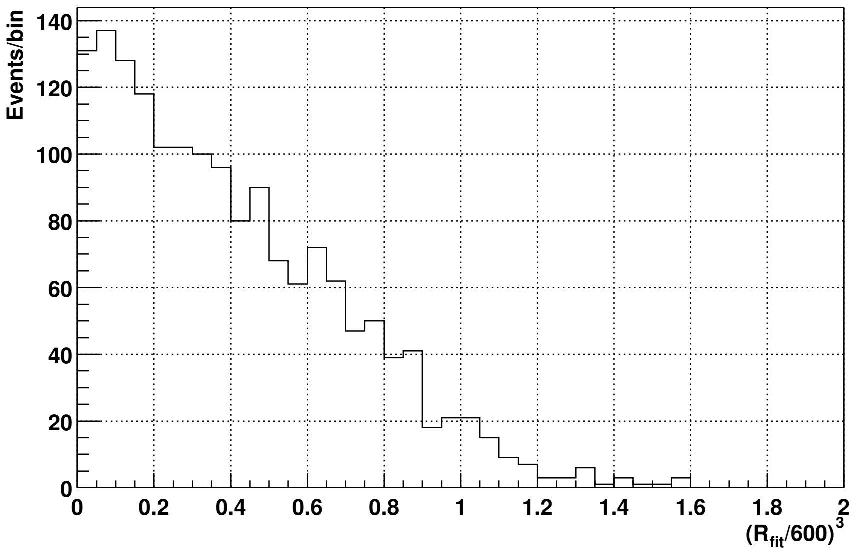

Figure 5.5: Reconstructed radial profile for a uniform neutron source.

5.3 ^{252}Cf Source Data

In this section data taken with the ^{252}Cf calibration source are analyzed and compared to the Monte-Carlo calculations. Since ^{252}Cf has many secondary β's and γ-rays associated with its decay we will restrict the analysis to regions which are spatially separated from the source so that the predominant signal is due to 6.25 MeV γ-rays from neutron capture on deuterium. Shown in figure 5.6 is the projection of reconstructed vertices onto the Z-X plane for a ^{252}Cf calibration source run with the source at the detector center and for events with E $>$ 3.5 MeV (top frame) and E $>$ 5.6 MeV (bottom frame). We can clearly see the intense activity near the source, much of which is β and γ activity.

To attempt to remove this contamination, several fiducial volume cuts were applied, with progressively larger regions around the source removed. Shown in figure 5.7 are the energy spectra from the calibration source, with volumes removed in 50 cm radial increments. We see an excess of low energy events near the source and note that for distances greater than about a meter from the source the energy spectrum is constant and is consistent with that expected for 6.25 MeV γ-rays. Shown in figure 5.8 are the radial profiles for reconstructed events with and without an energy threshold imposed. The distribution for all events is seen to peak near the source and outside r=600 cm, which is consistent with low energy activity from the source and some background leakage from the light water radioactivity. With an imposed energy threshold of 5.6 MeV we see that the radial profile agrees well for distances greater than about a meter from the source. Based on these comparisons we infer that for distances greater than 150 cm from the source and with an imposed threshold of 5.6 MeV we have a signal due to 6.25 MeV γ-rays from neutron capture on deuterium.

For the purpose of comparing the ^{252}Cf source calibration data to Monte-Carlo calculations, we will thus define the neutron capture efficiency

$$\begin{aligned} \epsilon' &= \text{fraction of captures on D with} \\ & \quad 150 \text{ cm } < |R_{fit} - R_{source}| < 540 \text{ cm, and} \\ & \quad \text{E} > 5.6 \text{ MeV} \end{aligned} \tag{5-1}$$

Figure 5.9 shows this efficiency as a function of source radius in the detector for both calibration data and Monte-Carlo. Figure 5.10 shows the deviation between the data and Monte-Carlo, where we see that there is good agreement.

We will thus use the capture efficiency for a uniform source of neutrons

$$\epsilon_D = 0.3 \pm 0.03 \tag{5-2}$$

with the capture profile given by the Monte-Carlo calculation.

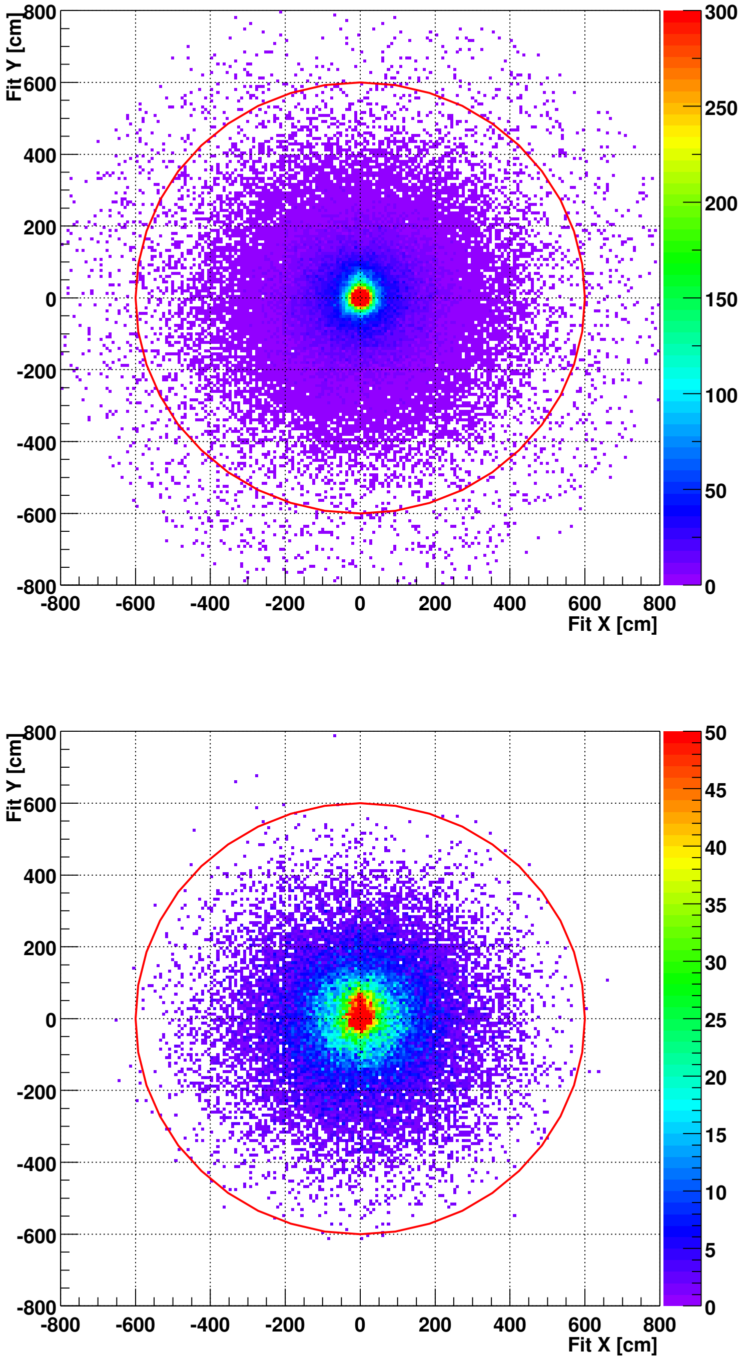

Figure 5.6: Projection of reconstructed vertices for the ^{252}Cf source at the detector center. Intense activity near the source is seen for an energy threshold of 3.5 MeV (top frame) and 5.6 MeV (bottom frame), attributed to β's and γ-rays associated with the fission of ^{252}Cf.

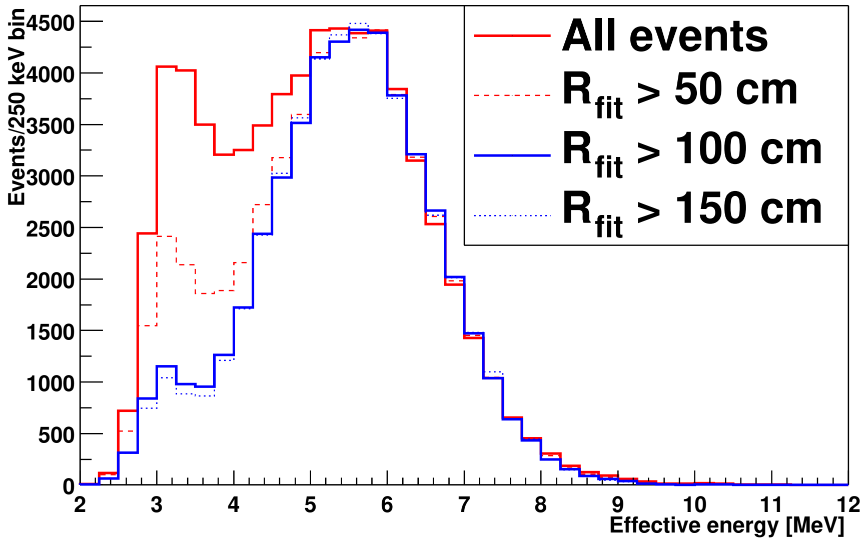

Figure 5.7: Energy spectra of reconstructed events for the ^{252}Cf source at the detector center. We see an excess of events near the source which are not apparent for distances from the source greater than about a meter.

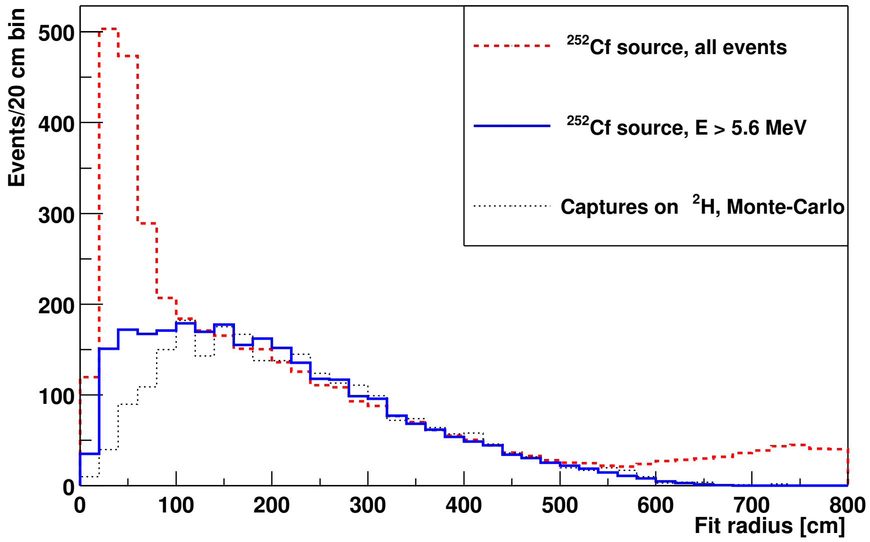

Figure 5.8: Radial profile of reconstructed events for the ^{252}Cf source at the detector center. We see an excess of events at lower energies which are attributed to β's and γ-rays associated with the decay of ^{252}Cf. The radial profile is seen to agree with the Monte-Carlo for distances from the source greater than about a meter.

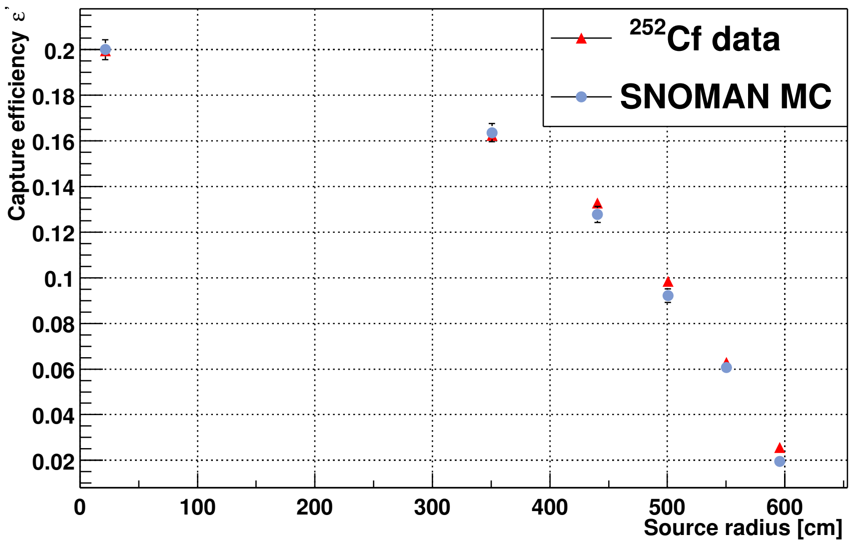

Figure 5.9: Neutron capture efficiency defined by equation 5-1 versus source radius for the ^{252}Cf source (triangles) and Monte-Carlo calculations (circles).

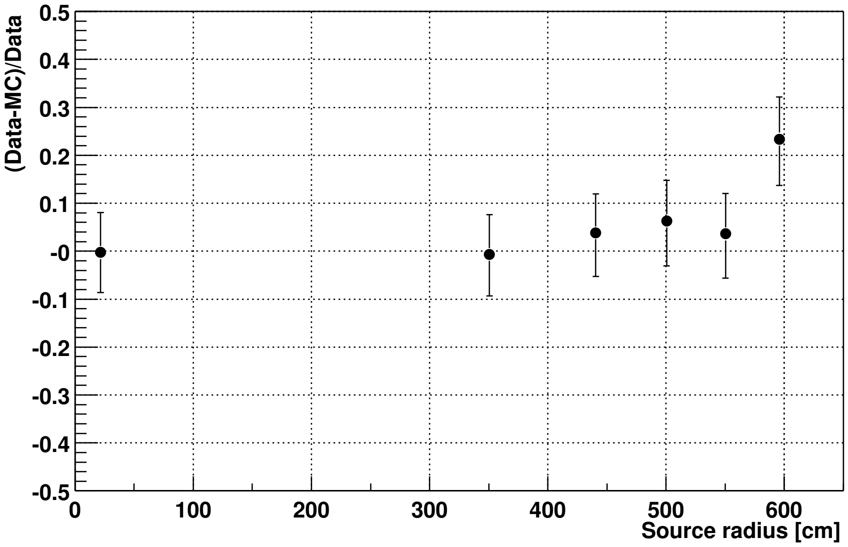

Figure 5.10: Deviation in neutron capture efficiency (ϵ') versus source radius between the ^{252}Cf source data and Monte-Carlo. We find good agreement. Shown are the combined statistical and systematic uncertainties due to vertex reconstruction, energy calibration and source intensity normalization.

Chapter 6

Energy Calibration

The energy of Čerenkov events in SNO is determined primarily by the number of phototubes which have fired (NHITs). This number depends on the number of photons produced and the response of the detector to these photons. A precise measurement of the solar neutrino signals measured in SNO requires that the energy calibration of Čerenkov events is well understood. Since SNO has a limited number of calibration sources with which to study energy calibration and data from these sources is only taken at certain positions in the detector, the approach taken is to accurately measure all optical properties of the detector and then rely on detailed Monte-Carlo calculations to convert between the SNO measurables (the number of hit phototubes and reconstructed event vertices) and the equivalent electron energy which would produce those measurables. The optical properties which dominantly affect the number of hit phototubes for a given energy event are the variation of phototube efficiency with photon incident angle and photon attenuation in the inner detector materials (D_2O, acrylic, and H_2O). These parameters are measured at various time intervals with extensive optical calibrations at various photon wavelengths. The results of this section are based on a preliminary set of optical calibrations.

The absolute photon collection efficiency is determined by comparing the number of phototubes hit in a Monte-Carlo calculation with the measured optical parameters to data from an ^{16}N calibration source. Extensive scans with the ^{16}N source are then taken at many points throughout the sensitive detector volume. The deviations between the measured detector gain and the Monte-Carlo prediction are then used as an estimate of the systematic uncertainty in the absolute energy calibration. We have found agreement between ^{16}N source data and Monte-Carlo throughout our sensitive volume.

In this section we discuss comparisons of ^{16}N calibration data and Monte-Carlo. We also describe the energy calibration function used to convert between SNO measurables and equivalent electron energy. The uncertainties in the energy scale and resolution will then be used to estimate uncertainties in the derived solar neutrino fluxes.

6.1 ^{16}N Decay

The primary energy calibration source for SNO are the γ-rays from the decay of ^{16}N. Shown in table 6.1 are the γ-ray energies emitted in ^{16}N decay [27] along with their branching ratios. The spectrum is relatively simple with most of the γ-rays at 6.13 MeV. Events are selected based on the presence of the β particle, so that we can select decays which occur in the relatively small volume of the source decay chamber.

E_g (keV)	I_g (%)	decay mode
787.26	3E-6	β^-
867.712	0.0002102	β^-
986.9315	0.00348	β^-
1067.510	3E-5	β^-
1754.96	0.12110	β^-
1954.78	0.0386	β^-
2741.55	0.826	β^-
2822.212	0.134	β^-
6048.210		β^-
6128.634	67.06	β^-
6915.56	0.0386	β^-
7115.15	4.94	β^-
8869.35	0.07610	β^-

Table 6.1: γ-rays from ^{16}N decay.

6.2 Time Spectra

Understanding the detector response to scattered photons is quite difficult since the exact path taken by such photons in not known, thus they have traveled through unknown amounts of the various detector media. To reduce the systematic uncertainties involved with scattered and reflected photons, the approach taken here is to use only direct photons for energy calibration. To select photons which have traveled directly from the event vertex to a phototube, we reconstruct the event position as described in chapter 4 and use the time residual defined by equation 4-2. We then select only phototube hits for which this time residual is small compared to the time residual for a photon which has scattered and traveled a greater distance than that of the straight line path.

Time residual histograms for ^{16}N source runs at radii of 0 to 5 meters and source

Monte-Carlos are shown in figures 6.1 and 6.2. We can clearly see the effects of scattering as the source is moved out in radius. The PSUP reflection peaks which are more than 50 ns away from the prompt peak with the source at the center can be seen to move closer to this peak as the source is moved towards the PSUP.

Based on these time residual histograms, a window of ± 10 ns was chosen. This window will greatly reduce the amount of scattered photons used for energy calibration, while it is significantly wider than the 1.5 ns tube resolution so that we are relatively insensitive to moving direct photons out of the window. For energies in the region of interest for solar neutrinos, there is typically only a single photon which hits a phototube.

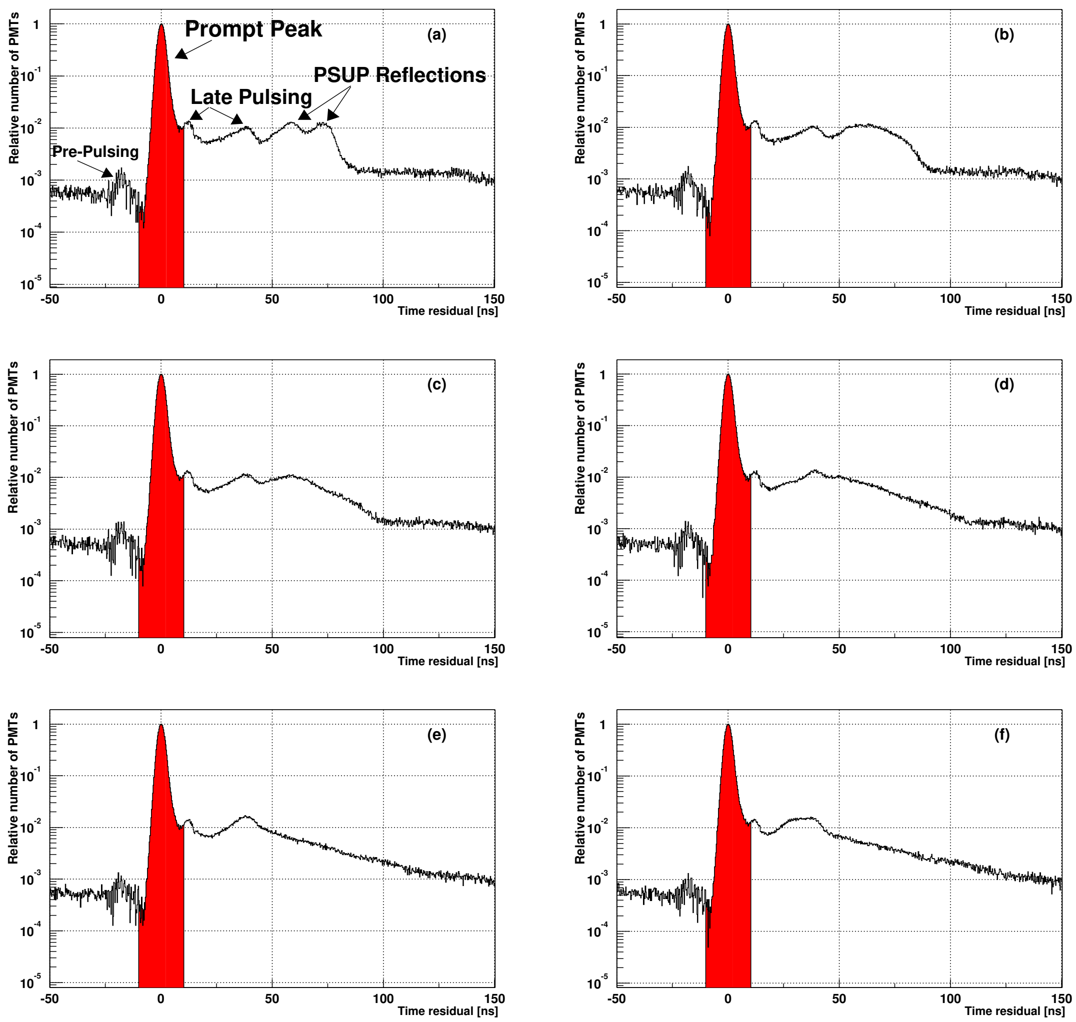

Figure 6.1: Time residual histograms from ^{16}N calibration data at various radii. (a) center (b) 100 cm (c) 200 cm (d) 300 cm (e) 400 cm (f) 500 cm. The pre-pulsing and late pulsing peaks are properties of the phototubes and do not depend on the source position, while the PSUP reflection peaks vary with source position. The shape and fraction of light in the main peak used for energy calibration (shaded) is insensitive to source position.

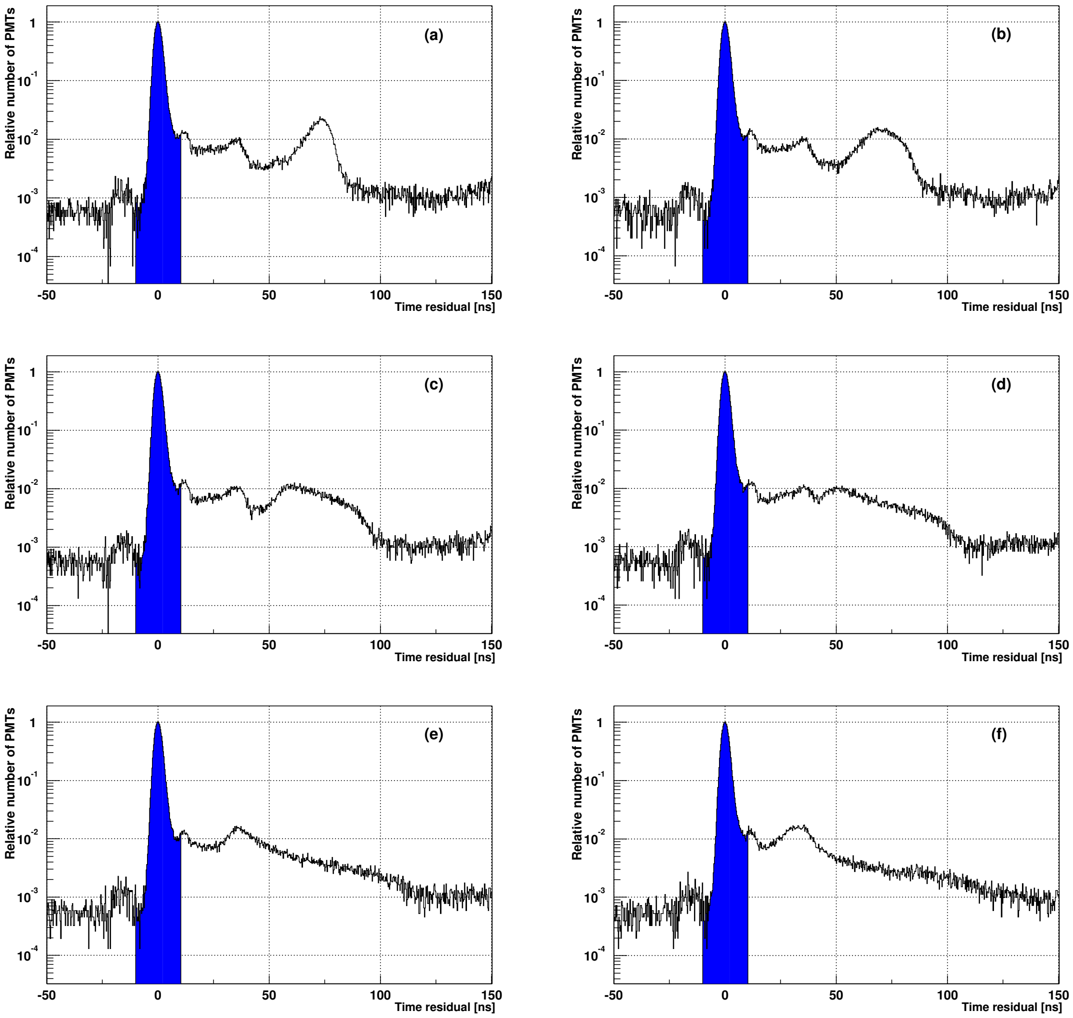

Figure 6.2: Time residual histograms for Monte-Carlo calculations of the ^{16}N source at various radii. (a) center (b) 100 cm (c) 200 cm (d) 300 cm (e) 400 cm (f) 500 cm. The shape of the main peak (shaded) is independant of source position while the scattered light is not.

6.3 Energy Calibration Function

Once we have measured the optical properties of the detector materials and absolute photon collection efficiency, detailed Monte-Carlo calculations are used to map between the measurables for an event (number of hit PMTs, $r_{fit}, \cos\theta_r$) and the electron energy which would lead to those measurables. To simplify the energy calibration procedure an analytic function is used to correct for the variation in detector optical response with event radius and direction. We thus correct the number of in-time hits for a given event to the equivalent number had the event been at the center of the detector and then map this number to electron energy. In addition to correcting for the optical response of the detector we also apply corrections for the relative number of on-line tubes available to collect photons for a given event and for the small drifts in absolute detector gain. The energy calibration techniques described here were implemented in the SNO collaboration's data analysis and Monte-Carlo package (SNOMAN) by the author.

For the energy calibration, we define an effective number of PMTs hit as

$$N_{eff} = N_{win} - N_{dark} \tag{6-1}$$

with

$$N_{win} = \text{number of in-time hits } (\pm 10 \text{ ns}), \text{ and} \tag{6-2}$$

$$N_{dark} = \text{number of in-time noise hits.} \tag{6-3}$$

The average PMT noise rate is determined by acquiring data with a pulsed trigger. The average number of noise hits in the 440 ns event window was found to be

$$N_{PGT} \approx \ 2.1 \text{ hits}, \tag{6-4}$$

which is equivalent to a dark noise rate for each photomultiplier tube of

$$R_{dark} \approx \ 593 \text{ Hz}. \tag{6-5}$$

Since this dark noise is uniform throughout the 440 ns window, the number of in-time noise hits is given by

$$\begin{aligned} N_{dark} &\approx N_{PGT} \times \frac{20 \text{ ns}}{440 \text{ ns}} \\ &\approx 0.1 \text{ hits per event}. \end{aligned} \tag{6-6}$$

This number of noise hits is equivalent to only about 10 keV so that we are insensitive to small uncertainties in the dark PMT noise.

We then apply the optical and gain corrections to determine the equivalent N_{eff} at the detector center

$$N_{cor} = N_{eff} \times \frac{1}{\epsilon_{response}} \times \frac{1}{\epsilon_{hardware}} \times \frac{1}{\epsilon_{drift}} \tag{6-7}$$

with

$$\begin{aligned} \epsilon_{response} &= \text{detector optical response at } \vec{r}, \vec{u} \\ &= \textstyle\sum_{\theta'} \sum_{\phi'} \sum_{\lambda} \frac{\epsilon_{PMT}(\lambda)}{\lambda^2} g(\theta', \phi') \\ &\times e^{-\mu_1 d_1} e^{-\mu_2 d_2} e^{-\mu_3 d_3} P(r, \theta, \theta', \phi') M(r, \theta', \phi') \end{aligned} \tag{6-8}$$

$$\epsilon_{hardware} = \frac{\text{no. tubes on}}{\text{no. tubes used in Monte-Carlo}} \tag{6-9}$$

$$\epsilon_{drift} = \text{correction for small drifts in detector gain with time} \tag{6-10}$$

and

ϵ_{PMT}	is the PMT wavelength response,
$g(\theta', \phi')$	is the Čerenkov light distribution,
$\mu_i d_i$	is the attenuation for medium i,
i	$=1, 2, 3$ corresponding to D_2O, acrylic, and H_2O,
$P(r, \theta, \theta', \phi')$	is the PMT angular response, and
$M(r, \theta, \theta', \phi')$	is a multiple hit correction.

To study calibration data and Monte-Carlo calculations, we also define a corrected N_{eff} with no optical or drift corrections,

$$N'_{eff} = N_{eff} \times \frac{1}{\epsilon_{hardware.}} \tag{6-11}$$

$\epsilon_{response}$ is the optical correction factor which accounts for attenuation of photons in the detector media, the photo-multiplier tube response and multiple hits in a single PMT. This correction is applied to estimate the equivalent number of hit phototubes were the event at the detector center. The SNO detector has very little variation in response throughout the central D_2O region. The largest deviation in $\epsilon_{response}$ as a function of source radius in this region is about 7% as can be seen from figure 6.3. Evaluation of the integral in equation 6-9 is detailed in a study by Ford [31].

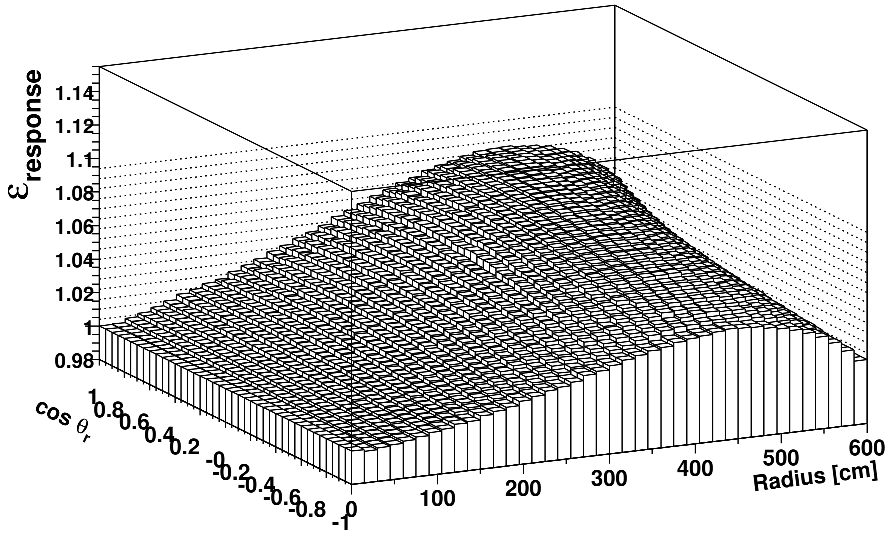

Figure 6.3: Optical response as defined by equation 6-9 for 8 MeV electrons. The variation in response throughout our fiducial volume is small.

$\epsilon_{hardware}$ is applied to correct for the number of phototubes available to a given event. The largest deviations in the number of live channels is also small and is on the order of 200 out of 9453 phototubes or about 2%.

ϵ_{drift} is used to correct for any small changes in the absolute photon collection efficiency of the detector over time. To measure this drift, a set of ^{16}N calibration data is collected at regular intervals. The centroid of the N'_{eff} distribution for the source at the detector center is used as the measure of detector gain. Figure 6.4 shows the results of these runs for a time period covering our neutrino data set. The data are scaled such that the first point used for calibrating the Monte-Carlo is unity. There is a small drop in detector gain of about 0.4% per month. The dashed line is used as a correction function to the absolute energy scale for a given date.

To map the corrected number of hit phototubes (N_{cor}) to electron energy, a set of

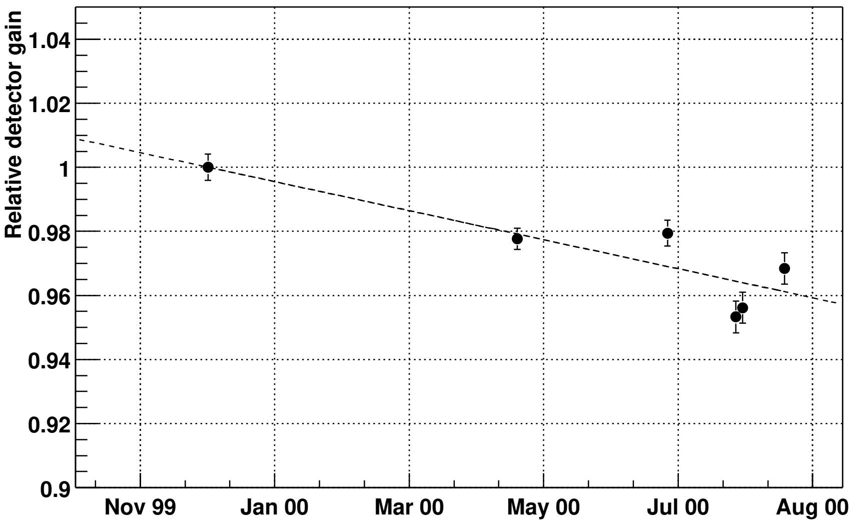

Figure 6.4: Photon collection efficiency versus time. Shown is the relative peak of the N'_{eff} distribution from ^{16}N calibration runs at the detector center. The dashed line is used as ϵ_{drift}, the correction to the absolute energy scale.

Monte-Carlo calculations are performed for mono-energetic electrons at the detector center. We fit a Gaussian function to the resultant N_{eff} spectrum and generate the map

$$E_e = E_{MC}\left(N_{eff}\right) \tag{6-12}$$

with

$$E_{MC}(N_{eff}) \quad = \quad N_{eff} \rightarrow E_e \text{ map} \tag{6-13}$$

The map is generated for event energies in our region of interest for solar neutrino analysis, from about 2 to 30 MeV. Shown in figure 6.5 is the result of these Monte-Carlo calculations. The detector energy resolution is also determined from the set of Monte-Carlo calculations. Shown in figure 6.6 is the width of the resolution function versus electron energy.

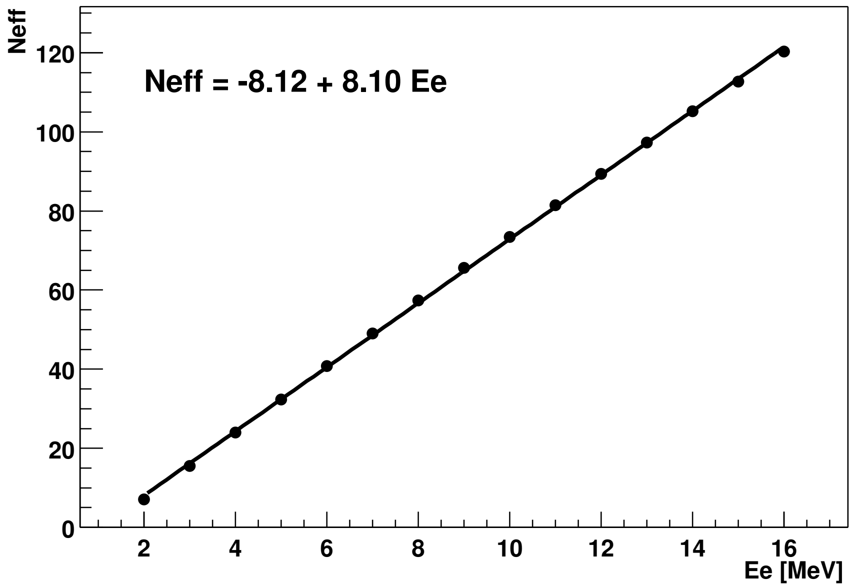

Figure 6.5: N_{eff} versus total electron energy (E_e) derived from Monte-Carlo calculations for mono-energetic electrons at the detector center.

We can now generate Monte-Carlo events, calculate N_{cor} from equation 6-7 and use the map of figure 6.5 to produce a calibrated energy spectrum. We can equivalently convolve a given electron energy distribution with the response function of figure 6.6 to calculate the predicted energy spectrum measured with SNO for this input distribution. Figure 6.7 shows the N_{eff} distribution for a Monte-Carlo calculation with 8 MeV electrons.

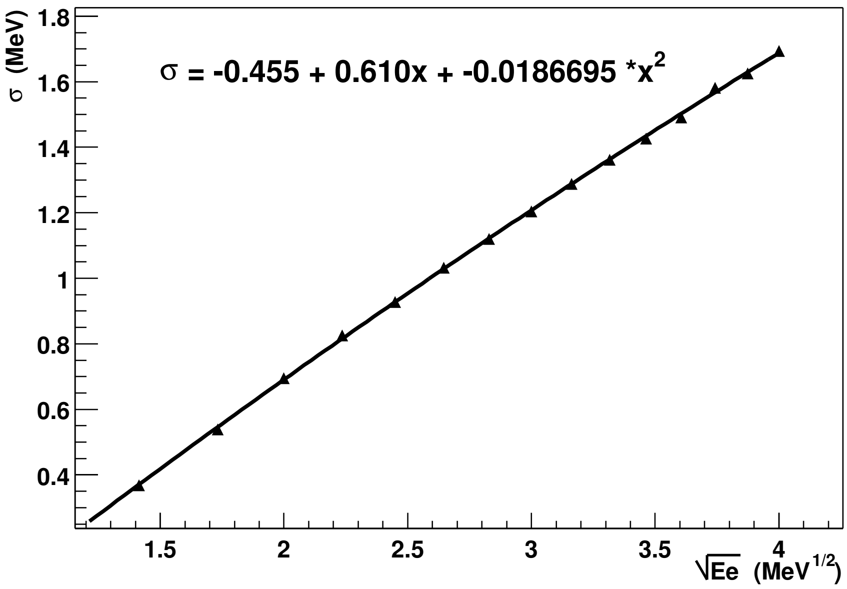

Figure 6.6: Energy resolution derived from Monte-Carlo calculations.

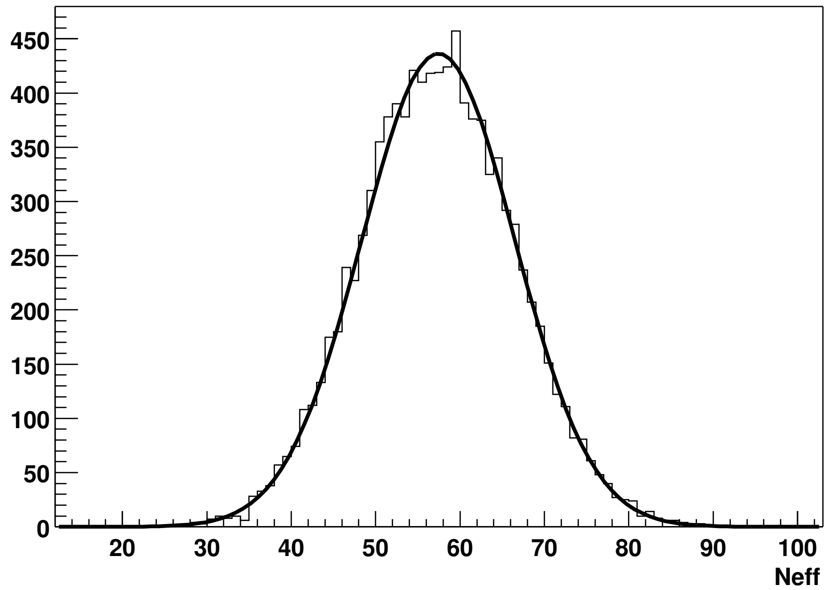

Figure 6.7: N_{eff} distribution for a Monte-Carlo calculation of 8 MeV electrons.

6.4 Comparison between ^{16}N Monte-Carlo and Data

To verify the Monte-Carlo and estimate the systematic uncertainties in energy calibration, a set of ^{16}N calibration data was taken throughout the sensitive detector volume. Figure 6.8 shows the N'_{eff} distributions for ^{16}N data taken at the detector center and a similar Monte-Carlo calculation. We see that there is excellent agreement between the data and Monte-Carlo.

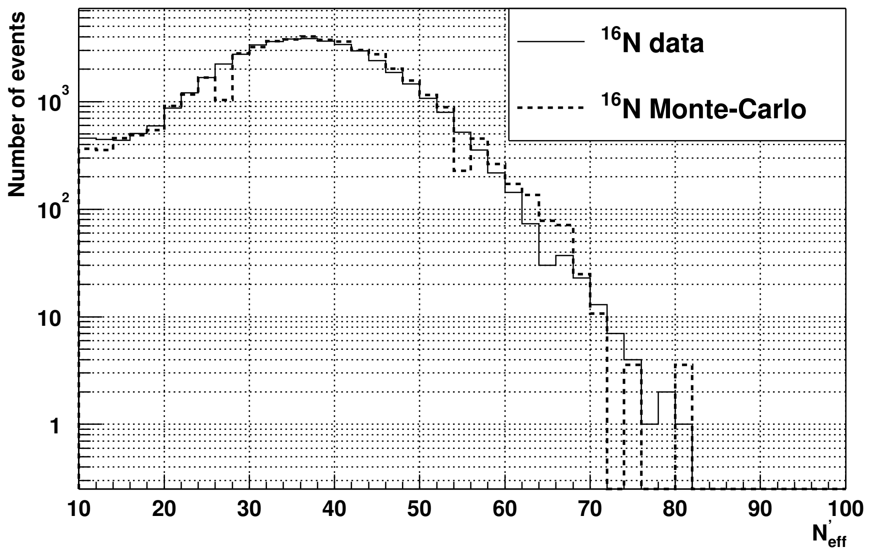

Figure 6.8: ^{16}N N'_{eff} spectra for calibration data and a Monte-Carlo calculation.

Figure 6.9 shows the N'_{eff} distributions for the ^{16}N calibration source at the detector center and at a radius of 465 cm. We see the shift in detector gain consistent with the optical response shown in figure 6.3. After applying the energy calibration function, this shift is removed, as shown in figure 6.10. Shown in figure 6.11 are the relative centroids of the N'_{eff} and calibrated energy distributions plotted versus source radius for a set of ^{16}N calibration data. We see that the maximum shift in gain is about 7% and that most of this variation is correctly removed by the energy calibration function. Figure 6.12 shows the distribution of deviation in the energy scale from figure 6.11, weighted by volume. A Gaussian fit to this distribution shows a 1σ deviation of about 0.7%.

The widths of the calibrated energy spectra were also determined by fitting a Gaussian function to the distributions. Shown in figure 6.13 are these fit widths versus source radial position. We see that the energy spectra become slightly narrower as the source radius is increased, due to the increased photon collection efficiency. For the solar neutrino analysis we have used the energy resolution determined by Monte-Carlo calculation for events at the detector center. This approximation is valid since the deviation in energy resolution with radius is small. As shown in figure 6.14, the maximum deviation is about 4%. The volume weighted deviation is shown in figure 6.15 and has a mean of approximately 3%, with a 1σ width of 2%. We will assume an uncertainty of approximately 5% in energy resolution. It is shown in a following section that this uncertainty does not contribute significantly to uncertainties in the solar neutrino analysis.

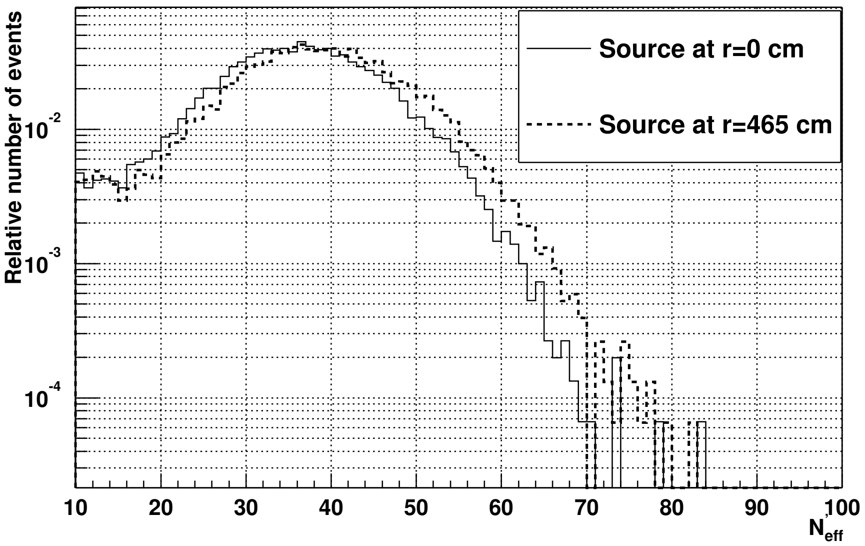

Figure 6.9: N'_{eff} distributions for the ^{16}N source at r=0 and r=465 cm. The shift in detector gain is apparent.

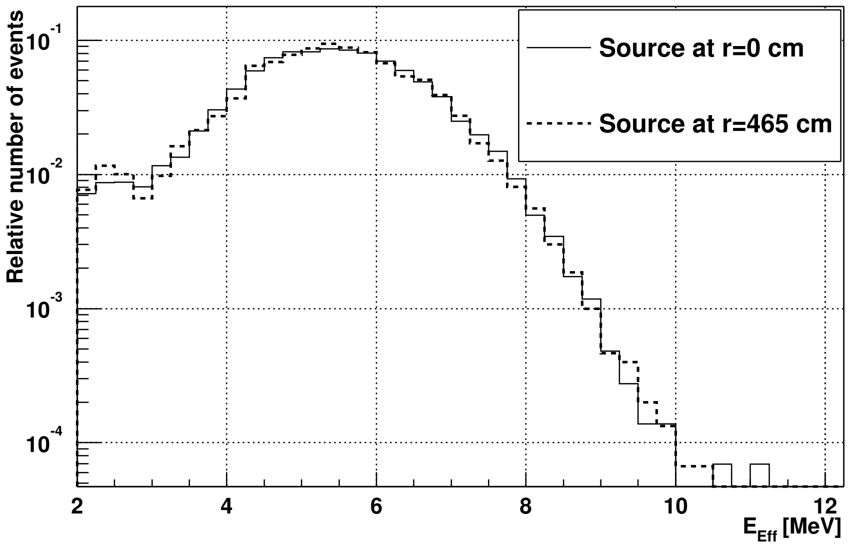

Figure 6.10: Energy spectra for the ^{16}N source at r=0 and r=465 cm. The shift in detector gain has been compensated for by the energy calibration function.

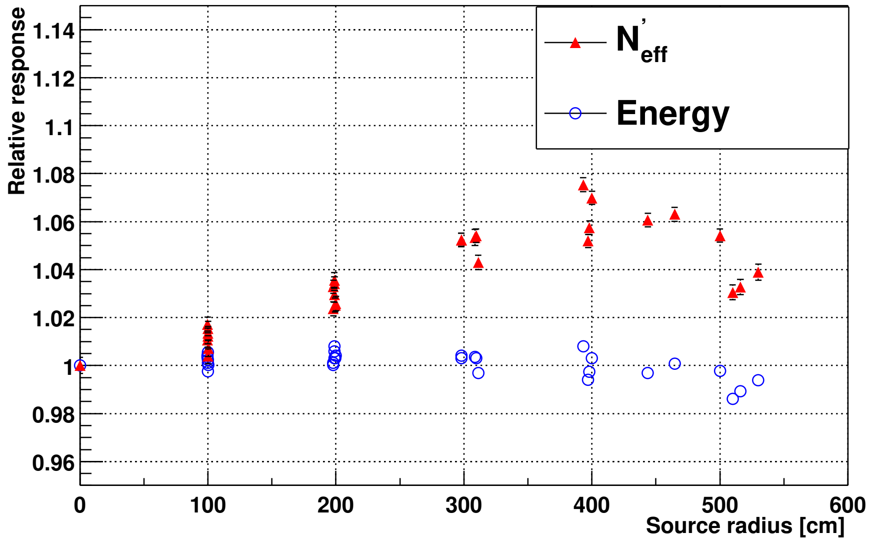

Figure 6.11: Comparison of N'_{eff} and calibrated energy as a function of source radius for ^{16}N data. We see the absolute detector gain varies by about 7% and this variation is removed by the energy calibration.

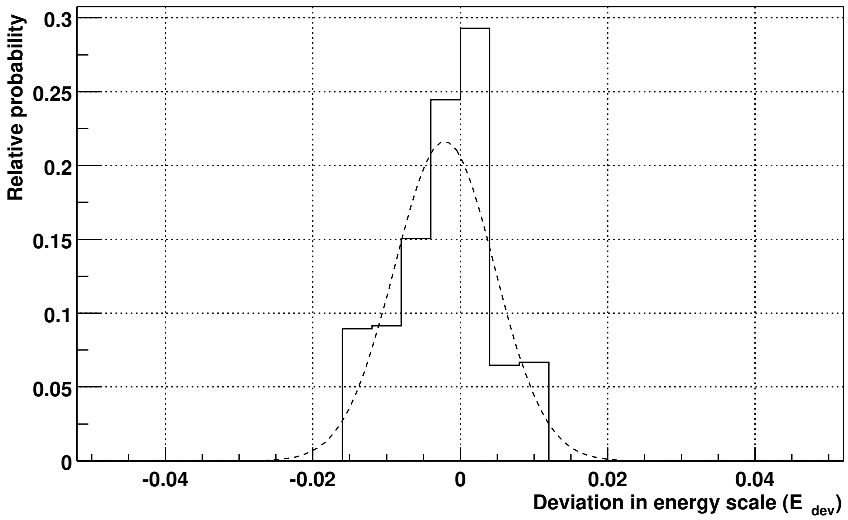

Figure 6.12: Deviation in energy scale from ^{16}N calibration runs. The histogram is the distribution of relative differences in the centroid of the calibrated energy spectra for a set of ^{16}N calibration data in the detector with weighting by volume. The Gaussian fit has a 1σ width of about 0.7%.

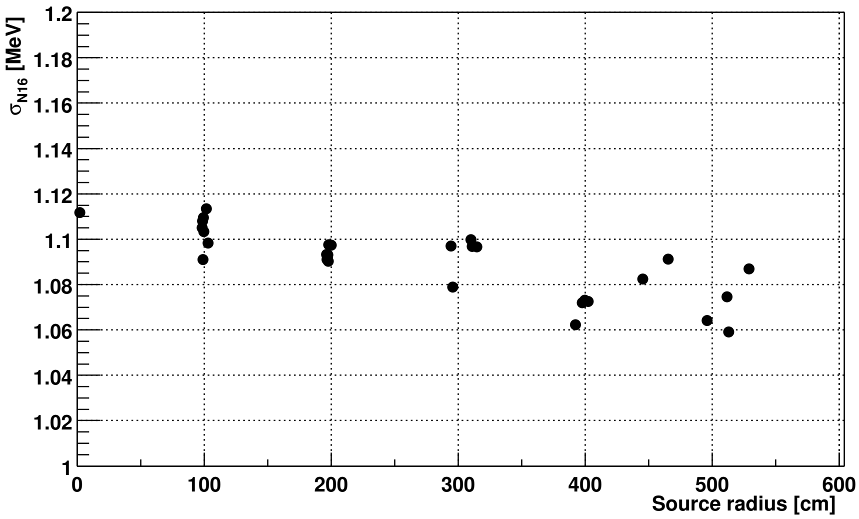

Figure 6.13: Energy resolution versus source radius for ^{16}N calibration runs.

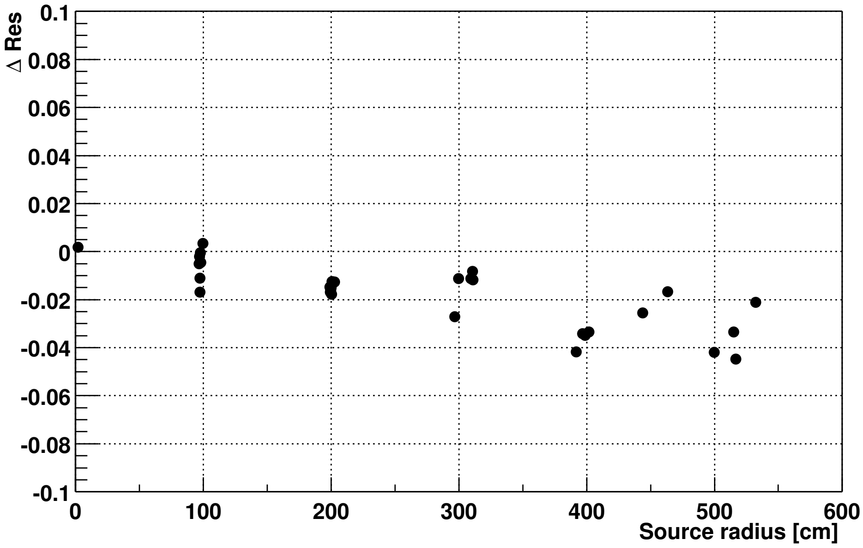

Figure 6.14: Deviation in energy resolution versus source radius for ^{16}N calibration runs.

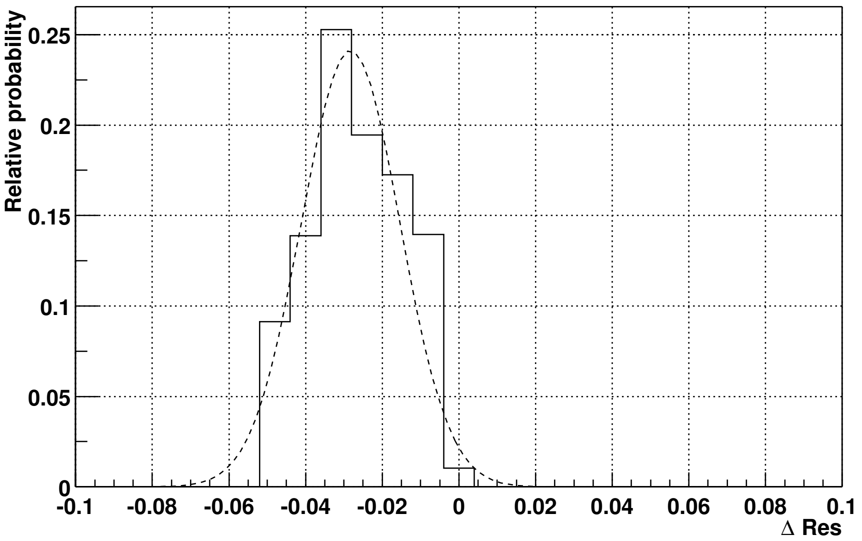

Figure 6.15: Deviation in energy resolution weighted by volume for ^{16}N calibration runs.

6.5 Calibration of Neutron Capture Events

An additional data set with which to test the energy calibration function are the γ-rays from neutron capture on ^{2}H. This is a good test of the energy calibration since the γ-rays are mono-energetic and are released directly into the D_2O without any encapsulating source such as the stainless steel ^{16}N chamber. Shown in figure 6.16 are the calibrated energy spectra for a ^{252}Cf calibration run at the detector center, along with the result of a similar Monte-Carlo calculation. After applying the energy calibration the spectra agree very well with a difference in the centroids of only about 0.3 %. We are thus confident that the systematic uncertainties involved with the Monte-Carlo calculations for the ^{16}N decays and source chamber are small. Work by Hamer [18] has shown that such systematic uncertainties due to uncertainties in modeling the source are less than $\sim$ 0.3% and the total uncertainty including uncertainty in the ^{16}N decay scheme and uncertainty in the tracking of γ-rays and electrons by EGS is less than $\sim$ 0.5%.

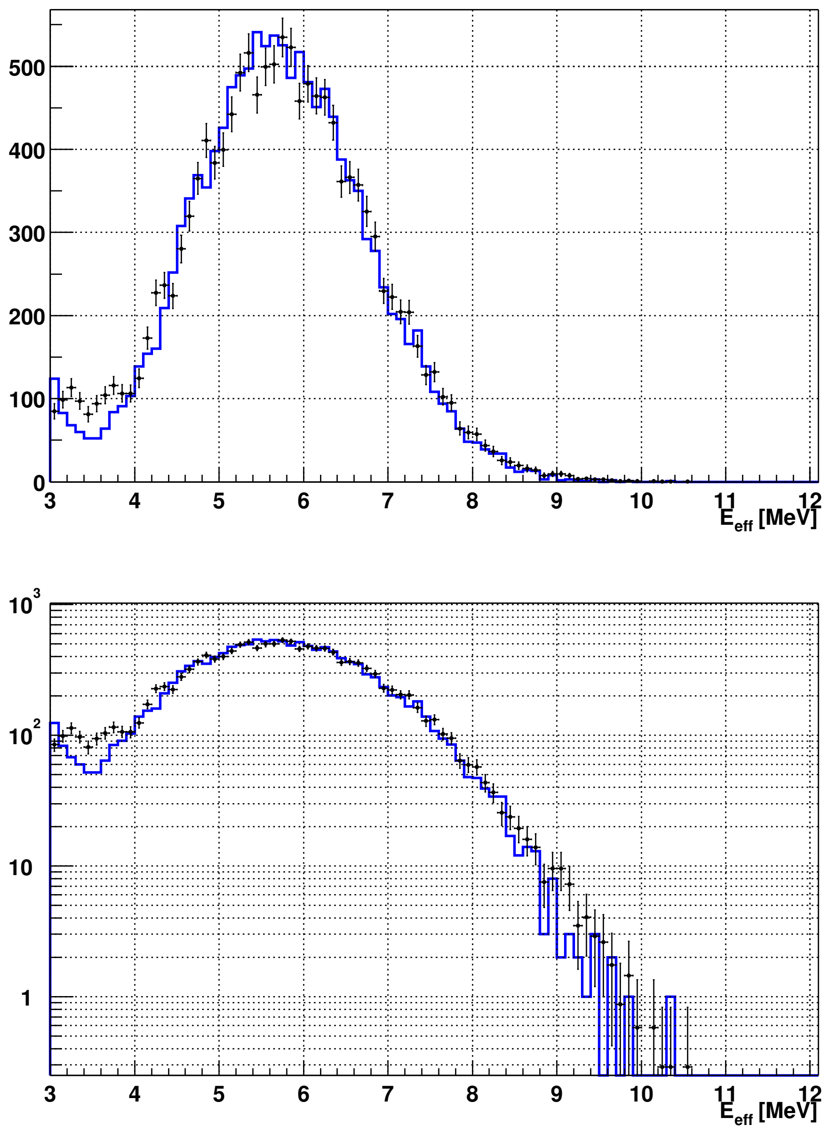

Figure 6.16: E_{eff} spectra for neutron capture γ-ray events. Shown are the Monte-Carlo result (line) and the spectrum from a ^{252}Cf calibration run at the detector center. We have selected events with $200 < R_{fit} < 540$ cm and applied the energy calibration processor (RSP). The centroids of these distributions agree to within 0.3%.

6.6 Systematic Uncertainties in Derived Solar Neutrino Fluxes

Based on the results of the previous sections, we assign conservative 1σ uncertainties on the absolute energy scale and resolution of SNO of

$$\frac{\sigma_E}{E} \approx 0.02 \tag{6-14}$$

$$\frac{\sigma_{\mathcal{R}}}{\mathcal{R}} \approx 0.05 \tag{6-15}$$

We can study the effect of these uncertainties on measuring neutrino rates in SNO by calculating the predicted E_{eff} spectra as described above and measuring the derivative of the integrals of these spectra above a given threshold as we vary the energy scale and resolution. This will tell us the uncertainty on a derived flux were we to measure such a spectrum in isolation from all other events in SNO. A more general study is presented in chapter 9 where the additional effects of separating several signals are considered.

We take here the example of charged-current interactions in SNO due to ^{8}B solar neutrinos. Ignoring any spectral shape distorting effects such as MSW, the predicted E_{eff} spectrum for these events is given by (see chapter 9 for details)

$$\frac{dN}{dE}(E) = \int_0^\infty \Phi(E_\nu)\frac{d\sigma_{cc}}{dE}(E_\nu, E_{e^-})R(E, E_{e^-})dE_\nu \tag{6-16}$$

and the event rate above a given threshold is then given by

$$R_{CC} = \int_{E_{thres}}^{\infty} \frac{dN}{dE}(E)dE \tag{6-17}$$

Similar expressions can be used to calculate the ES event rates. These spectra are shown in figure 6.17. For reference, a Monte-Carlo calculation of CC events is shown in figure 6.18, along with the energy spectrum calculated above. Also shown are spectra for energy resolution at ± 10 % of its nominal value.

The derived uncertainties in the CC and ES fluxes due to uncertainties in the absolute energy scale are shown in table 6.2, where we have assumed fractional uncertainties on the energy scale of 1 and 2σ as defined by equation 6-14.

Table 6.3 shows the uncertainty in the fluxes arising from uncertainty in the energy resolution defined by equation 6-15. We can see that the uncertainty due to energy resolution is small compared to that for uncertainty in the energy scale.

Threshold [MeV]	$\frac{\Delta F}{F}_{CC}$	$\frac{\Delta F}{F}_{ES}$	$\frac{\Delta F}{F}_{CC}$	$\frac{\Delta F}{F}_{ES}$
	$\frac{\Delta E}{E} = 2\%$		$\frac{\Delta E}{E} = 4\%$	
5	0.014	0.031	0.029	0.065
6	0.026	0.044	0.054	0.090
7	0.042	0.06	0.085	0.120
8	0.065	0.08	0.130	0.16
9	0.096	0.10	0.190	0.20
10	0.139	0.142	0.28	0.27

Table 6.2: Uncertainties in neutrino fluxes due to uncertainty in the energy scale.

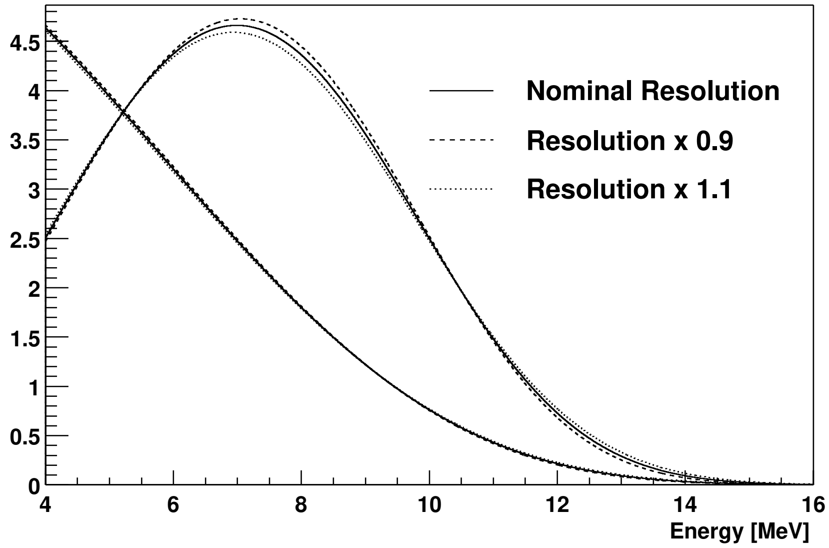

Figure 6.17: Calculated energy spectra for CC and ES events in SNO, with arbitrary normalization. Shown are the results for the nominal energy resolution from figure 6.6, as well as for ±10% shifts in the resolution width.

Threshold [MeV]	$\frac{\Delta F}{F}_{CC}$	$\frac{\Delta F}{F}_{ES}$	$\frac{\Delta F}{F}_{CC}$	$\frac{\Delta F}{F}_{ES}$
	$\frac{\Delta \mathcal{R}}{\mathcal{R}} = 5\%$		$\frac{\Delta \mathcal{R}}{\mathcal{R}} = 10\%$	
5	0.0027	0.00097	0.0052	0.0021
6	0.003	0.0002	0.0065	0.0065
7	0.003	0.0022	0.0057	0.0036
8	0.0005	0.0055	0.002	0.0095
9	0.0048	0.010	0.0068	0.019
10	0.015	0.019	0.025	0.034

Table 6.3: Uncertainties in neutrino fluxes due to uncertainty in energy resolution.

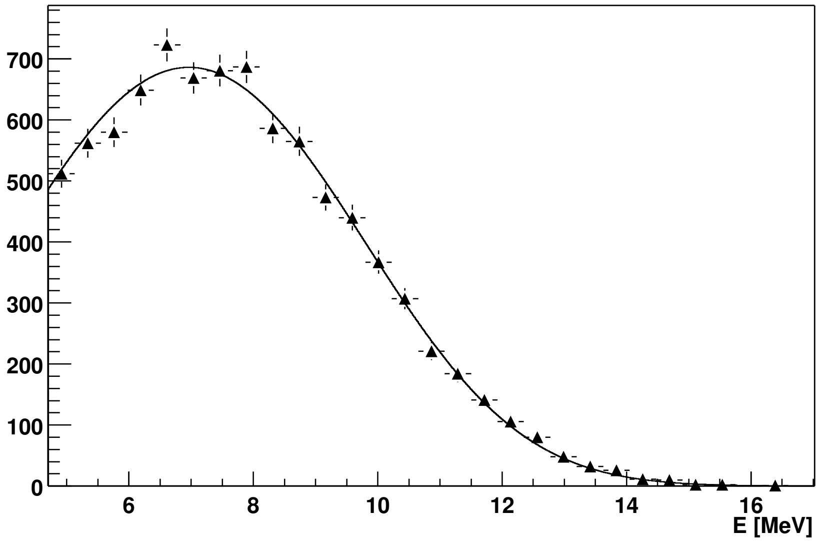

Figure 6.18: Calculated CC energy spectrum in SNO (line) and that generated from a SNOMAN Monte-Carlo calculation (points).

Chapter 7

Data Reduction

This section describes the set of cuts applied to the raw data to remove non-solar neutrino events from the data set. During the commissioning phase of the SNO detector, several classes of instrumental backgrounds were found. In this section we describe the types of backgrounds present in the SNO dataset and the cuts used to identify and remove them.

The data-cleaning cuts have been divided into two passes. The first pass applies simple data reduction algorithms which target specific classes of non-neutrino events. These cuts use easily calculated parameters and event hit patterns and are thus not very computationaly intensive. The second pass involves reconstructing the event vertex, and discarding events which either have a poorly reconstructed vertex or reconstruct outside of the volume selected for analysis.

7.1 First Pass Data Reduction

In this section a set of cuts are described which target classes of events which are not due to solar neutrinos. These events are due either to backgrounds associated with the physical detector instrumentation such as flashing PMTs, noise in the electronics subsystems, light associated with the acrylic vessel or other physics events such as muons or their spallation products. The cuts were developed during the commissioning phase of the detector as the various detector pathologies were being uncovered and have been divided into categories based on the primary type of background that the cut is intended to remove. In the following subsection each cut class is described along with the associated identification algorithm. In section 7.2 the effect of applying this set of cuts to valid calibration data is determined, where we find that effectively none of the valid Čerenkov events are removed by the data reduction cuts.

7.1.1 Flasher Event Cuts

Large PMT Pulses

Events which contained large PMT pulses were removed from the data set. These pulses are mostly associated with flashing PMTs, and are thought to be due to discharges in the PMT dynode chain or base. These produce a very large electrical pulse which is seen in the PMT and adjacent channels. Many photons are also generated which travel across the detector.

Figure 7.1 shows the summed charged spectra (in raw ADC counts) for a ^{16}N calibration run. Events with ADC counts outside of the range 350 to 4000, which correspond to pulses greater than about 200 photoelectrons, were considered to contain anomalously large PMT charges. To be tagged as an invalid event, the large

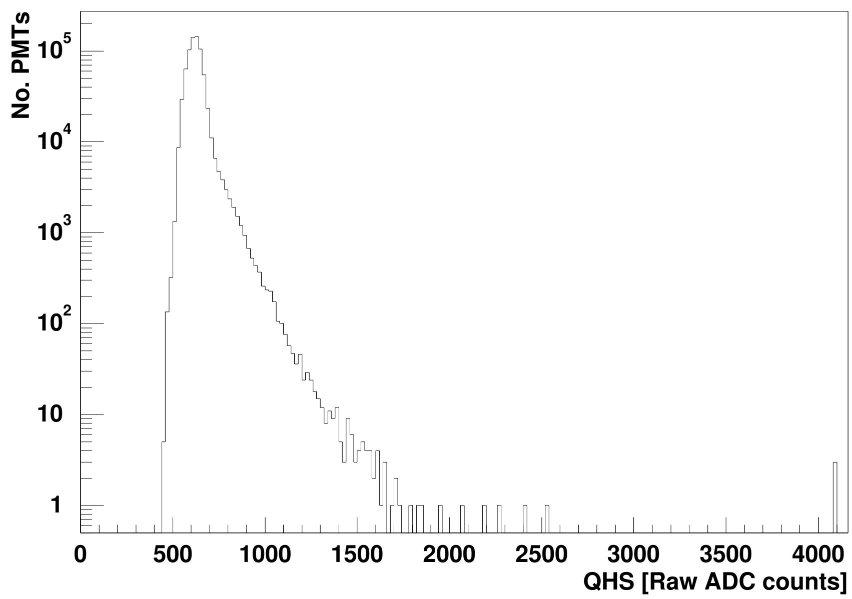

Figure 7.1: Summed PMT charge spectra from a ^{16}N calibration run.

pulse tube was also required to have a valid charge calibration, with the calibrated charge < -250. The railed PMT was also required to be within 250 and 60 ns earlier than the median PMT time in the event. This last requirement makes this cut less sensitive to incorrect charge measurements due to malfunctioning electronics.

Analog Measurement Board Cut

The analog sum of all phototube pulses is used to tag events which contain anomalously large charges. This event identification can be viewed as a normal (single-PMT) charge cut which becomes increasingly less efficient as the event energy increases. The cut algorithm used in this analysis is identical to the AMB cut in SNOMAN [32].

7.1.2 Neck Event Cuts

A class of events has been identified in SNO which appears to be due to light originating in the AV neck. To aid in identifying these events, four PMTs were installed in the AV neck. Events are tagged as NECK events if two or more of these NECK PMTs have fired.

7.1.3 Burst Cuts

The solar neutrino signal in the detector is on the order of tens of events per day. Bursts of events due to either flashing PMTs, seismic noise or noise in the electronics system can be removed from the dataset without affecting the solar neutrino signal. The basic algorithm for identifying a burst is to search for N_{events} or more events (with a minimum Nhit threshold of N_{thresh}) within a time window T_{win}. Once a burst was identified, all data within T_{cut} was removed from the data set. Three sets of parameters were defined to remove re-trigger bursts, large Nhit bursts, and high trigger rate bursts. Table 7.1 shows the values of these parameters for these three burst cuts.

Name	N_{events}	N_{thresh}	$T_{win}[nsec]$	$T_{cut}[nsec]$
Re-trigger	2	0	1000	100000
High Nhit	40	20	1e9	1e9
High Rate	2	60	1e8	1e9

Table 7.1: Burst cut parameters used in the data reduction algorithms.

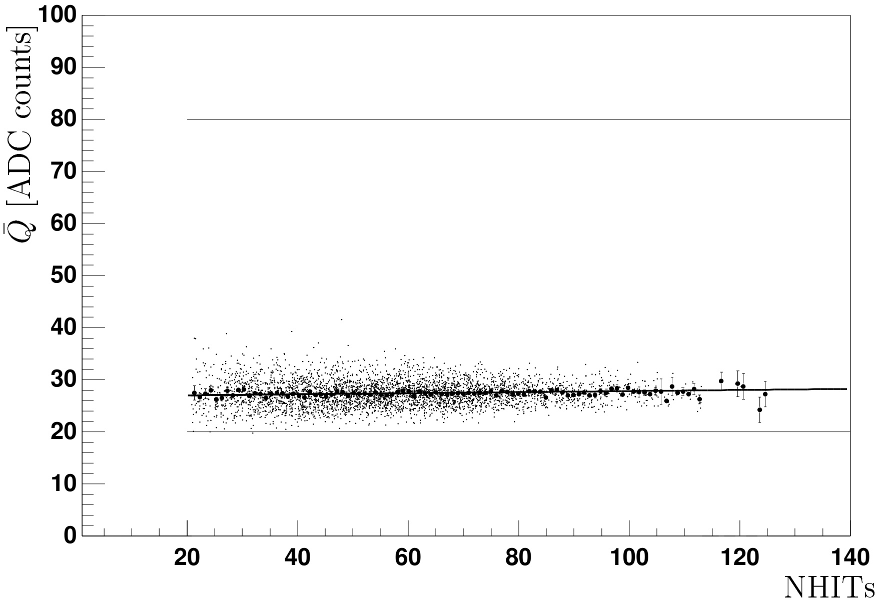

Figure 7.2: Average charge cut applied to Monte-Carlo CC events.

7.1.4 Electronics Induced Noise Cuts

Average Detected Charge

Events were removed from the data set in which the average PMT charge was much different than that expected for Čerenkov events in our energy region of interest. Figure 7.2 shows the average PMT charge in ADC counts predicted by SNOMAN for solar neutrino charged current events. The single p.e. peak is near channel 20. Events are cut if the average charge is outside the range 20 to 80 ADC counts, which corresponds to a range of 1 to 4 photons per PMT since genuine Čerenkov events are in this range. Figures 7.3 and 7.4 show a similar plot for ^{16}N calibration runs at the detector center, and at z = -570 cm respectively. This cut removes << 0.1 % of valid events.

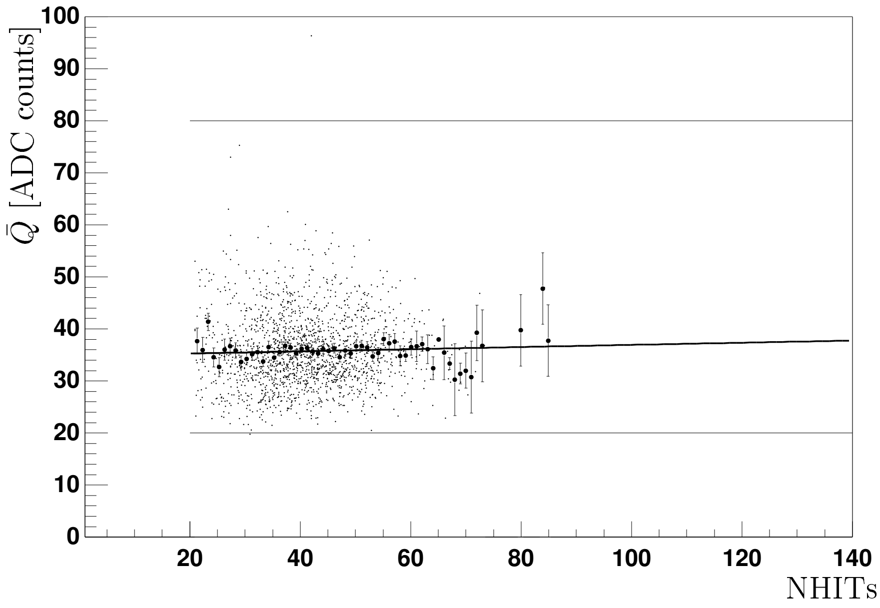

Figure 7.3: Average charge cut applied to ^{16}N events with source at detector center.

Electronics Hit Density

This cut predominantly removes events associated with pickup in the electronics or associated hardware. Events are removed which contain a high density of hits on a single electronics paddle card, which carries 8 PMT signals to a multiplexing motherboard. Figure 7.5 shows the maximum number of hits per paddle card for an ^{16}N calibration run, and SNOMAN Monte-Carlo of charged current neutrino events. By removing events with 7 or more hits per paddle card, we remove an insignificant fraction ($\ll 0.1\%$) of calibration or Monte-Carlo events.

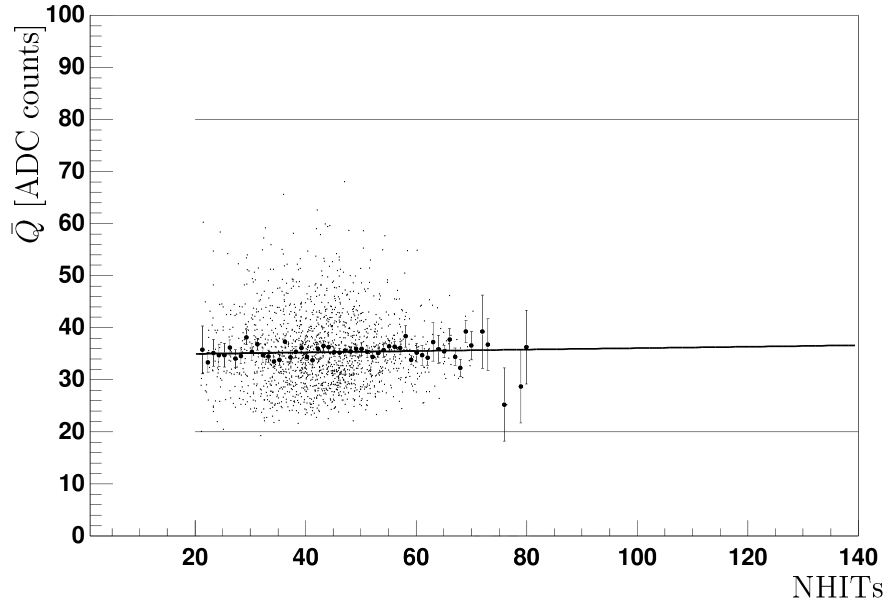

Figure 7.4: Average charge cut applied ^{16}N events with source at z = -570 cm.

7.1.5 Muons and Spallation Products

Muon Cut

SNO observes approximately 3 through-going muons per hour. The muon cut tags muons and imposes a dead time following this muon to remove any spallation products from the neutrino data set. The current algorithm (identical to the default SNOMAN muon ID) requires 5 or more outward looking (OWL) tubes to fire, as well as a 150 or more inward looking PMTs with an RMS time of less that 90 ns. Twenty seconds of dead time is imposed following each identified muon to remove spallation products following muon events.

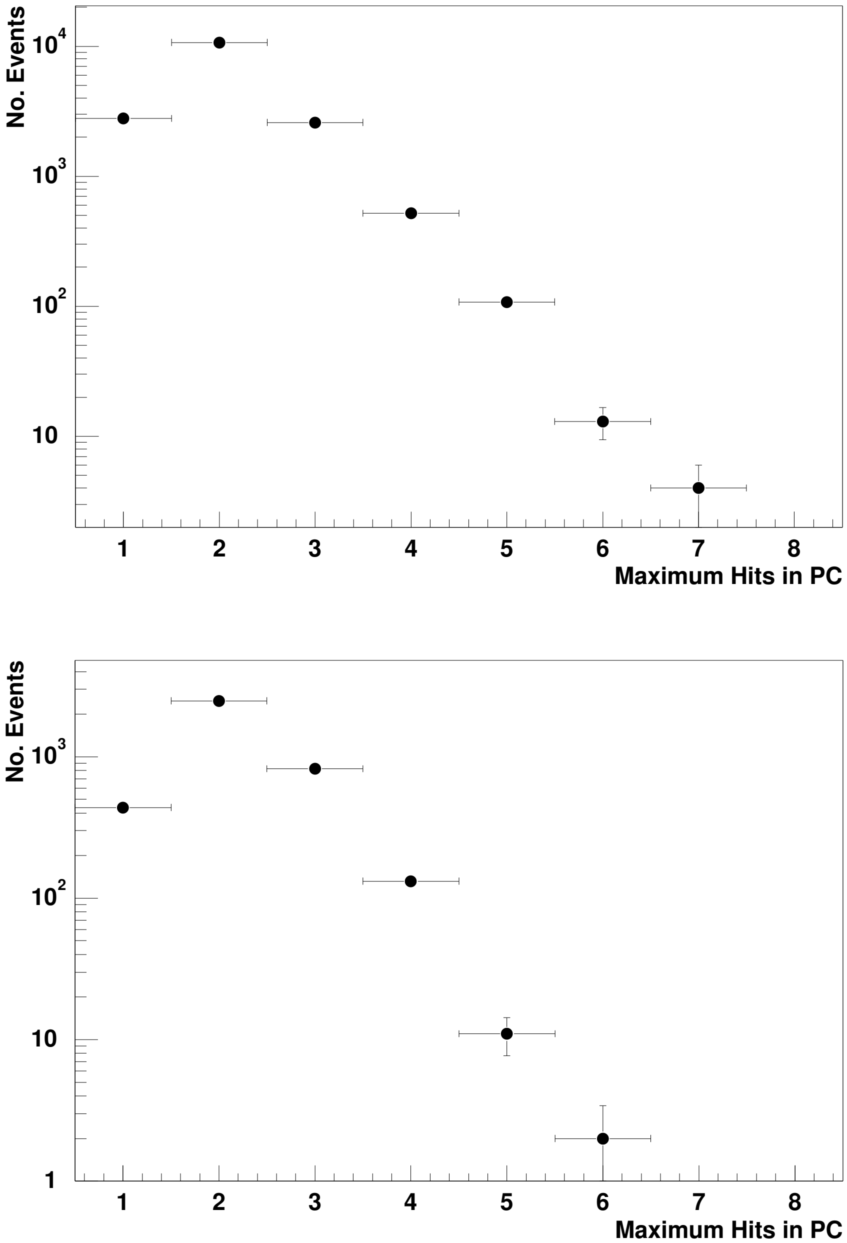

Figure 7.5: Maximum number of hits in one electronics paddle card for a calibration run (top frame) and Monte-Carlo events (bottom frame).

Outer Detector Activity

This cut is used to identify events associated with activity outside of the fiducial volume of the detector. Events are identified based on the number of outward looking PMTs which have fired. Table 7.2 shows the cut parameters used.

Min BUTTs	Min OWLs	Min BUTTs+OWLs
2	5	5

Table 7.2: Parameters used in the outer detector cut.

7.2 Effect of First Pass Cuts on Calibration Data

To determine the effect the first pass data reduction cuts have on genuine Čerenkov signals, the application of the cuts to ^{16}N calibration data is studied. In the context of data reduction we define sacrifice as the fraction of signal events removed by the cuts. The sacrifice versus NHITs is shown in figures 7.6 - 7.8 for ^{16}N source positions in the D_2O and H_2O for all of the first pass cuts. We see that the total sacrifice is small for source positions inside the detector. To estimate the effect the cuts will have on events with energies greater than those from ^{16}N (and up to our maximum energy of interest of around 16 MeV) we make the assumption that the local density of hits on the PSUP is the most important factor in determining the energy bias in the data reduction cuts. This is a valid assumption since the data reduction cuts which may have an energy bias are those which use hit clustering on the PSUP to identify non-Čerenkov events. We can thus study ^{16}N data for the source outside of the inner fiducial volume region which will lead to a greater density of phototube hits on the PSUP (since the source is nearer the PSUP) and then determine the equivalent energy of an event at our fiducial volume boundary for this increased hit density. The measured sacrifice can then be inferred for this increased event energy. We can thus infer from figure 7.10 that the sacrifice for events at a radius of 540 cm is around 3 % for events with NHITs given by

$$\begin{aligned} \text{NHITs} &= (\frac{700}{540})^2 \times 80 \text{ NHITs} \\ &= 134 \text{ NHITs} \end{aligned}$$

We will thus estimate that the maximum uncertainty in sacrifice is 3% for events inside a radius of 540 cm, with NHITs <= 134. Since this is near the highest energy region of our solar neutrino signal, the effect of data reduction sacrifice on the solar neutrino analysis is small and can be ignored.

Figure 7.6: Measured sacrifice for the first pass data reduction with the source at the detector center.

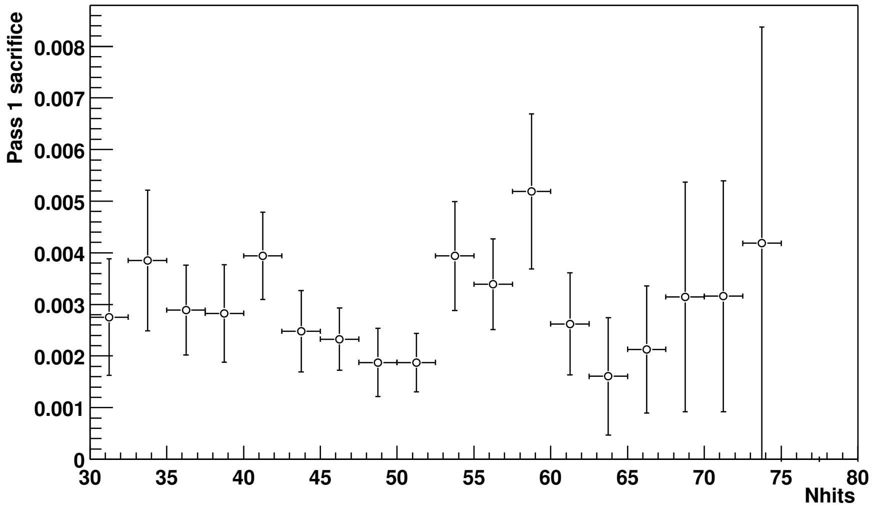

Figure 7.7: Measured sacrifice for the first pass data reduction with the source at r=500 cm.

7.3 Second Pass Data Reduction

After the first pass data reduction has been applied, the data are reconstructed using the techniques described in chapter 4 to determine their position and direction in the detector. Events which reconstruct outside of the fiducial volume selected for analysis are removed from the data set. Two additional cuts are also imposed based on information derived from the fit vertex and hit pattern of the event. Events are considered good if the fraction of phototubes in the prompt peak satisfies

$$q_{fit} \equiv \frac{N_{win}}{\text{NHITs}} \geq 0.6 \tag{7-1}$$

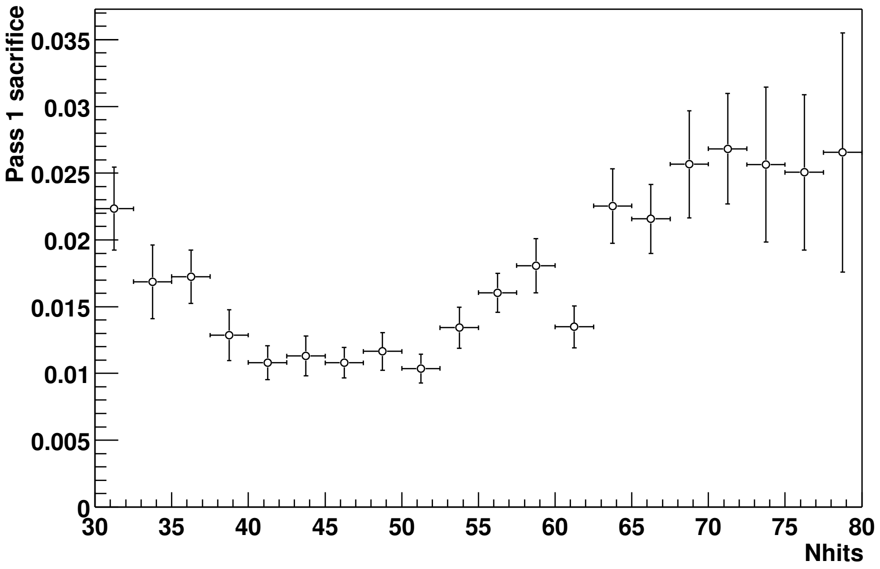

Figure 7.8: Measured sacrifice for the first pass data reduction with the source at r=650 cm.

where

N_{win}	is the number of hits in the 20 ns in-time window,
NHITs	is the total number of hits.

This cut will remove non-Čerenkov events from the data set not removed by the first pass data reduction. A test with the ^{16}N calibration source in the heavy water shows that this cut removes less than 0.1% of ^{16}N calibration events, as shown in figure 7.11.

A parameter proposed by Chen [33] to measure event isotropicity is also used in the second pass data reduction. The isotropicity parameter is defined as $\bar{\theta_{ij}}$ and is the average angle as measured from the reconstructed vertex between all pairs of PMTs in the event which are within the prompt 20 ns window. This parameter thus

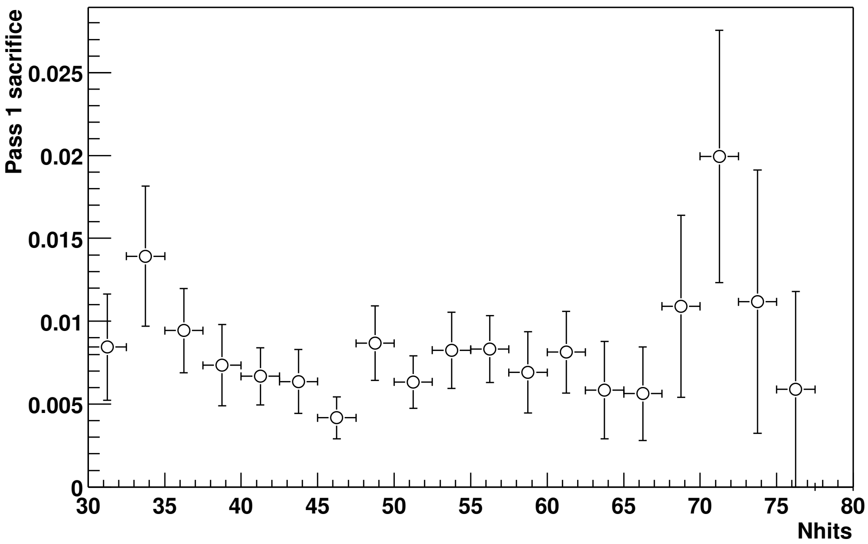

Figure 7.9: Measured sacrifice for the first pass data reduction with the source at r=650 cm and $R_{fit} <= 650$ cm.

increases for increasingly isotropic events. We will reject events for which

$$\bar{\theta_{ij}} < 0.8 \tag{7-2}$$

This cut removes an insignificant fraction of ^{16}N calibration events as shown in figure 7.12, but is useful in rejecting events which misreconstruct far from the true vertex and thus have an abnormal value of $\bar{\theta_{ij}}$.

7.4 Alternative Data Reduction

The data reduction algorithms described in the previous sections were implemented by the author and used in the analysis presented in this thesis. An alternate set of

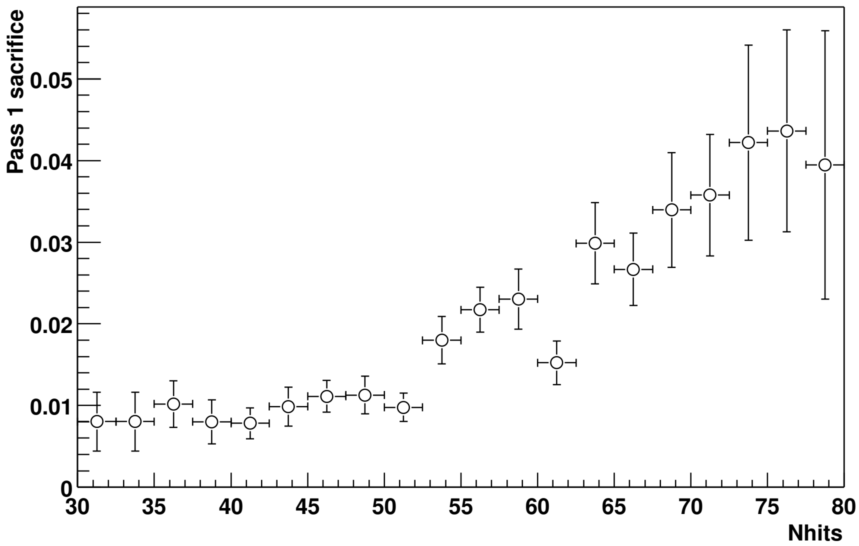

Figure 7.10: Measured sacrifice for the first pass data reduction with the source at r=650 cm, and with 675 < Rfit < 725 cm.

data reduction algorithms has been implemented by the SNO collaboration. As a cross-check we have applied both data reduction sets to the SNO data sets described in chapter 10. The comparison of both sets of cuts is shown in table 7.3, where the cuts used in the work are labelled QSNO and the alternative cuts are labelled DAMN. We see that the set of events selected for analysis using the two different data reduction techniques are nearly identical.

Bifurcated analysis methods using orthogonal data reduction cuts to cross calibrate each other have been used in SNO to estimate the cut efficiencies. Studies using these techniques have shown that leakage of all the known types of instrumental background events into the final data set are small [34]. We will thus ignore instrumental backgrounds in the solar neutrino analysis.

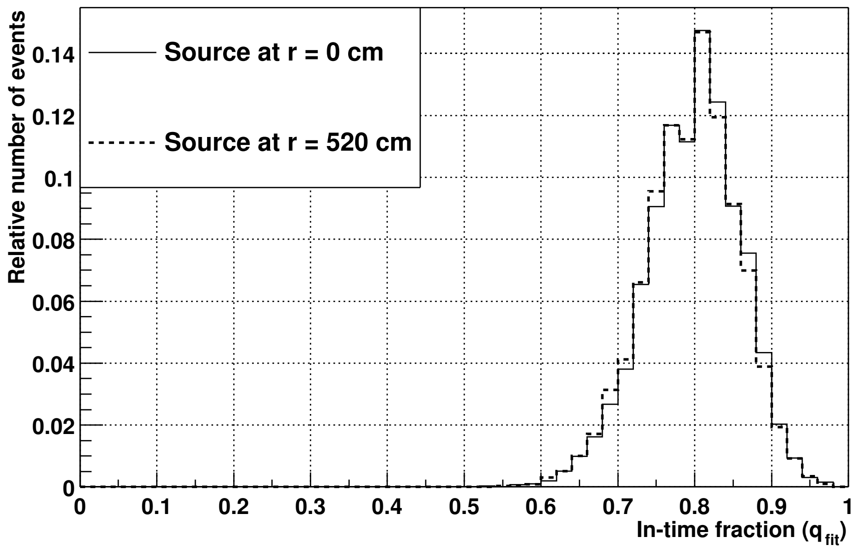

Figure 7.11: In-time fraction (q_{fit} defined by equation 7-1) for ^{16}N calibration data in the heavy water region. We note that removing events with $q_{fit} < 0.6$ removes less than 0.1% of the ^{16}N events for points inside the D_2O.

Applied cut set	Number of selected events
DAMN	954
QSNO	968
Cut by QSNO but not by DAMN	0
Cut by DAMN but not by QSNO	14

Table 7.3: Comparison between the QSNO (cuts discussed in this chapter) and DAMN (alternative) data reduction cuts. We find that application of the DAMN cuts reduces the data set to nearly that for the QSNO cuts presented in this chapter.

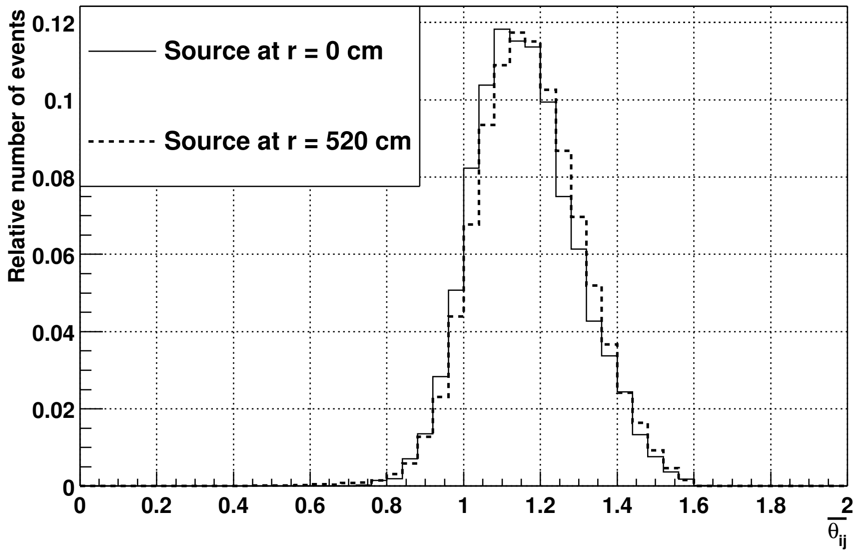

Figure 7.12: $\bar{\theta_{ij}}$ cut applied to ^{16}N calibration data in the heavy water region. We note that a cut on $\bar{\theta_{ij}} < 0.8$ removes effectively none of the ^{16}N events for points inside the D_2O.

Chapter 8

Radioactive and Cosmic Backgrounds

The energy threshold used in analysis of the neutrino signals is primarily determined by the contamination of the low energy region by radioactive decays in the detector materials. A large effort on the part of the SNO collaboration has been placed in assuring the concentration of radioactive contaminants in all detector materials is low. The approach taken in this analysis is to use Monte-Carlo calculations based on the measurements of the radioactive contaminations in the detector materials and choose an analysis threshold based on this study such that the contamination above that threshold is a small fraction of the neutrino signal. In this chapter we show that for an analysis threshold of $E_{eff} \geq 6$ MeV the only significant backgrounds predicted by the Monte-Carlo calculations are due to neutron captures on ^{2}H. These neutron backgrounds are dealt with explicitly in the solar neutrino analysis.

The naturally occurring radionuclides we are concerned with are the ^{232}Th and ^{238}U chains. We are concerned with these backgrounds for two reasons. Radioactive decays in the above chains will directly set a limit on the low energy threshold we can use for analysis since the finite detector energy and spatial resolutions will allow a fraction of these events to be a background to the solar neutrino events. Some decays in these chains can also lead to free neutrons in the D_2O, since a γ-ray with energy greater than 2.223 MeV can photo-disintegrate the deuteron. These free neutron background events are indistinguishable from those due to neutral current neutrino interactions and we must thus subtract the rate of these events from our measured neutral current rates. The only decays in the naturally occurring radionuclides which can lead to such gammas are those of ^{214}Bi (from the ^{238}U chain) and ^{208}Tl (from the ^{232}Th chain). The design specifications of SNO called for ^{232}Th and ^{238}U contaminations which limit the total number of free neutrons generated in the D_2O to one per day, which is approximately 8% of the standard model solar neutrino signal.

If we assume these daughters are in secular equilibrium with their long-lived parents, we can write $\omega_A N_A = \omega_B N_B$, where ω is the radioactive decay rate, N is the number of radioactive atoms. A and B refer to the parent and daughter respectively. We thus expect

$$1075\ {}^{214}\text{Bi decays/day/}\mu\text{g of }{}^{238}\text{U, and} \tag{8-1}$$

$$351\ {}^{208}\text{Tl decays/day/}\mu\text{g of }{}^{232}\text{Th.} \tag{8-2}$$

From the decay schemes of ^{208}Tl and ^{214}Bi, we have the number of γ-rays capable of photo-disintegrating the deuteron are given by

$$16.5\ {}^{214}2.445 \text{ MeV } \gamma\text{-rays/day per } \mu\text{g of U} \tag{8-3}$$

$$126\ {}^{208}2.614 \text{ MeV } \gamma\text{-rays/day per } \mu\text{g of Th} \tag{8-4}$$

An intensive effort on the part of the SNO collaboration has been placed on keeping the radioactivities of detector materials low and on accurately measuring the contamination levels of these materials. The heavy and light water inside the PSUP region are regularly assayed for uranium and thorium. Figures 8.1 and 8.2 show the results of such assays for the periods between May 1999 and April 2000 [35].

The concentrations of contaminants in the acrylic vessel and phototubes have also been measured. Shown in tables 8.1-8.2 are the design specifications for concentrations of ^{232}Th and ^{238}U in the SNO detector materials near our sensitive detector region [36, 37], along with the measured concentrations [38, 39, 35, 40] averaged over the data set we will use for solar neutrino analysis.

	D_2O (10^{-14} g/g)	Acrylic (10^{-13} g/g)	H_2O (10^{-13} g/g)	Phototubes (μg/PMT)
Target	4.5	3.0	4.5	75
Actual	$< 0.5^1$	$< 0.73^2$	1.5 $\pm$2	< 75
Mass	$< 5\ \mu$g	$< 2\ \mu$g	$250 \pm 333\ \mu$g	< 730 mg

Table 8.1: Contamination levels of ^{238}U in our detector materials. ^{1}Upper limit. $^2 2\sigma$ limit.

In the following sections we will discuss the contributions to the neutrino background from each of the detector materials (D_2O, H_2O, the acrylic vessel, and the phototubes).

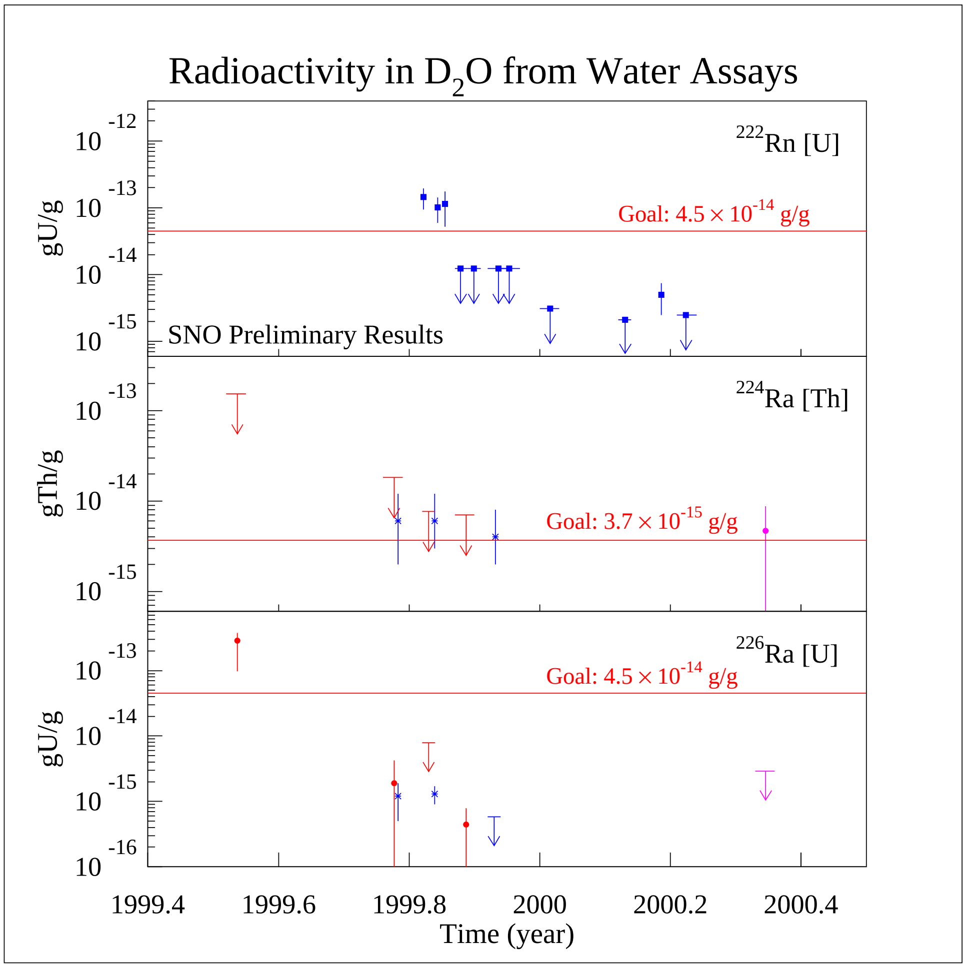

Figure 8.1: Assay results showing the D_2O contamination levels.

8.1 $\beta - \gamma$ Decays in Detector Materials

To study the effects of radioactive contamination of the detector materials, we have a performed a set of Monte-Carlo calculations with event rates given by the measured contamination levels. Table 8.3 shows the total number of ^{214}Bi and ^{208}Tl decays we expect in the dataset described in chapter 9 (approximately 141 live days) for the contaminations of tables 8.1 and 8.2.

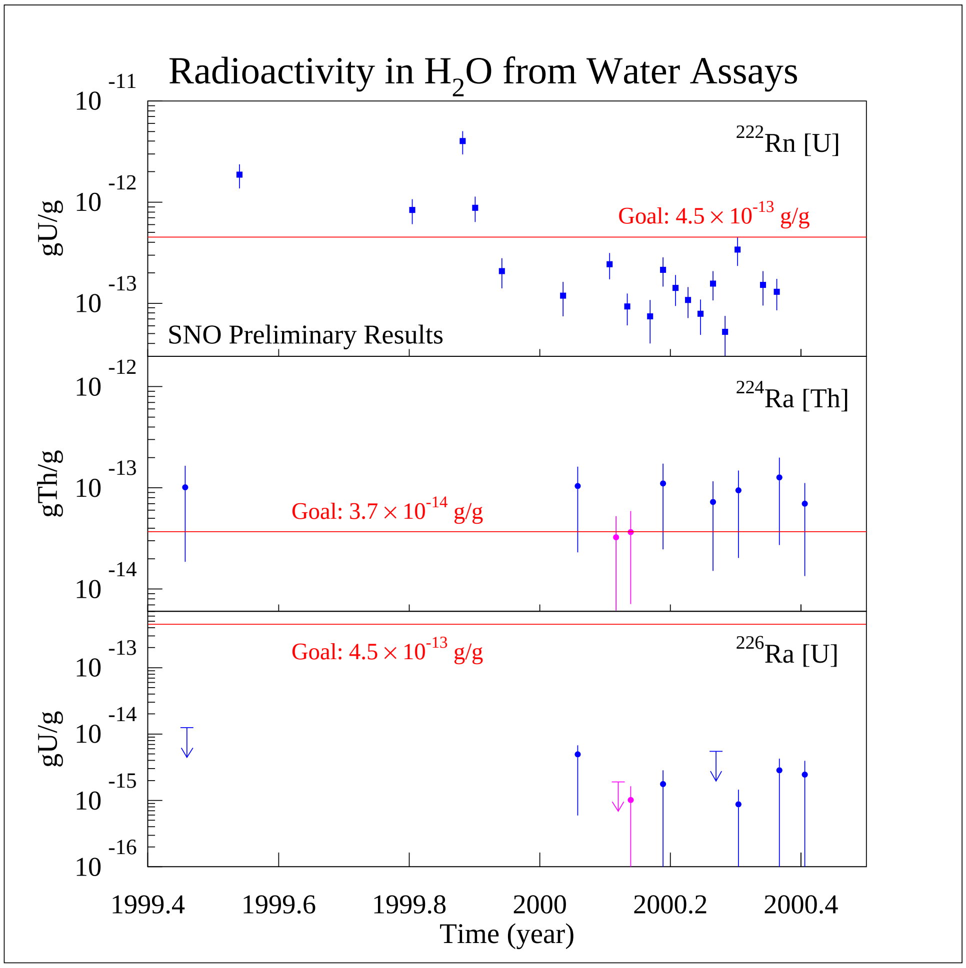

Figure 8.2: Assay results showing the H_2O contamination levels.

An important component of the low-energy radioactive background which reconstructs inside the fiducial volume of the SNO detector is due to $\beta - \gamma$ events within the D_2O. These internal decays are the dominant source of low energy background near threshold since they are in our sensitive detector region. Figure 8.3 shows the calculated energy spectra for events which reconstruct inside our fiducial volume from Monte-Carlo calculations for ^{214}Bi and ^{208}Tl decays in the D_2O region.

The next closest material to our sensitive volume is the acrylic vessel. The mea-

	D_2O (10^{-15} g/g)	Acrylic (10^{-12} g/g)	H_2O (10^{-14} g/g)	Phototubes (μg/PMT)
Target	3.7	7	3.7	75
Actual	$3.7^{+4.3}_{-3.7}$	$< 0.11^2$	8^{+4}_{-8}	< 75
Mass	$3.7^{+4.3}_{-3.7}$ μg	< 3 μg	133^{+67}_{-133} μg	< 730 mg

Table 8.2: Contamination levels of ^{232}Th in our detector materials. [1]Upper limit. [2]2σ limit.

	D_2O	Acrylic	H_2O	Phototubes
^{214}Bi decays	7.55×10^5	3.04×10^6	3.78×10^7	1.10×10^{11}
2.445 MeV $\gamma's$	11 627	46 816	582 120	1.69×10^9
^{232}Th decays	65 698	53 908	2 367 950	3.60×10^{10}
2.614 MeV $\gamma's$	23 651	19 407	852 462	1.30×10^{10}

Table 8.3: Number of ^{214}Bi and ^{232}Th decays in our data set for the contamination levels of tables 8.1 and 8.2.

sured concentrations of Th and U in the acrylic are much lower that the original design specifications so that it contributes very little to our low energy background. Shown in figure 8.4 are the energy spectra of ^{208}Tl and ^{214}Bi for a Monte-Carlo data set with the concentrations of tables 8.2 and 8.1.

Monte-Carlo ^{208}Tl and ^{214}Bi decays were generated in the H_2O region with rates from table 8.3. Energy spectra for events from the simulation which reconstruct inside our fiducial volume are shown in figure 8.5. We are less sensitive to decays in the H_2O region since events must mis-reconstruct to enter our fiducial volume.

Table 8.4 shows the integrated number of counts above various energy thresholds determined from the Monte-Carlo calculations of backgrounds in each region. Also shown are the total number of counts from all background sources and the expected number of solar neutrino events above the given threshold and with $E_{eff} < 7$ MeV, for reference. We find the leakage of background events above threshold drops rapidly with increasing energy threshold, and that no background events remain above a threshold of 6 MeV. We thus select a 6 MeV threshold to analyze the solar neutrino data.

E_{thresh}	N_{d2o}	N_{acr}	N_{h2o}	N_{total}	N_{nu}
4.0	1353	76	1139	2569	779
4.5	270	14	255	539	673
5.0	39	2	59	100	533
5.5	3	0	19	22	363
6.0	0	0	0	0	168

Table 8.4: Predicted leakage of background events above threshold.

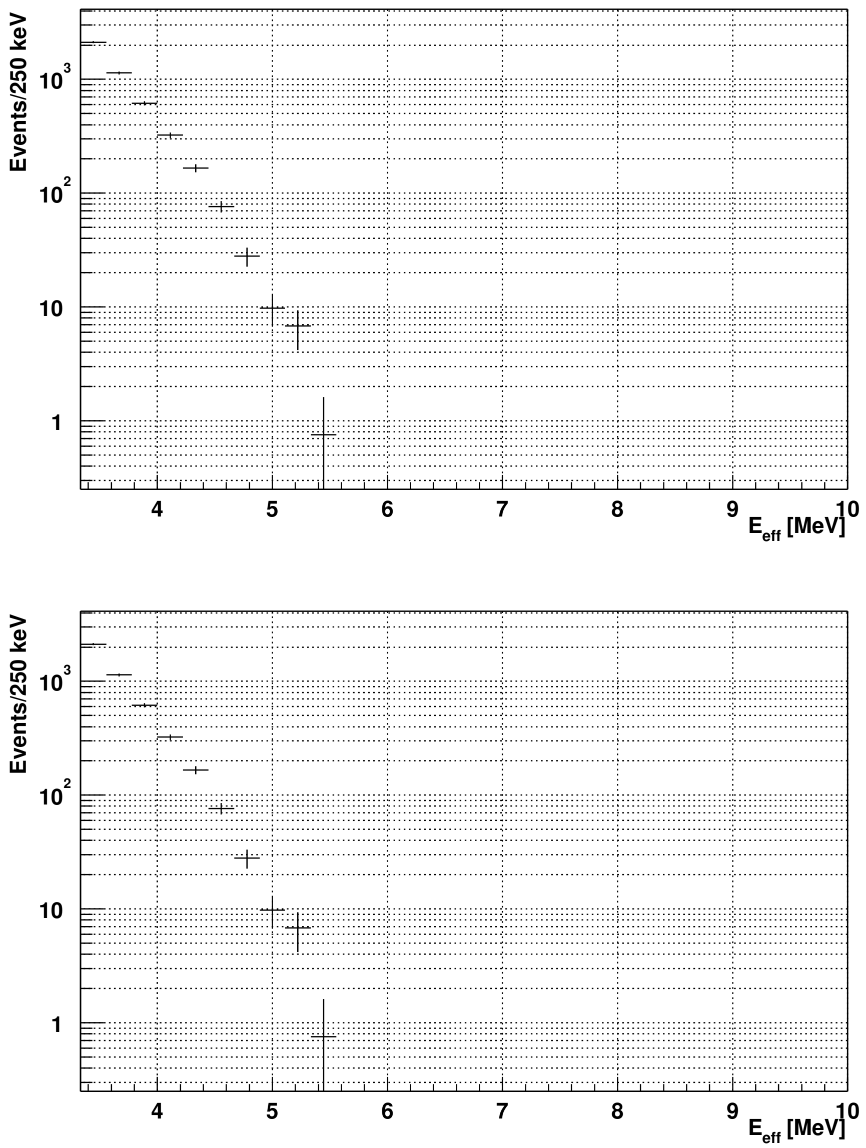

Figure 8.3: SNOMAN Monte-Carlo of ^{214}Bi $\beta-\gamma$'s (top frame) and ^{208}Tl (bottom frame) in the D_2O for the numbers of decays given by table 8.3. Shown are the calculated E_{eff} spectra for events which reconstruct with $R_{fit} < 540$ cm.

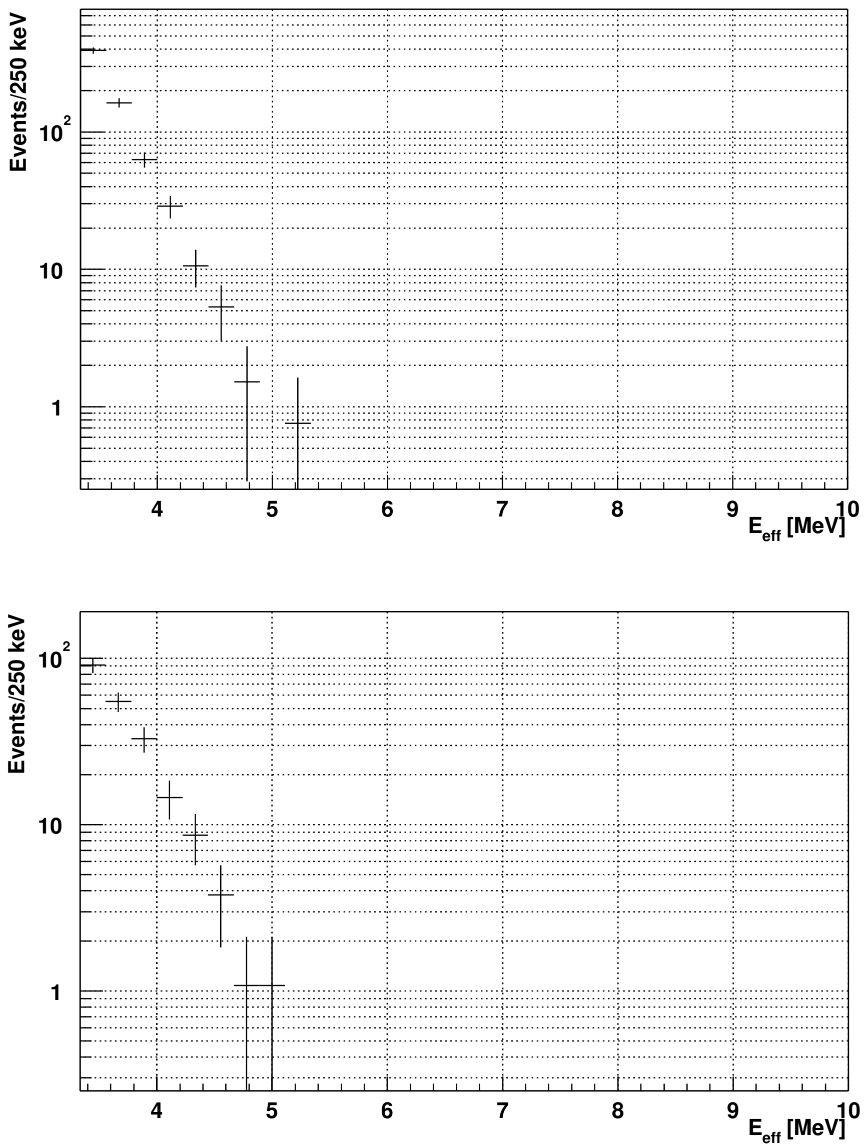

Figure 8.4: SNOMAN Monte-Carlo of ^{214}Bi $\beta - \gamma$'s (top frame) and ^{208}Tl (bottom frame) in the acrylic vessel for the numbers of decays given by table 8.3. Shown are the calculated E_{eff} spectra for events which mis-reconstruct with $R_{fit} < 540$ cm.

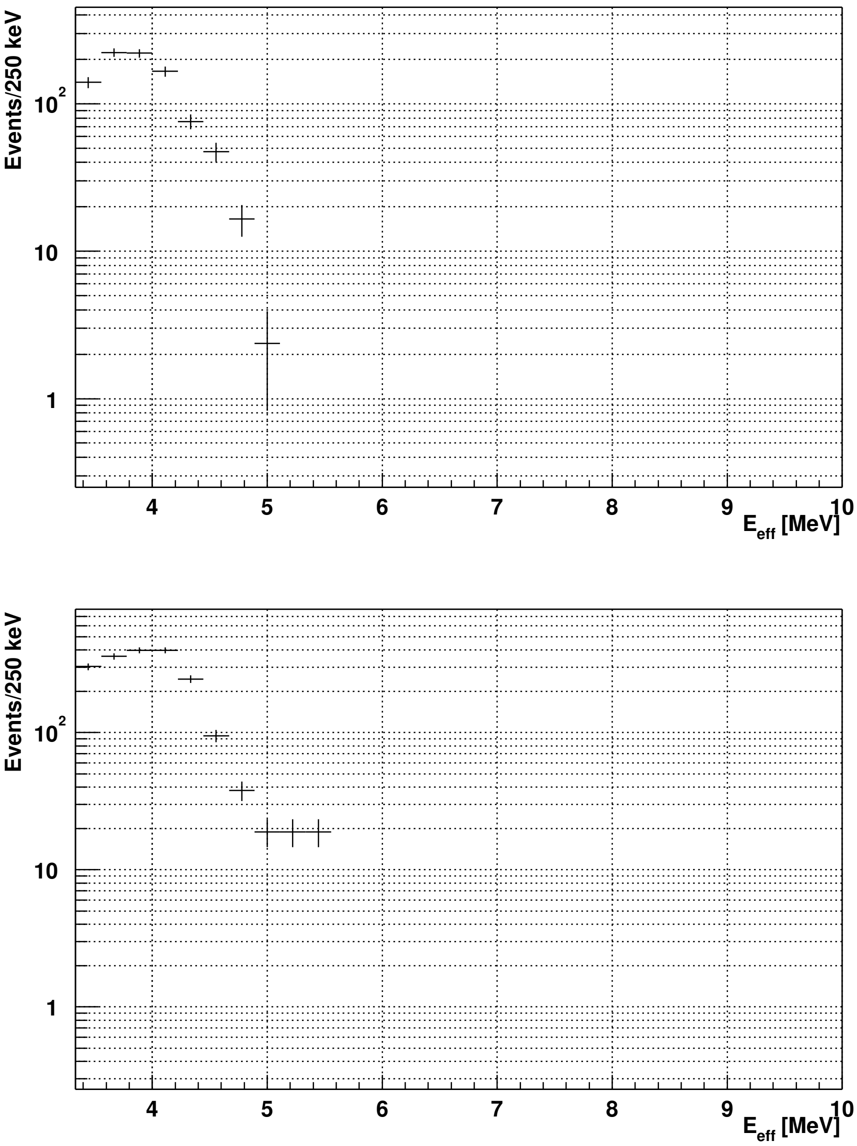

Figure 8.5: SNOMAN Monte-Carlo of ^{214}Bi $\beta - \gamma$'s (top frame) and ^{208}Tl (bottom frame) in the H_2O region for the numbers of decays given by table 8.3. Shown are the calculated E_{eff} spectra for events which mis-reconstruct with $R_{fit} < 540$ cm.

8.2 γ-ray Backgrounds

The light water shielding around the inner volume of the SNO detector will greatly reduce the flux of external γ-rays impinging on the heavy water. A study by Skensved and Robertson [38] has shown contamination from external γ-rays reconstructing into the D_2O is expected to be small. As a cross-check we study the response of SNO to γ-rays from the ^{16}N source near the PSUP and estimate the maximum leakage of γ-ray events into our dataset. The method employed is to use the $\cos\theta_r$ distribution that is characteristic of γ-rays from the PSUP which reconstruct into our fiducial volume to set a limit on the number of external γ-rays in the neutrino data set used for analysis.

Figure 8.6 shows the reconstructed positions projected onto the $Z - X$ plane for the ^{16}N source near the PSUP at $r = 800$ cm. Events which reconstruct into the heavy water region have the $cos\theta_r$ distribution shown in figure 8.7. We define the function P_{mis}

$$P_{mis} = \alpha_{mis}\exp[-\lambda_{mis}\cos\theta_r] \tag{8-5}$$

and fit it to the distribution of figure 8.7 to extract the parameters $\alpha_{mis}, \lambda_{mis}$. To estimate the maximum leakage of external γ-ray events into our dataset, we use the $\cos\theta_r$ distribution for the events selected for solar neutrino analysis, described in chapter 9. We assume this distribution consists of a flat signal component, and a γ-ray background component with a $\cos\theta_r$ distribution as shown in figure 8.7. We thus fit the function

$$P(\cos\theta_r) = \alpha_0 + \alpha_{mis}\exp[-\lambda_{mis}\cos\theta_r] \tag{8-6}$$

with the parameter λ_{mis} fixed to the value derived from the ^{16}N data, and extract the parameters α_0 and α_{mis} to determine the fraction of the $\cos\theta_r$ distribution which is due the background component. We find

$$\alpha_{mis} = 0.08 \pm 0.1 \tag{8-7}$$

which is equivalent to a background (N_γ^{bkg}) component of

$$N_\gamma^{bkg} = 15 \pm 20 \tag{8-8}$$

We thus ignore external γ-ray backgrounds in the solar neutrino analysis.

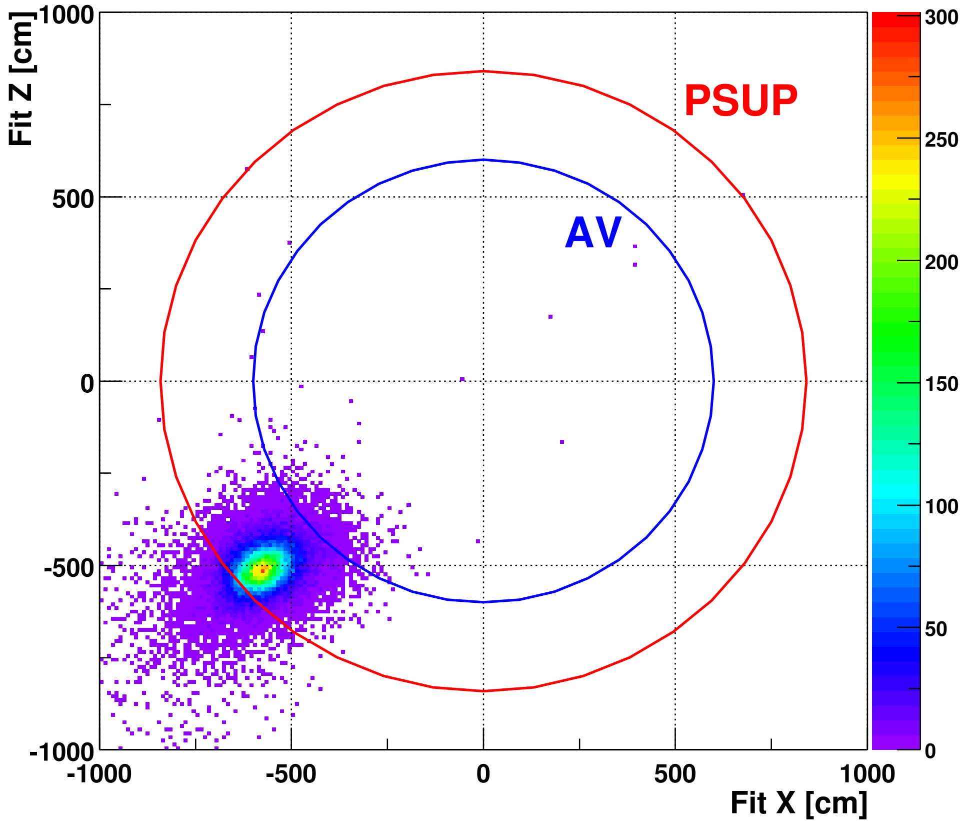

Figure 8.6: Distribution of reconstructed vertices for ^{16}N source near the PSUP at a radius of 800 cm. Shown are the relative numbers of events versus the reconstructed z and x-coordinates for events with NHITs > 20.

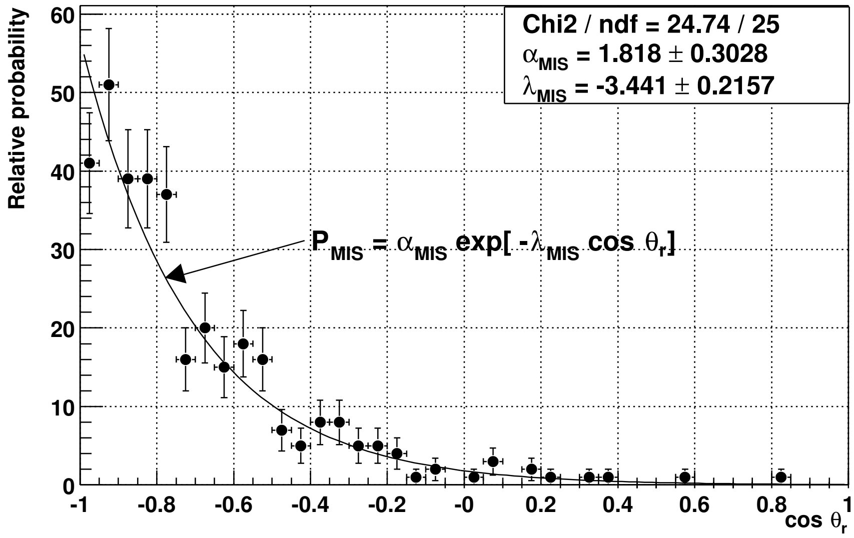

Figure 8.7: Distribution of $\cos\theta_r$ for events which reconstruct into the D_2O region with the ^{16}N source near the PSUP. We see there is a peak for events which reconstruct radially inward.

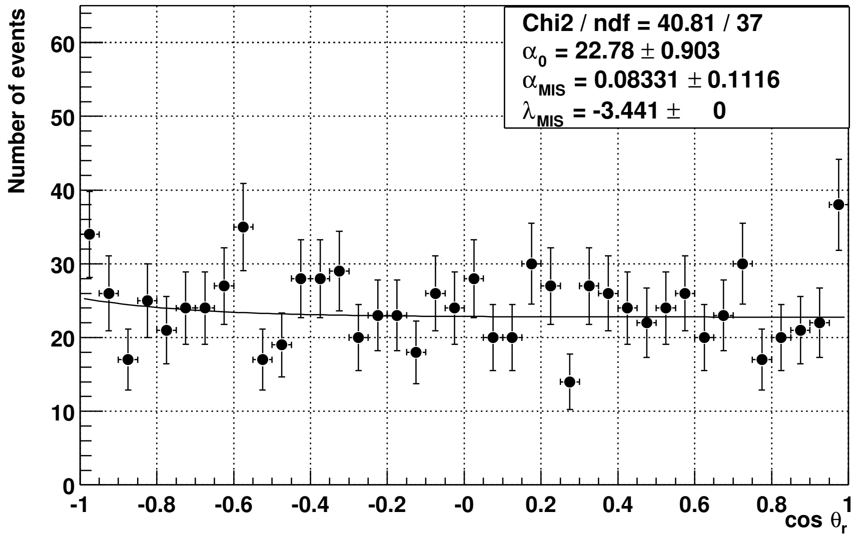

Figure 8.8: Distribution of $\cos\theta_r$ for the SNO data set. The line shows a fit to a flat component and the P_{mis} distribution shown in figure 8.7 were we see there is little leakage from external γ-ray events.

8.3 Neutral Current Backgrounds

In section 8.1 we have estimated the number of background events in our dataset due to $\beta - \gamma$ events which have their energies above threshold due to the finite detector energy resolution. The other background associated with these events is free neutrons from photo-disintegration of the deuteron by the γ-rays which have energies greater than the deutron binding energy of 2.23 MeV. Sources of such backgrounds will give rise to different spatial distributions of neutrons depending on whether they are internal or external to the D_2O region. γ-rays uniform in the D_2O will lead to uniform distribution of background neutrons which will lead to a capture profile and efficiency that is identical to that for our solar neutrino signal as discussed in chapter 4. γ-rays whose origin is external to the D_2O will lead to neutrons generated near the outer edge of the D_2O region. Detailed Monte-Carlo calculations by Lyon [41] have shown that the ratios of photo-disentegrations to γ-rays in the D_2O are 1/497 and 1/480 for 2.614 and 2.445 MeV γ-rays in the ^{232}Th and ^{238}U chains respectively. Shown in table 8.5 adapted from Lyon [41] are the number of photo-disintegration neutrons generated from uranium and thorium chain contaminations in various detector materials. This table can be used along with the measured contaminations from tables 8.1 and 8.2 to calculate the total number of background neutrons generated in the D_2O.

Chain	^{238}U			^{232}Th		
Location	D_2O	AV	H_2O	D_2O	AV	H_2O
D disintegration rate [/μg/day]	0.256	0.0935	0.00312	0.0341	0.0120	0.000361

Table 8.5: Deuteron photo-disintegration rates due to radioactive contaminations in detector materials.

The capture efficiency and radial profile for a source of neutrons uniform in the D_2O (as is the case for neutrons generated by contamination in the D_2O itself) were studied in detal in chapter 5. To estimate the capture efficiency and radial profile of neutrons generated in the D_2O near the acrylic vessel (as is the case for neutrons generated by contamination external to the D_2O region) a Monte-Carlo calculation was performed with neutrons generated in a shell between radii of 580 and 600 cm. The reconstructed radial profile for this calculation is shown in figure 8.9. The fraction of neutrons generated in this shell which capture and lead to a reconstructed vertex inside of our 540 cm fiducial volume was found to be

$$\epsilon_{shell} = 0.05 \tag{8-9}$$

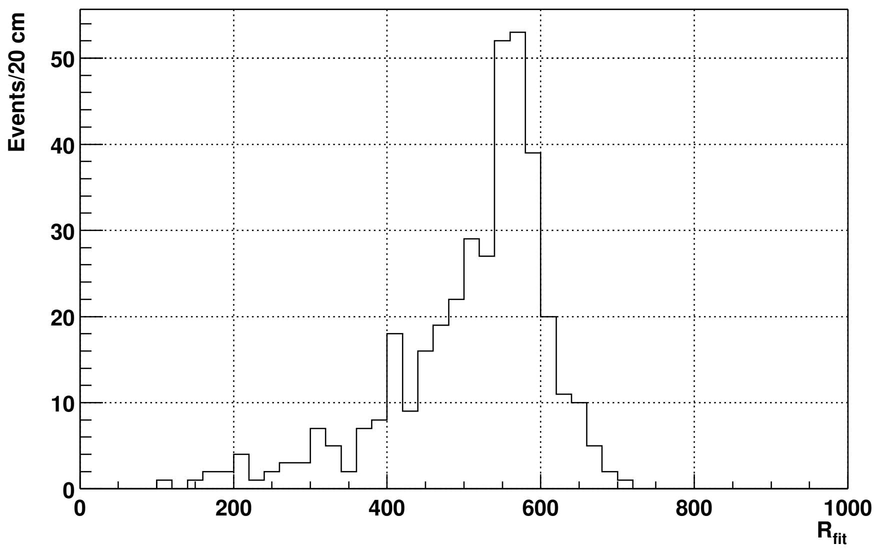

Figure 8.9: Radial distribution of neutron captures for Monte-Carlo calculation with a neutron source near the acrylic vessel

Thus neutrons generated by γ-rays external to the D_2O region lead to less of a background than those generated internally, since those neutrons have a much smaller probability of capturing on ^2H and reconstructing into our fiducial volume. Shown in table 8.6 are the calculated rates of background neutrons released into the D_2O from radioactive contamination in the detector materials. The second row shows these rates weighted by the probability that these events are captured and reconstruct inside a fiducial volume of r = 540 cm. The dominant contribution to the NC background is from radioactive contamination in the D_2O.

	D_2O	AV	H_2O	Phototubes	Total
$N_{neutron}$	1.1 $\pm$ 1.3	$<$ 0.3	0.5 $\pm$0.5	$<$ 0.15	1.4 $\pm$1.1
$N_{neutron} \times \epsilon_{capture}$	0.3	0.015	0.025	0.007	0.35

Table 8.6: Rate of generated background neutrons per day from contaminations in various detector materials. The last row shows the rates with weighting by neutron capture efficiency.

8.4 Atmospheric Neutrinos, Muons and Spallation Products

With the 2039 meter overburden of norite rock, the only particles which can penetrate to this depth and reach the SNO detector are neutrinos and high-energy muons. The background to the solar neutrino flux due to atmospheric neutrinos is on the order of 1 event per kilotonne year per 10 MeV bin [42] and is not significant for the solar neutrino analysis. The rate of muon events in the SNO detector is approximately 3 per hour. Muons themselves are not a significant background to the solar neutrino analysis since the energy deposited in the detector is much greater than that in the solar neutrino region [43]. Muons in the SNO detector can generate spallation products when they interact with the hydrogen and oxygen nuclei in the detector. Figure 8.10 shows the event rates following muon events in the SNO detector, in one second bins. We see that most of the activity is in the first bin; the rates for times greater than one second are consistent with a constant event rate uncorrelated to the muon activity. Figure 8.11 shows the event rates during the first second after muon events. This time distribution is consistent with that for neutron captures on ^{2}H. Figure 8.12 shows the energy spectrum for these events, along with the energy spectrum for neutron capture γ-rays derived from a Monte-Carlo calculation. We thus conclude that most of the muon spallation products in SNO are neutrons. This is a potentially serious background since free neutrons in the heavy water region will lead to a signal that is indistinguishable from the NC neutrino signal. The muon cut efficiency was measured to be $\geq$ 99.5% [44], so that we may fail to identify approximately 1 of every 200 muons in the detector. With rate of approximately 3 muons per hour, this corresponds to approximately 0.36 unidentified muon events per day. The fraction of muons which generate spallation products in SNO was found to be approximately 4% [45], so that the leakage of neutron events into the dataset is less than 0.014 neutrons per day. This is much smaller than the background expected from radioactivity in the detector of approximately 1.3 neutrons/day and will be ignored in the solar neutrino analysis.

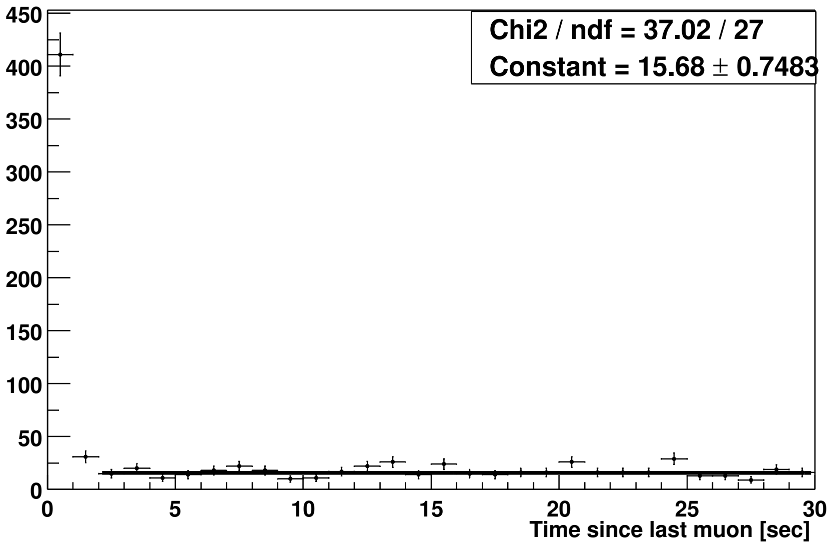

Figure 8.10: Event rates for several seconds following muon events.

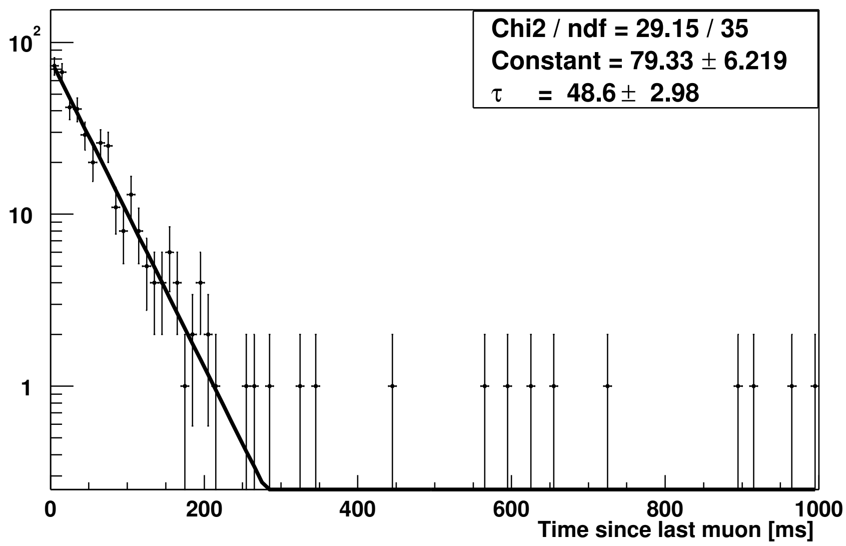

Figure 8.11: Event rates following muon events. The lifetime (τ) of about 50 ms is consistent with the neutron capture time on ^{2}H.

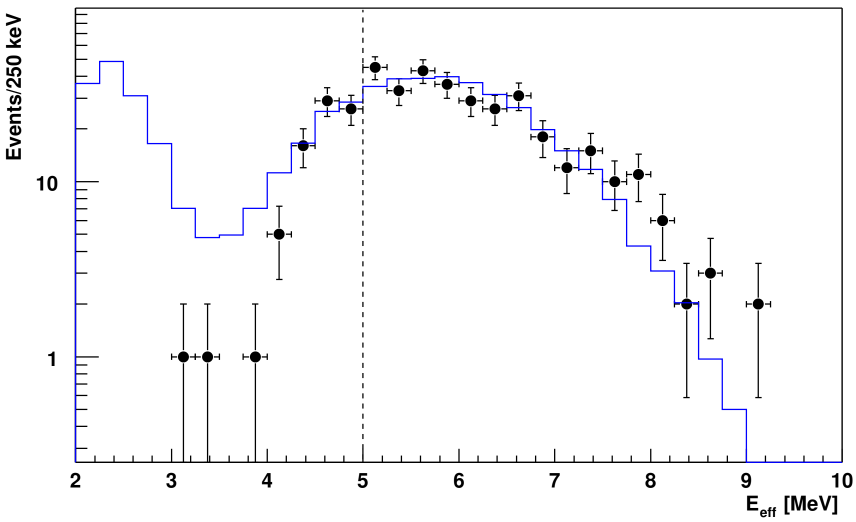

Figure 8.12: Energy spectrum of muon follower events. We see that the energy distribution of events following muons is consistent with that for neutron gamma γ-rays.

Chapter 9

Solar Neutrino Signals in SNO

After the data reduction, event vertex reconstruction and energy calibration have been applied to the data, we are left with a set of events with distributions in E_{eff}, $\vec{x}$, and $\cos\theta_{sun}$. To extract the solar neutrino fluxes from these distributions, we must generate the expected distributions in these measurables as a function of the input spectra and parameters.

The main ingredients used in calculating predicted solar neutrino rates and energy spectra in SNO are the the standard solar model, the neutrino-deuteron and neutrino-electron cross sections, and the response of the SNO detector to the neutrino signals. The standard solar model used here is that of Bahcall and Pinsonneault (BP98) [15]. The neutrino-deuteron cross sections are taken from Kubodera and Nozawa [46]. Ying et al. [47] have also calculated these cross sections. Agreement between the two cross section calculations is about 6%; this agreement is used as an estimate of the absolute cross section uncertainty. The neutrino-electron scattering cross sections used have an uncertainty of about 1%.

9.1 Solar Neutrino Fluxes

Table 9.1 reproduced from [15] shows the predicted solar neutrino fluxes with 1σ uncertainties obtained by combining all uncertainties in input parameters. The ^{8}B and hep neutrinos are the only ones to which SNO is sensitive.

Source	Flux (10^{10} cm^{-2}s^{-1})
pp	$5.94(1.00^{+0.01}_{-0.01})$
pep	$1.39 \times 10^{-2}(1.00^{+0.01}_{-0.01})$
hep	2.10×10^{-7}
^{7}Be	$4.80 \times 10^{-1}(1.00^{+0.09}_{-0.09})$
^{8}B	$5.15 \times 10^{-4}(1.00^{+0.19}_{-0.14})$
^{13}N	$6.05 \times 10^{-2}(1.00^{+0.19}_{-0.13})$
^{15}O	$5.32 \times 10^{-2}(1.00^{+0.22}_{-0.15})$
^{17}F	$6.33 \times 10^{-4}(1.00^{+0.12}_{-0.11})$

Table 9.1: Solar neutrino fluxes predicted with the Standard Solar Model (BP98), including 1σ uncertainties from all sources.

9.2 Neutrino Cross Sections

9.2.1 Neutrino-Deuterium Cross Sections

To use the above solar neutrino fluxes to calculate predicted rates and spectra in the SNO detector, we must know the differential and total cross sections for each of the neutrino reactions possible in SNO. The primary reaction for SNO is charged current absorption on ^{2}H (equation 3-1),

$$\nu_e +^2 \mathrm{H} \longrightarrow p + p + e^-$$

This reaction has the largest cross section and generates electrons with kinetic energies closely related to those of the incident neutrino. It is thus best suited for electron neutrino flux and spectral energy measurements. This reaction also has a weak angular dependence (the distribution of angles between the incoming neutrino and the recoil electron is given approximately by $(1 - 1/3\cos(\theta))$ which can also be used to separate the charged current neutrino signal from other signals and backgrounds in SNO.

Figure 9.1 shows the differential CC cross sections for incoming neutrino energies of 5, 10, and 15 MeV. Figure 9.2 shows the tabulated cross section versus angle between neutrino and recoil electron for a 10 MeV neutrino. Figure 9.3 shows the total CC cross section versus incident neutrino energy for energies in the range of interest to SNO.

SNO is also able to detect neutrinos through neutral current interactions which are independent of flavour (equation 3-2),

$$\nu_x +^2 \mathrm{H} \longrightarrow \nu_x + p + n$$

The subsequent neutron can be detected in SNO to provide a signature for this reaction. SNO can detect neutrons by their capture on ^{2}H which releases a 6.25 MeV γ-ray.

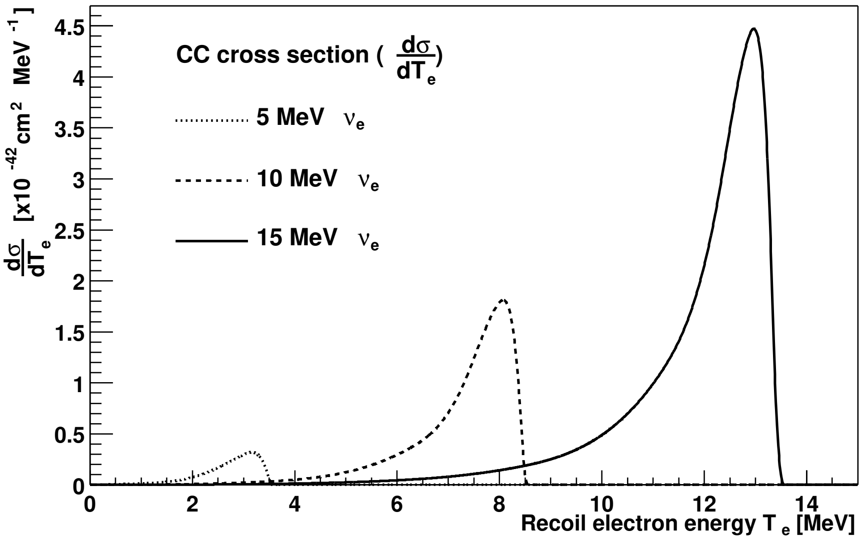

Figure 9.1: Differential CC cross sections for 5, 10, and 15 MeV incident electron neutrinos on ^{2}H. Shown are the cross sections versus electron kinetic energy (denoted T_e). The correlation between incident neutrino energy and recoil electron energy makes this reaction well suited to energy spectrum measurements.

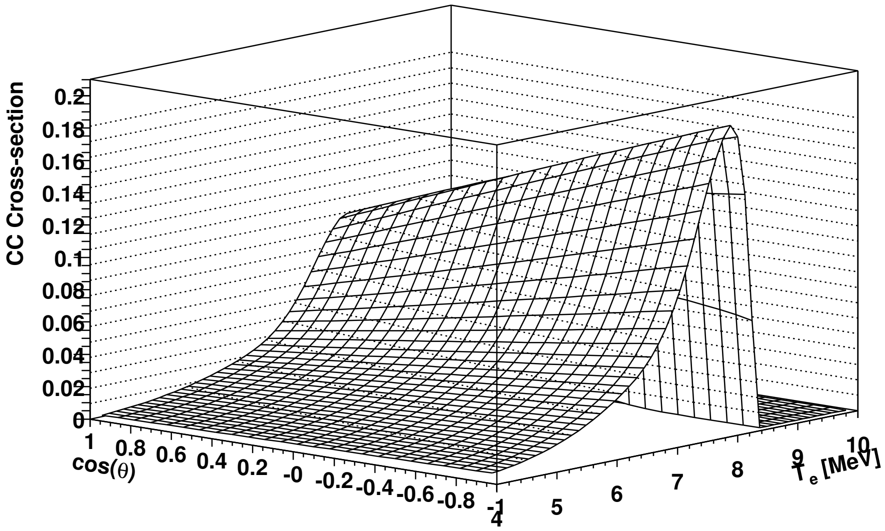

Figure 9.2: CC cross section versus angle between the incident neutrino and recoil electron and electron kinetc energy (denoted T_e) for a 10 MeV neutrino. There is approximately a $(1 - 1/3\cos(\theta))$ angular dependence.

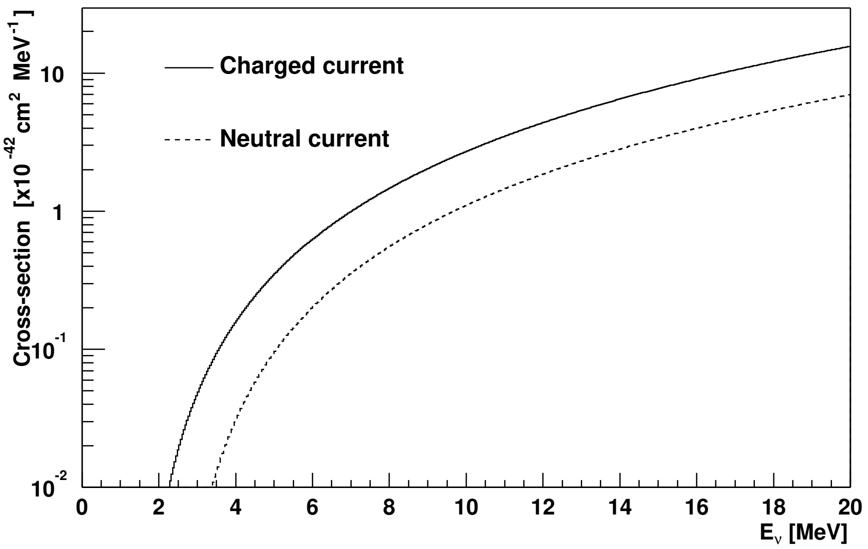

Figure 9.3: Neutrino cross sections versus incident neutrino energy for CC and NC reactions with the deuteron.

9.2.2 Neutrino-Electron Scattering

SNO can also detect neutrinos through neutrino-electron elastic scattering (equation 3-3),

$$\nu_x + e \longrightarrow \nu_x + e$$

Although this reaction can occur for any flavour of incident neutrino, the cross section for electron neutrinos is approximately 7 times that of other flavours. Due to momentum conservation, the recoil electron will have approximately the same direction as the incident neutrino. We can use this angular correlation to separate ES events from other signals and backgrounds in SNO.

The cross section for neutrino-electron scattering is given by [48, 10]

$$\frac{d\sigma}{dT_e} = \frac{\sigma_e}{m_e}[g_L^2 + g_R^2(1 - T_e/q)^2 - g_L g_R(T_e m_e/q^2)] \tag{9-1}$$

where

$$\begin{aligned} T_e & \quad \text{is the electron kinetic energy,} & (9\text{-}2) \\ q & \quad \text{is the neutrino energy,} & (9\text{-}3) \\ g_L &= \pm 1/2 + \sin^2 \Theta_W, & (9\text{-}4) \\ g_R &= \sin^2 \Theta_W, \text{ and} & (9\text{-}5) \\ m_e & \quad \text{is the electron rest mass.} & (9\text{-}6) \end{aligned}$$

The upper sign corresponds to electron neutrino scattering. The lower sign is for other neutrino flavours. The Weinberg mixing angle is given by [49]

$$\sin^2 \Theta_W = 0.231, \tag{9-7}$$

and the dimensional term is [10]

$$\sigma_e = 2G_F^2 m_e^2/\pi\hbar^4 = 88.083 \times 10^{-46}\mathrm{cm}^2 \tag{9-8}$$

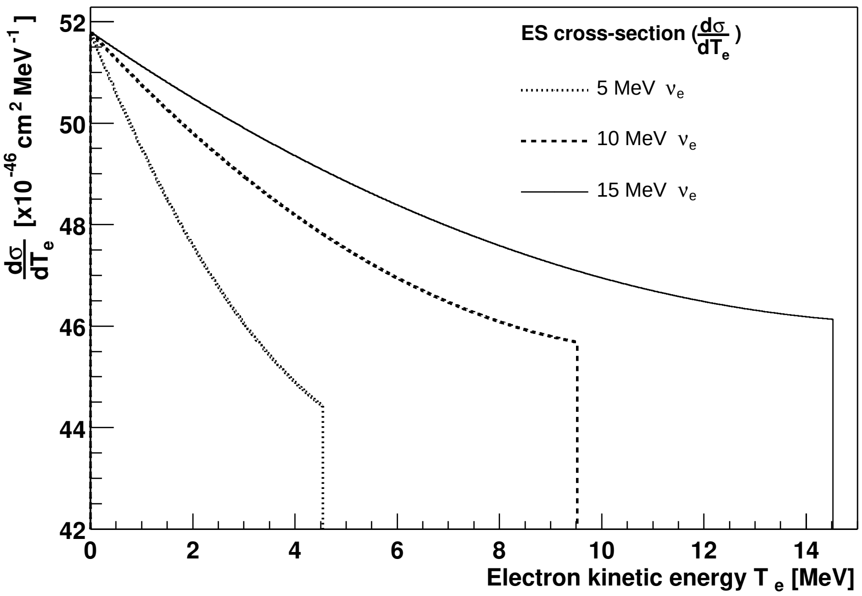

Figure 9.4: Cross sections for $\nu_e - e$ scattering for neutrinos with 5, 10, and 15 MeV energies. Shown are the cross sections versus electron kinetic energy (denoted T$_e$).

9.3 Detection Efficiency

We must also consider detection efficiency to convert the above fluxes and spectra to absolute predicted rates in SNO. This will include vertex reconstruction, data reduction and trigger efficiency. A detection efficiency of 1 is used for electrons and γ-rays. Results of chapter 5 will be used where the capture efficiency on ^{2}H was found to be

$$\epsilon_D = 0.30 \pm 0.03 \tag{9-9}$$

for neutrons generated uniformly in the heavy water, and the appropriate vertex resolution functions will be used.

9.4 Predicted Rates and Spectra

With the above solar neutrino energy spectra and neutrino cross sections, we can calculate the total event rates and recoil electron energy spectra expected in the SNO detector. We can also calculate the expected energy spectrum as measured by SNO by convoluting the recoil electron energy spectrum with SNO's response function

$$\frac{dN}{dE}_{theor}(E) \;\; = \;\; \int_{E_{threshold}}^{\infty} \frac{dN}{dE}(E')\sigma(E')R(E,E')dE', \tag{9-10.a}$$

where

$$\frac{dN}{dE}(E') \quad \text{is the input electron energy spectrum,}$$

$$\sigma(E') \quad \text{is the cross section for the process being measured, and}$$

$$R(E, E') \quad \text{is the detector energy response function shown in figure 6.6.}$$

9.4.1 Charged Current Electron Spectra

For the charged-current interaction, we can convolute the input neutrino spectrum with the differential cross section for charged-current interactions on D_2O,

$$\frac{dN}{dE}_{e^-} = \int_0^\infty \Phi'(E') \frac{d\sigma_{cc}}{dE}(E', E) dE' \tag{9-11}$$

The energy spectrum measured with the SNO detector for these neutrinos is then given by

$$\frac{dN}{dE}_{theor}(E) = \int_{E_{thresh}}^\infty \int_0^\infty \Phi(E_\nu) \frac{d\sigma_{cc}}{dE}(E_\nu, E_{e^-}) R(E, E_{e^-}) dE_\nu dE_{e^-}$$

The calculated rate for the SNO detector is then found by integrating the above expression above the threshold energy.

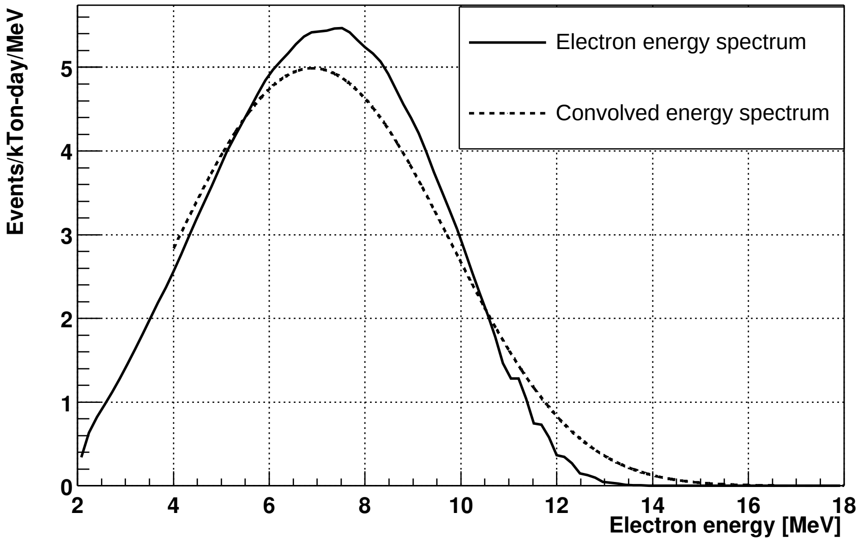

Figure 9.5: Predicted charged current energy spectra from ^{8}B neutrinos. Shown are the recoil total electron energy spectrum, and the predicted energy spectrum after convolution with the detector energy response function. The irregularities in the electron energy spectrum at high energies are a result of the interpolation of the tabulated cross sections.

9.4.2 Elastic Scattering Electron Spectra

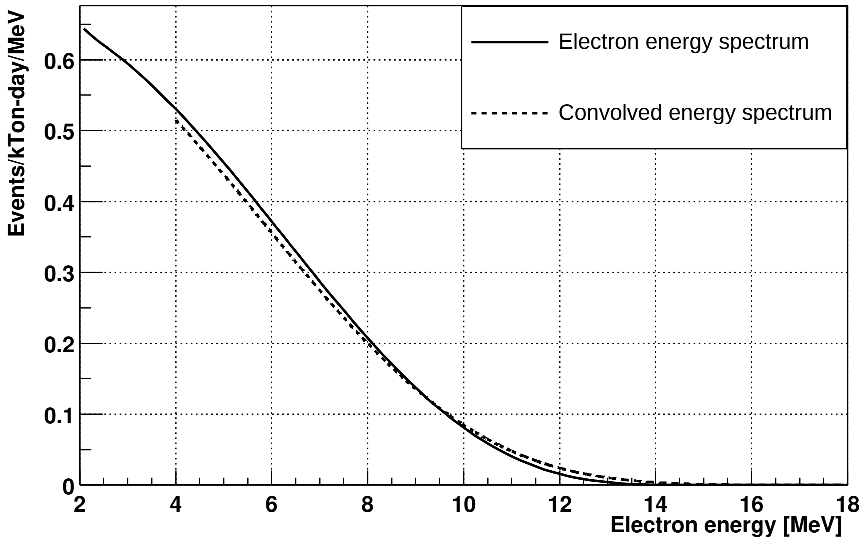

Figure 9.6: Predicted elastic scattering energy spectra from ^{8}B neutrinos. Shown are the recoil electron total energy spectrum, and the predicted energy spectrum after convolution with the detector energy response function.

9.4.3 Neutral Current Events

Neutral current events in SNO will to lead to a free neutron in the heavy water. This neutron can be detected by capture on deuterium with the release of a 6.25 MeV γ-ray. The predicted flux of neutrons due to solar ^{8}B neutrinos is given by

$$R_{NC} = \int_{E_{min,NC}}^{\infty} \frac{dN}{dE_\nu}(E_\nu)\sigma_{NC}(E_\nu)dE_\nu \tag{9-12}$$

where E_{min} is the deuteron binding energy required for neutral current absorption (equation 3-2), 2.23 MeV [49].

With the above cross sections and fluxes, we can calculate the expected neutral current rate in SNO to be

$$R_{NC} = 12.82 \text{ neutrons/kTon-day} \tag{9-13}$$

Figure 9.7 shows the predicted energy spectra from the three available neutrino reactions in SNO with the above detection efficiencies. Figure 9.8 shows the predicted rates in events/kTon-day versus effective energy threshold.

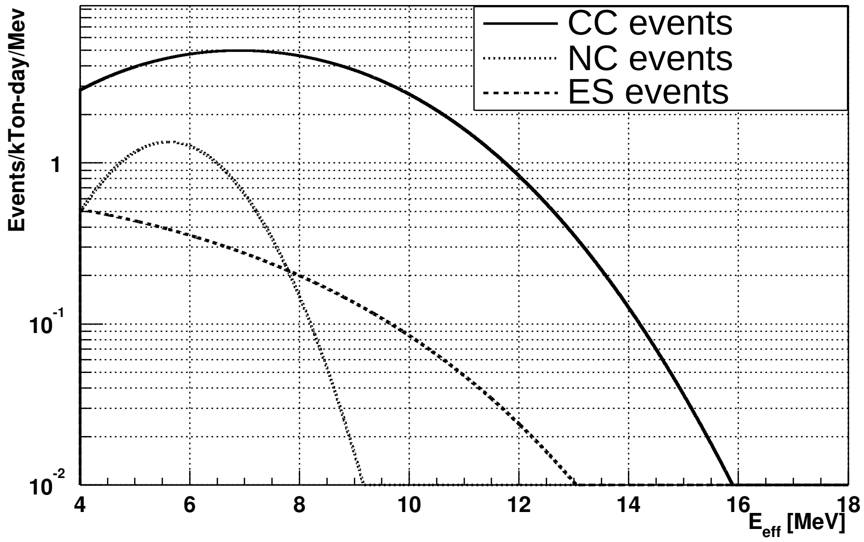

Figure 9.7: Predicted effective neutrino energy spectra.

9.5 Extracting Neutrino Signals

The method used to extract and separate the three solar neutrino signals (CC, ES, and NC) is to define a probability distribution function for each. We define the

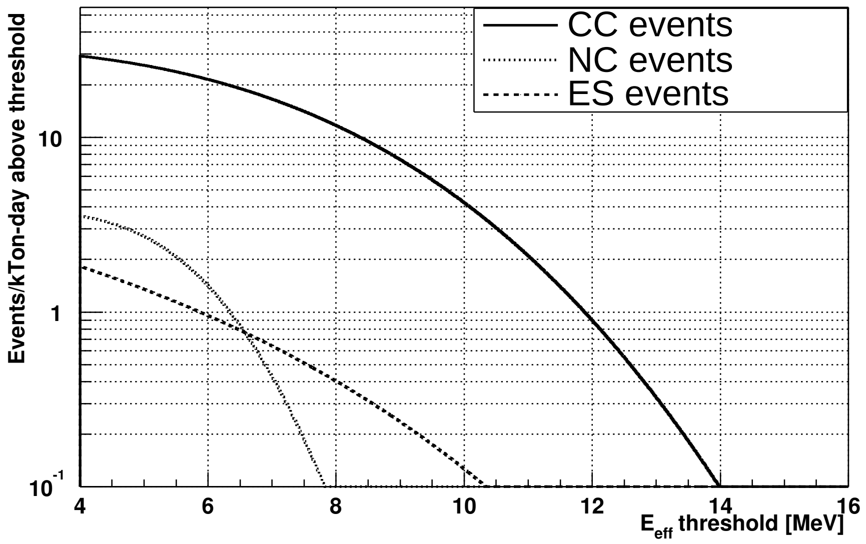

Figure 9.8: Predicted solar neutrino rates in SNO versus effective energy threshold.

probability distribution

$$\mathcal{F}_{signal} = \alpha_{CC} F_{CC} + \alpha_{ES} F_{ES} + \alpha_{NC} F_{NC} \tag{9-14}$$

where the separate signal PDF's F_{CC}, F_{ES} and F_{NC} are functions of the reconstructed radius, effective energy, and direction to the sun and the α_x coefficients are relative fractions of each event type in our data set. In the analysis presented in this thesis we have selected a fiducial volume and energy region such that backgrounds to the solar neutrino signals can be ignored. The analysis can be readily extended by adding background PDF's to equation 9-14.

We can then define the likelihood function

$$\mathcal{L} = \prod_{i=1}^{N} \mathcal{F}_{signal,i} \tag{9-15}$$

where i corresponds to the i'th event in the data set. We can take the logarithm of this function to define the negative log likelihood

$$\mathcal{L} = -2\sum_{i=0}^{N} \log(\mathcal{F}_{signal,i}) \tag{9-16}$$

Equation 9-16 can then be minimized to find the coefficients α_{CC}, α_{ES}, and α_{NC}.

We also have the requirement that the total number of events in our sample is fixed, which allows us to write

$$\alpha_{CC} + \alpha_{ES} + \alpha_{NC} = \text{ constant } \equiv 1. \tag{9-17}$$

We can substitute the above equation in 9-14 and 9-16 so that we now have

$$\mathcal{L} = -2\sum_{i=1}^{N} \log(\alpha_{CC}F_{CC} + \alpha_{ES}F_{ES} + (1 - \alpha_{CC} - \alpha_{ES})F_{NC}) \tag{9-18}$$

Minimizing the above function to find α_{CC} and α_{ES} will give us the number of events in our particular data set of type CC, ES, and NC.

Since we are interested in not only the number of each type of event in our particular data set but the mean number of events in the parent distribution, we modify 9-15 by adding a factor for the probability of obtaining a sample of size N from a Poisson distribution of mean Φ [50]

$$\mathcal{L}_E = \frac{\exp^{-\Phi} \Phi^N}{N!}\mathcal{L} \tag{9-19}$$

where $\mathcal{L}_E$ is the extended likelihood function. We can now write

$$\begin{aligned}\Phi_{CC} &= \Phi\alpha_{CC}\\ \Phi_{ES} &= \Phi\alpha_{ES}\\ \Phi_{NC} &= \Phi(1-\alpha_{ES}-\alpha_{CC}),\end{aligned}$$

so that

$$\Phi = \Phi_{CC} + \Phi_{ES} + \Phi_{NC} \tag{9-20}$$

and equation 9-19 becomes

$$\mathcal{L}_E = \frac{\exp^{-(\Phi_{CC}+\Phi_{ES}+\Phi_{NC})}}{N!}\prod_{i=1}^{N}(\Phi_{CC}F_{CC} + \Phi_{ES}F_{ES} + \Phi_{NC}F_{NC}) \tag{9-21}$$

We again work with the negative logarithm of this expression and redefine $\mathcal{L}_E$ as

$$\mathcal{L}_E = 2\left[\Phi_{CC} + \Phi_{ES} + \Phi_{NC} + \log(N!) - \sum_{i=1}^{N}\log(\Phi_{CC}F_{CC} + \Phi_{ES}F_{ES} + \Phi_{NC}F_{NC})\right] \tag{9-22}$$

Minimizing equation 9-22 for Φ_{CC}, Φ_{ES} and Φ_{NC} will result in the same numbers of events as for equation 9-18; in this case the uncertainties on the fit parameters will include uncertainties due to Poisson fluctuations in the number of events in our sample so that these uncertainties can be used directly when converting from number of events to neutrino fluxes.

The statistical uncertainties in Φ_{CC}, Φ_{ES}, and Φ_{NC} can be approximated by determining the sσ contours in the likelihood surface. We have that for a log likelihood function $(-2\ln L(\vec{\alpha}))$, the sσ confidence intervals are given by the contours with [49]

$$-2\ln L(\vec{\alpha'}) - 2\ln L_{max} = s^2 \tag{9-23}$$

where $\vec{\alpha'}$ is the sσ contour in parameter space and L_{max} is the maximum likelihood. The minimization of equation 9-22 and estimation of statistical uncertainties were implemented with the MINUIT minimization package [51].

9.5.1 The Neutrino Signal Probability Distribution Functions

The following figures show the probability distribution functions used in equation 9-22 to describe the response of the SNO detector to the solar neutrino signals. The analysis techniques described in this work assume an undistorted ^{8}B solar neutrino energy spectrum. The probability distribution functions were derived from the techniques described in chapters 4-6 and have simple analytic forms with tunable parameters. Uncertainties in the shapes of these distributions are discussed and the effects of these uncertainties on the determination of neutrino fluxes are considered in the following sections.

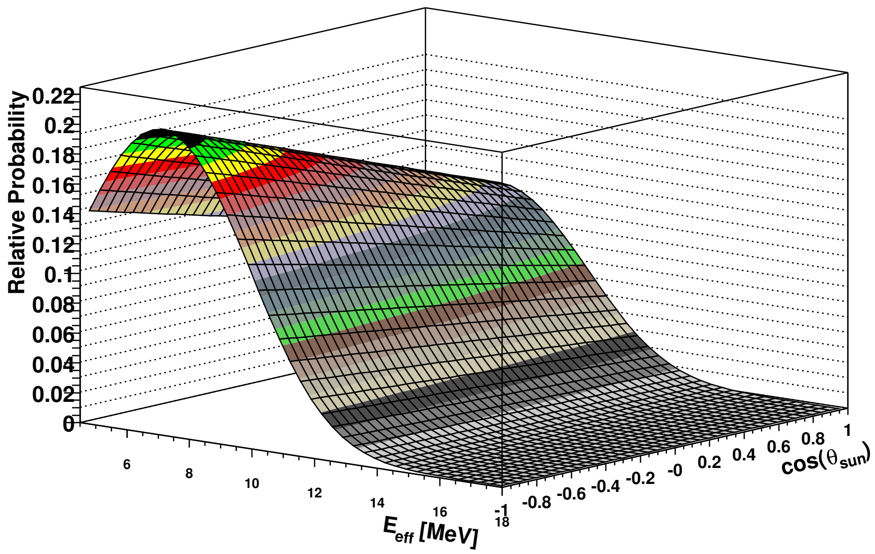

Figure 9.9: Charged current event probability distribution function used for signal separation.

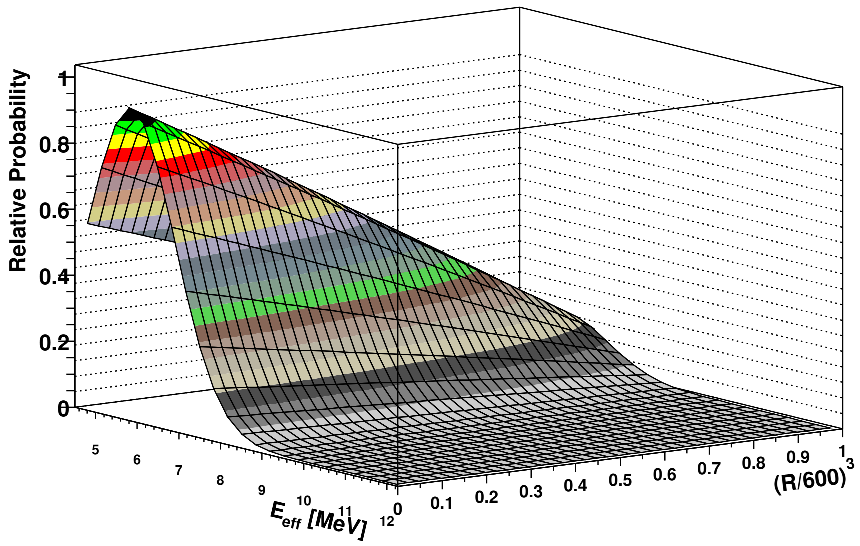

Figure 9.10: Neutral current event probability distribution function used for signal separation.

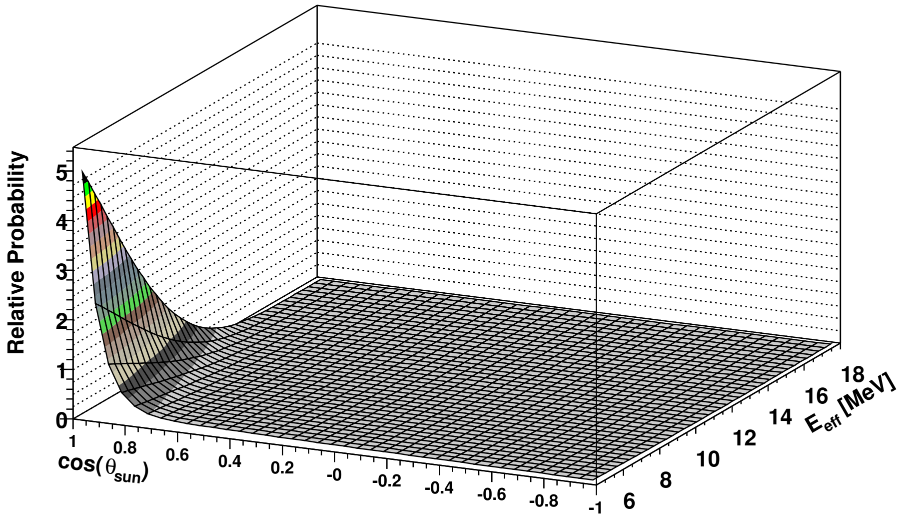

Figure 9.11: Elastic scattering event probability distribution function used for signal separation.

9.5.2 Uncertainties in the Neutrino Signal Probability Distribution Functions

The probability distribution functions used to describe the solar neutrino signals have been built from simple functions which model the response of the detector in vertex, angular, and energy resolution. Detailed studies of these response functions were performed in chapters 4 and 6, and calibration data used to estimate the systematic uncertainty on the response function parameters. To estimate the uncertainty on the solar neutrino signal probability distribution functions, we combine the underlying response function uncertainties.

Effective Energy

We have discussed energy calibration in detail in chapter 6 and assigned an absolute uncertainty to the energy scale and resolution of events in SNO. To assign systematic uncertainties in the derived neutrino fluxes (and flux ratios) we will allow the energy scale and resolution on the three probability distributions to vary by these amounts and study the resultant shifts in the fit fluxes. One has to be careful here, since a shift in the energy scale or resolution will shift both the fit number of events of each type in our data sample, as well as the expected number of events we calculate for given spectral shapes. Since we are interested in the uncertainties in the derived fluxes, we must recalculate these for a given energy and resolution shift.

Reconstructed Radial Profiles

The radial profiles for CC and NC events derived chapter 4 are used for the solar neutrino probability distribution functions, along with the two extreme profiles for the maximum allowed uncertainty in reconstruction resolution.

Angular Resolution

To build the angular component of the solar neutrino probability distribution functions, we use the results for the Monte-Carlo calculations of mono-energetic electrons and the systematic uncertainties derived in chapter 4. A detailed study by Jillings [20] has shown that the dominant contributor to systematic uncertainty involved with angular resolution is that due to multiple scattering. A correction was applied to match the relative area under the multiple scattering component of the angular resolution function to the relative area derived from the Monte-Carlo calculations

$$\alpha_M \longrightarrow \alpha_M \times (1 + 20\%) \tag{9-24}$$

This small correction is used since for values of $\cos\theta_e$ far from the main peak the angular resolution deviates from the form of equation 4-35. Figure 9.12 shows the average angular resolution for elastic scattering events generated from a Monte-Carlo calculation, along with the extreme cases of 5 and 15 MeV electrons, where we can clearly see that uncertainty in the fraction of the signal contained in the tail will lead to an uncertainty in the total area.

9.5.3 Sample Monte-Carlo Data Sets

We have used the Monte-Carlo method to generate a large number of sample data sets closely resembling our data set. This has several purposes. The fitting algorithms can be developed and tested on the Monte-Carlo data sets. We can also apply the fit to a large number of Monte-Carlo data sets and assure ourselves that the statistical

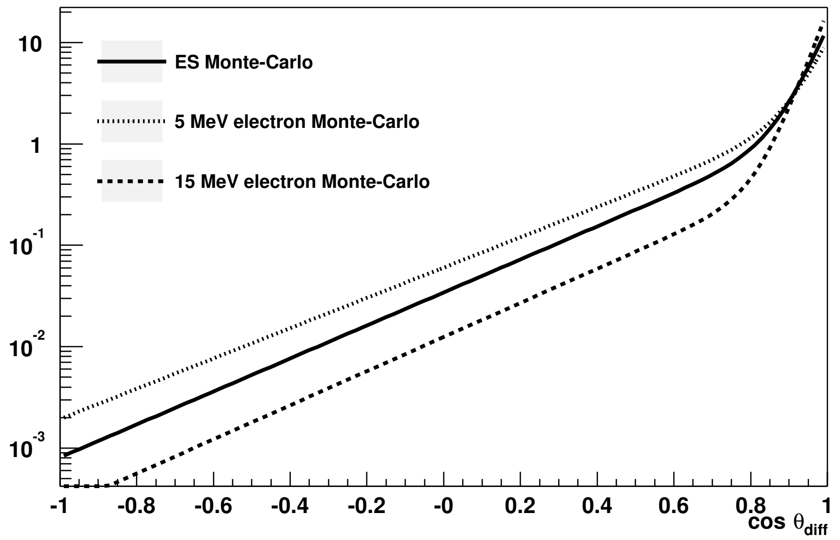

Figure 9.12: Angular resolution derived from SNOMAN Monte-Carlo calculations. Shown are the average angular resolution for elastic scattering events and the extreme cases of 5 and 15 MeV electrons used for studies of systematic uncertainties.

uncertainties estimated by equation 9-23 are correct. The Monte-Carlo method can (and will) be used to estimate the systematic uncertainties involved with uncertainties in the input probability distributions.

We can also use the distribution of likelihoods (from equation 9-22) at the fit minima for a large number of Monte-Carlo data sets where the input parameters (number of each type of event) is taken from the fit to our data as a measure of the goodness of fit for our particular data. This is especially useful since we have a priori no distribution to which we can compare our likelihood as one would have with a χ^2 minimization. The significance level for a given likelihood distribution $P(\mathcal{L})$ is defined as

$$SL(\mathcal{L}) = \frac{1}{\int_{-\infty}^{\infty} P(\mathcal{L}')d\mathcal{L}'} \int_{\mathcal{L}}^{\infty} P(\mathcal{L}')d\mathcal{L}' \tag{9-25}$$

We have thus performed 100 independent Monte-Carlo calculations, each with a different random number seed so that the generated events are statistically independent. The numbers of each type of event was chosen to be near our results discussed in the following chapter, and are shown in table 9.2.

We have minimized equation 9-22 for each of these data sets. The distribution of fit results are shown in figures 9.13-9.15. Also shown are the true number of events from table 9.2 and the average 1σ confidence intervals as calculated with equation 9-23 for $s = 1$. We can see that the fitting algorithms do converge to the true number of events and that the 1σ confidence intervals are correct. This is a powerful result since we have shown that the simple analytic parameterization of the detector response to solar neutrinos can be used effectively to extract the solar neutrino signals from complex Monte-Carlo calculations. The many small details and irregularities present in the Monte-Carlo calculation thus have little effect on the output signal and we are justified in representing the detector response with analytic probability distribution functions. Table 9.3 shows the mean number of fit events of each type derived by fitting a Gaussian function to the distributions of figures 9.13-9.15, the width of the Gaussian function, and the mean 1σ confidence interval from the fit.

The distribution of likelihoods and the integral likelihood distribution are shown in figure 9.16. These will be used in estimating the goodness of fit to our data in the following chapter.

CC	ES	NC
771	89	252

Table 9.2: Number of events used in each of the 100 Monte-Carlo calculations.

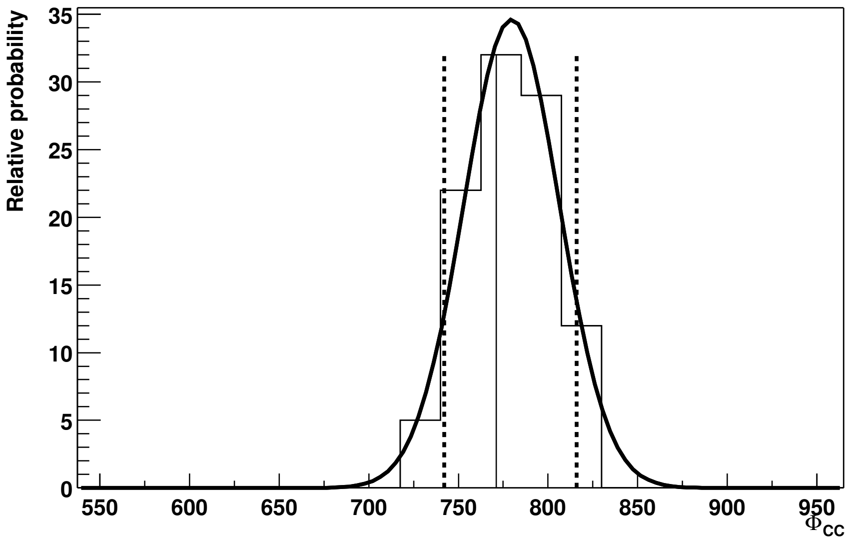

Figure 9.13: Distribution of fit CC events (Φ_{CC}) for 100 Monte-Carlo data sets (histogram). Also shown are the Gaussian fit to this histogram and the average 1σ confidence intervals calculated with equation 9-23.

	CC	ES	NC
$\bar{\Phi}_x$	780 ± 3	86 ± 1	247 ± 3
σ_{gaus}	27	9	25
σ_{fit}	37	14	29

Table 9.3: Average fit results for the 100 Monte-Carlo data sets. We find good agreement with the true values of table 9.2. We can also see that σ_{fit} is larger than σ_{gaus} as expected, since it includes uncertainty due to Poisson fluctuations in the expected number of events.

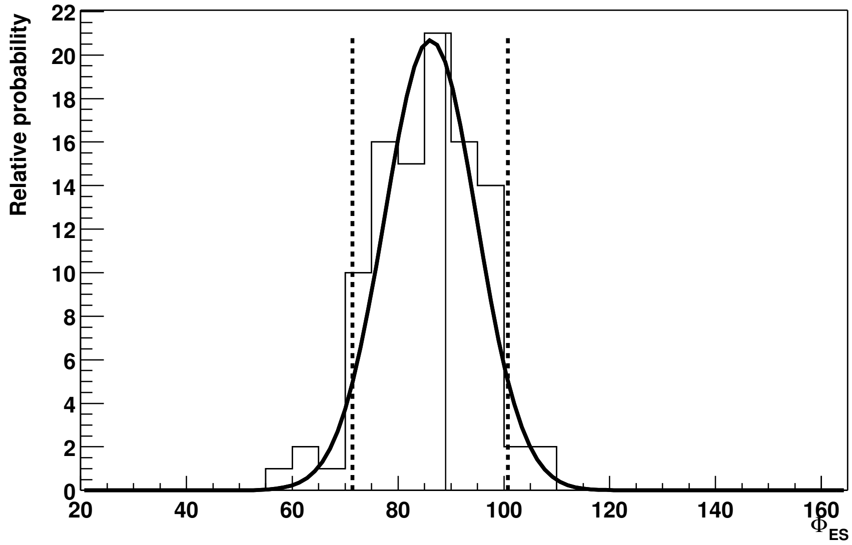

Figure 9.14: Distribution of fit ES events (Φ_{ES}) for 100 Monte-Carlo data sets (histogram). Also shown are the Gaussian fit to this histogram and the average 1σ confidence intervals calculated with equation 9-23.

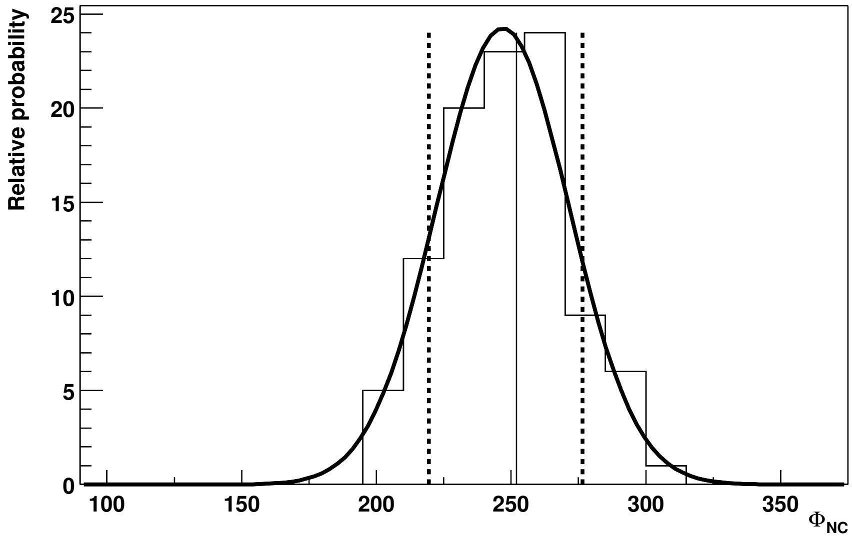

Figure 9.15: Distribution of fit NC events (Φ_{NC}) for 100 Monte-Carlo data sets (histogram). Also shown are the Gaussian fit to this histogram and the average 1σ confidence intervals calculated with equation 9-23.

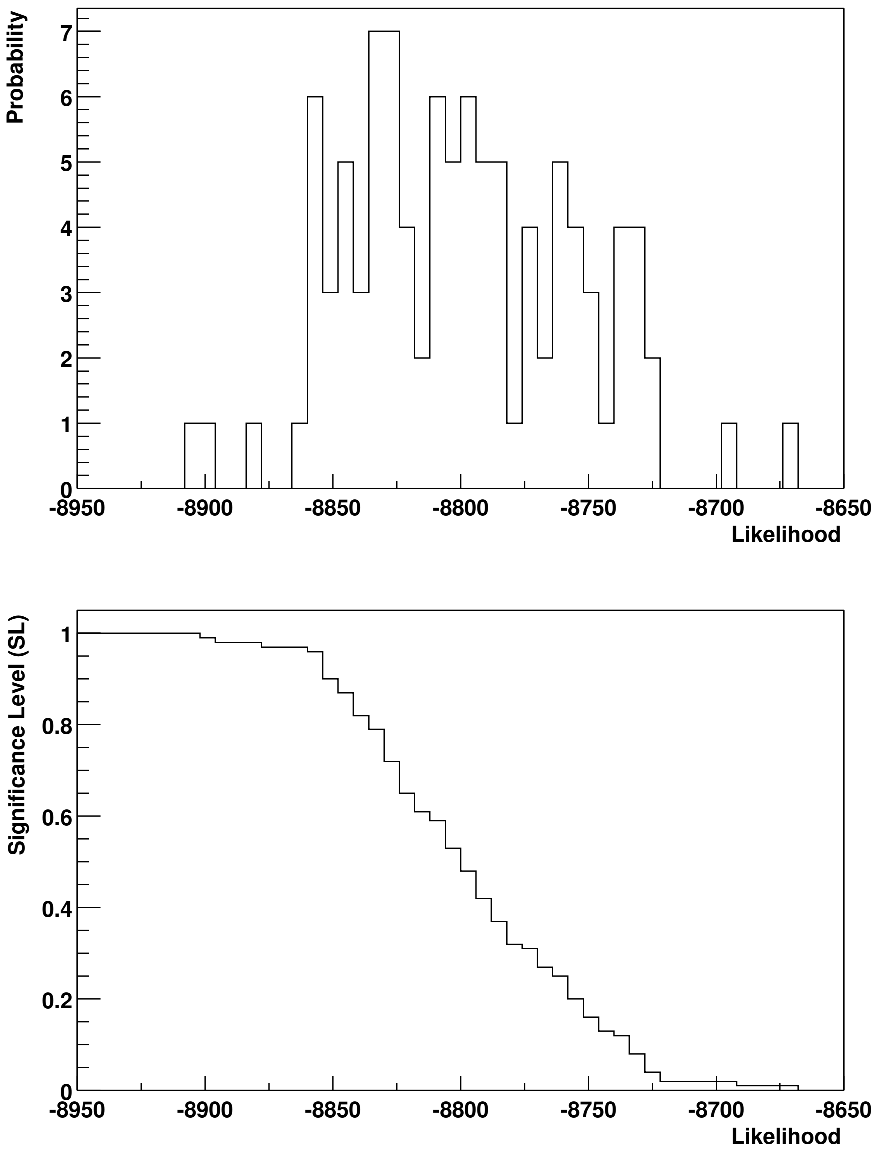

Figure 9.16: Likelihood distribution from 100 Monte-Carlo data sets. The top frame show the relative probability for a given likelihood. The bottom frame shows the significance level for a given likelihood defined by equation 9-25.

9.5.4 Systematic Uncertainties on Fit Results

To estimate the effect that systematic uncertainties in the signal probability distribution functions have on the extracted results, we will repeat the minimization of equation 9-22 with the probability distributions modified within their allowed limits. Since our complete detector response to neutrino signals has been expressed in terms of a small number of parameters, we can easily vary all of these parameters in turn and estimate the systematic uncertainty in the fit results. Thus the uncertainty in a given fit result due to an uncertainty in a response parameter is given by

$$\sigma_R^C = \frac{\Phi_R - \Phi_{R,C}}{\Phi_R} \tag{9-26}$$

where R denotes the event class (CC, ES, or NC) and C denotes the cause of the systematic uncertainty (energy, angular resolution, or radial profile). Φ_R denotes the fit result, and $\Phi_{R,C}$ the fit result with modified input probability distribution function. As an example, figure 9.17 shows the derived systematic uncertainty in Φ_{CC} due a 2% uncertainty in the absolute energy calibration, for the 100 Monte-Carlo data sets.

The systematic uncertainties due to all of the response parameters were estimated for these data sets using equation 9-26. Tables 9.4- 9.5 show the derived uncertainties in the number of fit events, the solar neutrino fluxes, and flux ratios. We find that the solar neutrino fluxes have a total systematic uncertainty of approximately 10%. The [CC]/[NC] ratio has a somewhat larger uncertainty of about 15% due mostly to anti-correlation of the fit number of CC and NC events with energy scale variation. The [CC]/[ES] ratio has a relatively small systematic uncertainty of about 5%.

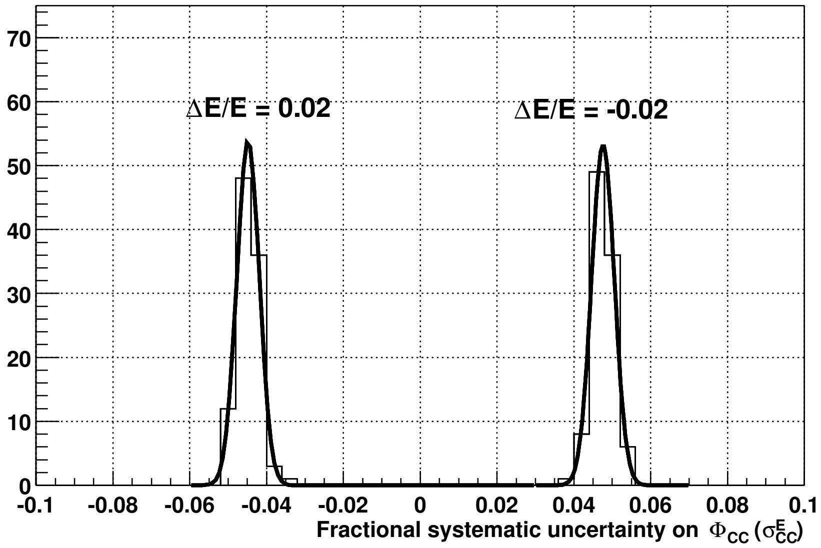

Figure 9.17: Systematic uncertainty of Φ_{CC} due to energy scale uncertainty. The fractional uncertainty is defined by equation 9-26.

	σ_{CC}	σ_{ES}	σ_{NC}
σ^E	$^{+0.05}_{-0.04}$	$^{+0.01}_{-0.01}$	$^{+0.14}_{-0.15}$
σ^{AR}	$^{+0.01}_{-0.01}$	$^{+0.21}_{-0.17}$	$^{+0.02}_{-0.02}$
σ^R	$^{+0.003}_{0.006}$	$^{+0.002}_{-0.004}$	$^{+0.02}_{-0.006}$

Table 9.4: Systematic uncertainties on numbers of events for MC data sets. We have combined the uncertainties due to energy calibration (σ^E), angular resolution (σ^{AR}), and vertex reconstruction (σ^R).

	[CC]	[ES]	[NC]	[CC]/[NC]	[CC]/[ES]
σ^E	$^{+0.05}_{-0.04}$	$^{+0.01}_{-0.01}$	$^{+0.03}_{-0.03}$	$^{+0.08}_{-0.08}$	$^{+0.04}_{-0.03}$
σ^{AR}	$^{+0.01}_{-0.01}$	$^{+0.21}_{-0.17}$	$^{+0.02}_{-0.02}$	$^{+0.008}_{-0.006}$	$^{+0.15}_{-0.29}$
σ^R	$^{+0.003}_{-0.006}$	$^{+0.002}_{-0.004}$	$^{+0.08}_{-0.06}$	$^{+0.06}_{-0.09}$	$^{+0.0005}_{-0.001}$

Table 9.5: Systematic uncertainties on derived fluxes for MC data sets.

Chapter 10

Analysis of SNO Data

10.1 SNO Data Set

SNO was filled with heavy water and began taking data in May of 1999. The first several months served as a commissioning phase; the detector operating parameters were frozen in November 1999 when production data taking began. After analyzing the results of the water radioactivity assays shown in chapter 8, data taken between December 1999 and June 2000 were used in this analysis since the background levels were near or below target. Good neutrino runs were selected by removing any runs where hardware problems existed or when the detector was being calibrated. Figure 10.1 shows the fractional livetime versus date for the selected runs. The total neutrino livetime for the data set analyzed in this thesis was approximately 141.7 days before data reduction, which corresponds to a live fraction of about 67%; the neutrino livetime after data reduction was 139.4 live days.

The average trigger rate of the SNO detector during this time period was 16.6 Hz, most of which is due to the very low energy background. The total number of

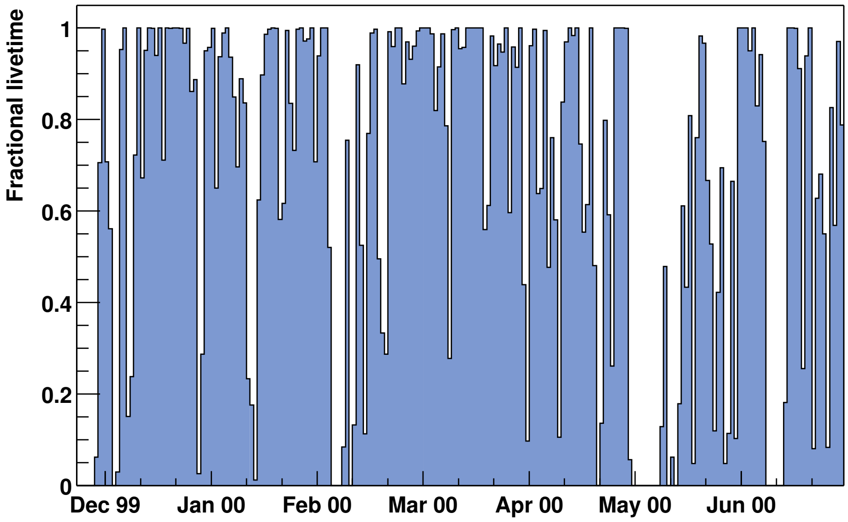

Figure 10.1: Livetime histogram for the production data set used in this analysis. A total of 141.7 days of data were used (before data cleaning), corresponding to a live fraction of about 67%.

triggered events for the runs used was 202,795,542.

The raw NHITs spectrum for the selected runs is shown in figure 10.2. An analysis threshold of 30 NHITs was applied to the data since this greatly reduced the size of the data set while still allowing for a relatively low energy threshold to be applied. Table 10.1 outlines the fraction of events removed for each of the data reduction steps. The 30 NHITs cut decreased the number of events in the data set to about 0.5% of the total. The first pass data reduction described in chapter 7 further reduced the number of events by about a factor of 5. Restricting ourselves to the region between 50 and 120 NHITs, roughly equivalent to our final energy region of interest of 6 to 16 MeV, further reduced the data set by a factor of about 40. After application of the final fiducial volume and energy cuts, we have 968 events selected for analysis, equivalent to a rate of approximately 7.1 events/day.

Figure 10.3 shows the NHITs spectra after each set of first-pass cuts is applied. We see that a large fraction of the data are removed by the flasher cuts. Shown in figure 10.4 are the NHITs spectra for various fiducial volume cuts. The final spectrum for $R_{fit} < 540$ cm is for the events used to extract the solar neutrino signals.

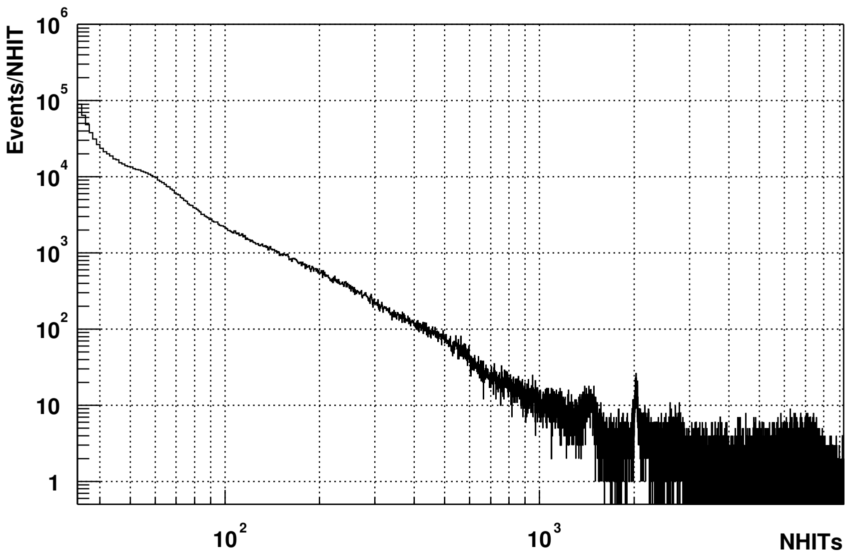

Figure 10.2: Raw NHITs spectrum for the data set analyzed, before any data reduction or fitted vertex cuts. An analysis threshold of 30 Nhits was applied.

Data reduction step	No. events	Average rate
Raw data	202 795 542	16.6 Hz
NHITs >= 30	980 978	4.8 min^{-1}
Pass 1 reduction	190 978	0.94 min^{-1}
$50 \leq$ NHITs ≤ 120	5439	38.7 day^{-1}
$R_{fit} <= 800$ cm	3902	27.8 day^{-1}
$R_{fit} <= 700$ cm	2457	24.6 day^{-1}
$R_{fit} <= 600$ cm	1617	11.5 day^{-1}
$R_{fit} <= 540$ cm	1161	8.3 day^{-1}
$6 < E_{eff} < 16$ MeV	968	7.1 day^{-1}

Table 10.1: Events remaining after various data reduction steps.

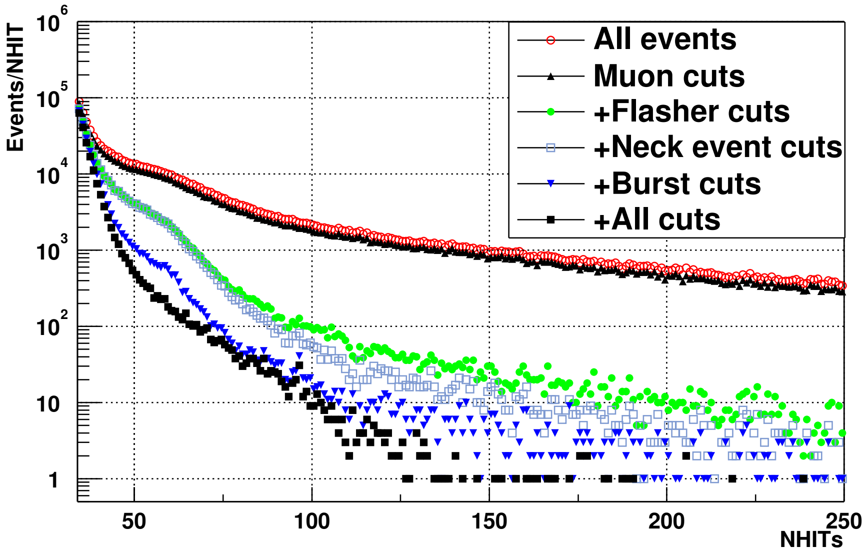

Figure 10.3: NHITs spectra for first pass data reduction steps.

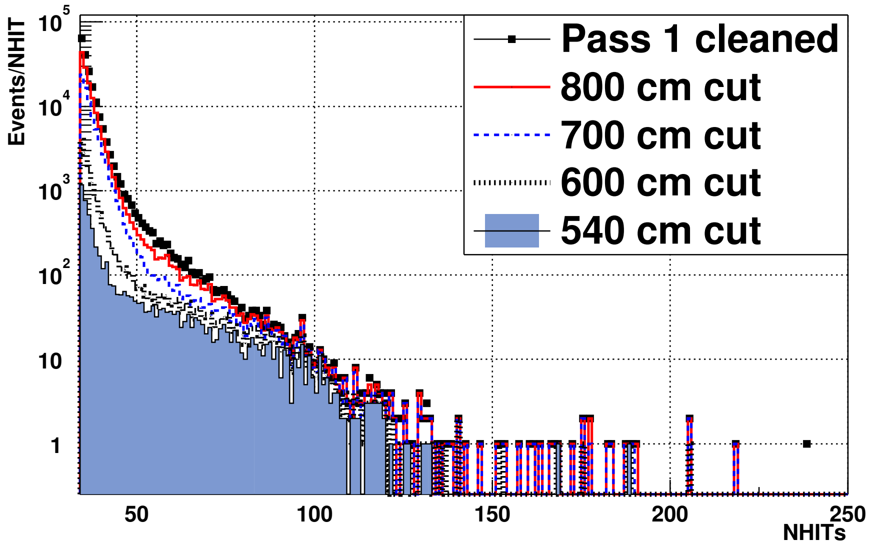

Figure 10.4: NHITs spectra for various fiducial volume cuts applied to the data set.

Shown in figure 10.5 are the number of events in the data set for calibrated energy versus volume weighted radius ($(R_{fit}/600)^3$). The box shows the 968 events selected for analysis with $6 < E_{eff} < 16$ MeV and $R_{fit} < 540$ cm. This region was selected to provide a solar neutrino signal with a negligeable contribution from background radioactivity as discussed in chapter 8. A class of events which reconstruct near the D_2O boundary are associated with the acrylic vessel and are removed by the radial cut. Figure 10.6 shows the raw event rate for all events with NHITs > 30 from the selected runs, and figure 10.7 shows the rate for the selected events. We note that this rate is approximately constant at 7.1 events/day throughout the 6 month period. The data are shown projected onto the three dimensions used in the maximum likelihood fit, namely calibrated energy, radial profile, and $\cos\theta_{sun}$. These distributions are shown in figures 10.8-10.10.

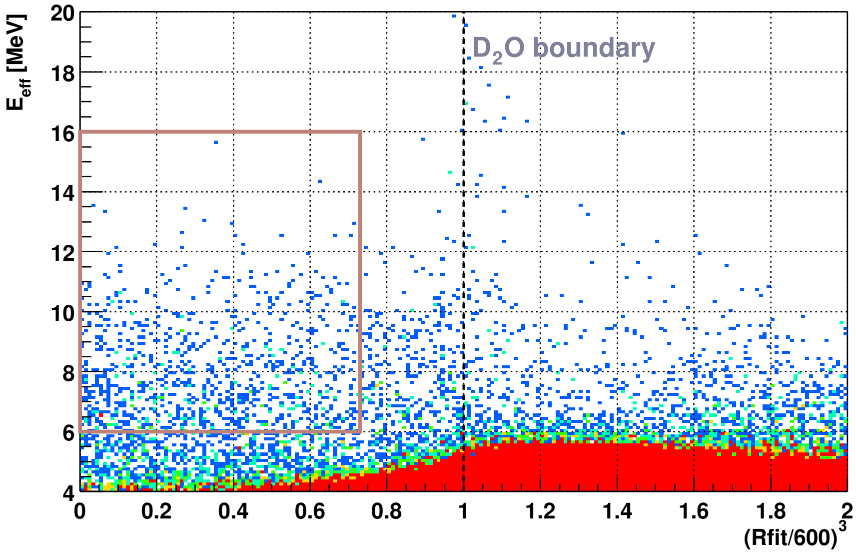

Figure 10.5: Events selected for analysis. The analysis described in chapter 9 was applied to the selected events.

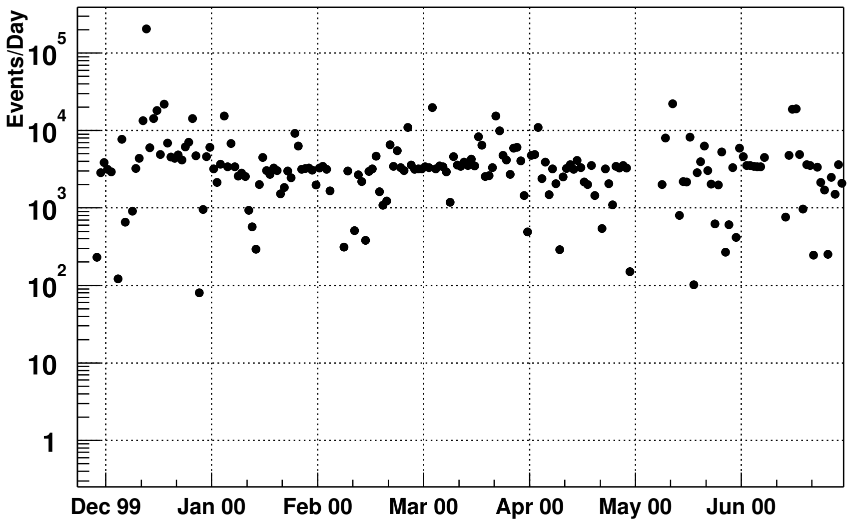

Figure 10.6: Raw event rates for the runs analyzed. A software threshold of 30 NHITs was applied.

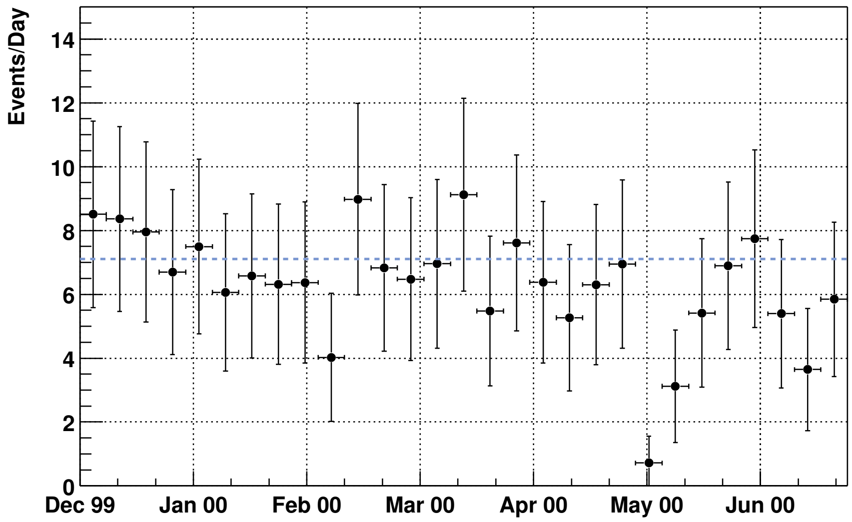

Figure 10.7: Livetime corrected event rates for the 968 events selected for analysis. The dashed line shows the average event rate of 7.1 per day.

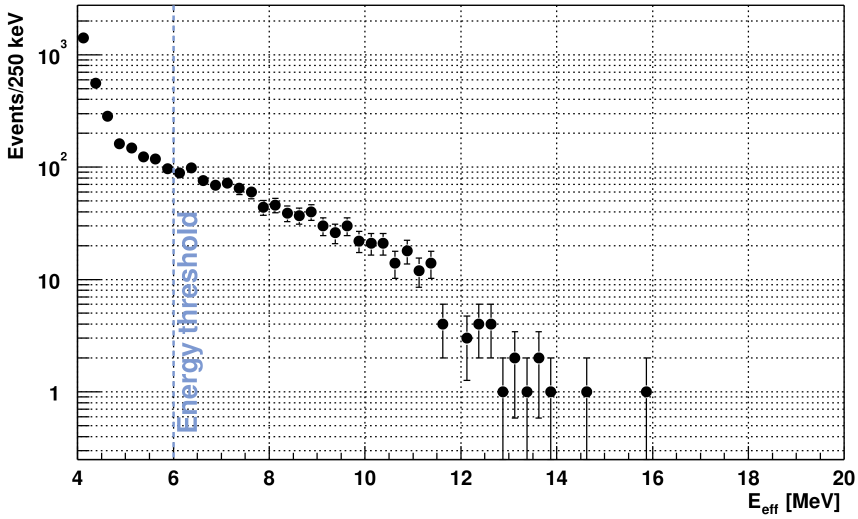

Figure 10.8: Energy spectrum for the selected data. E_{eff} is defined as total electron energy.

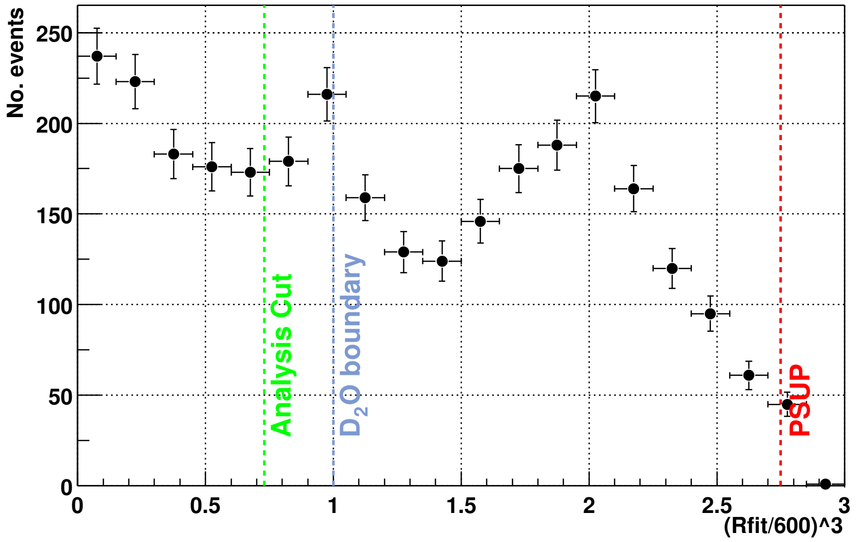

Figure 10.9: Radial distribution for the selected data.

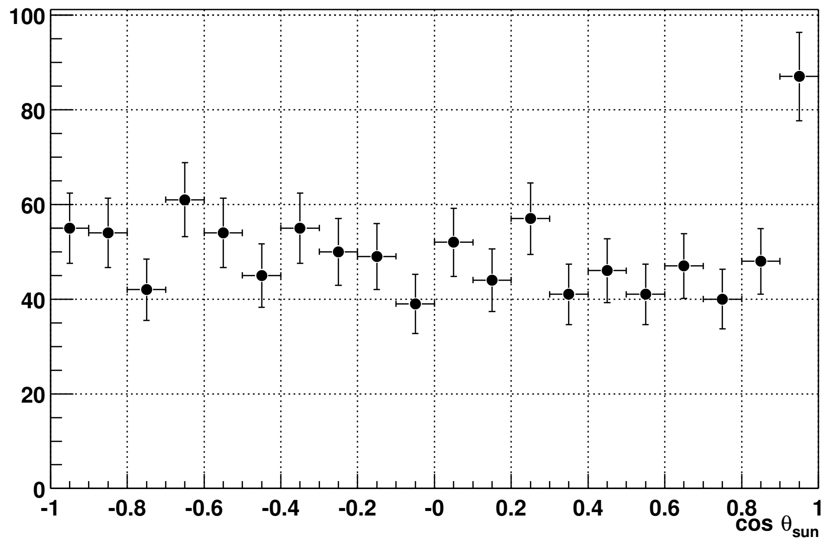

Figure 10.10: $\cos\theta_{sun}$ distribution for the selected data.

10.2 Results

10.2.1 Maximum Likelihood Fit

The selected events were analyzed as described in chapter 9. For the 968 events, E_{eff}, R_{fit}, and $\cos\theta_{sun}$ were determined. This set of events was then used with equation 9-22 to determine the most likely number of CC, ES, and NC events in the data set. The detailed analysis procedure and a description of the object-oriented analysis code is described by Boulay [52]. The resulting fit parameters are shown in table 10.2. The tabulated model values are the expected numbers of events for the standard solar model, the livetime of the data set analyzed, and our selected fiducial volume and energy region. The fit value for the neutral current signal includes the contribution from the neutral current background. Shown in figures 10.11- 10.14 are the radial, $\cos\theta_{sun}$ and energy distributions for the selected data, as well as the shapes predicted by the model, normalized to the fit values. The radial profiles are shown for two energy regions: figure 10.11 is for $6 < E_{eff} < 8$ MeV, where the neutral current contribution is emphasized, and figure 10.12 is for $E_{eff} > 8$ MeV, where there is very little contribution from the neutral current signal.

	Fit results	Model values
N_{cc}	$664.14^{+34.72}_{-33.76}$	2118.23
N_{es}	$78.47^{+14.04}_{-13.25}$	189.81
N_{nc}	$225.47^{+26.87}_{-26.28}$	159.72(SSM) + 16.32(bkg)

Table 10.2: Results of maximum likelihood fit.

We find that the shapes of the energy, radial, and angular distributions agree well with the predicted shapes.

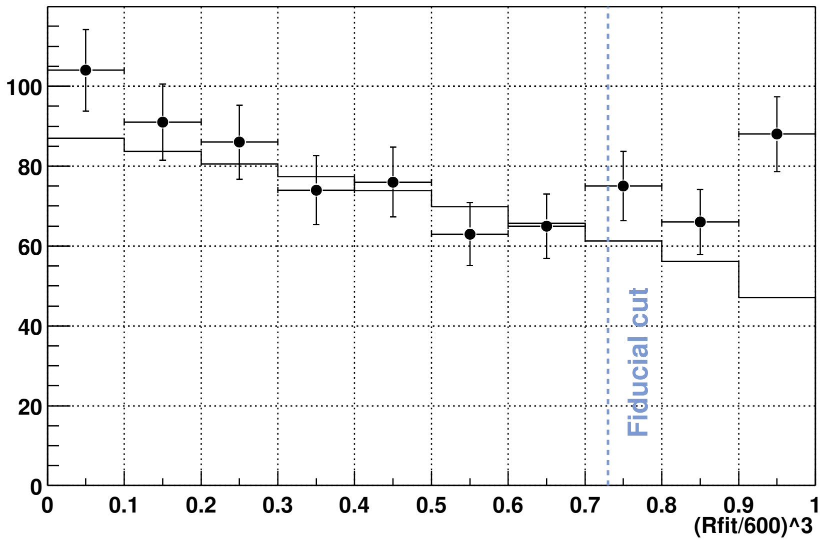

Figure 10.11: Radial profile of events selected for analysis with effective energy between 6 and 8 MeV (data points) and the expected radial profile scaled to the fit results (line). The χ^2 between the data and model is 6.6 for 8 d.o.f.

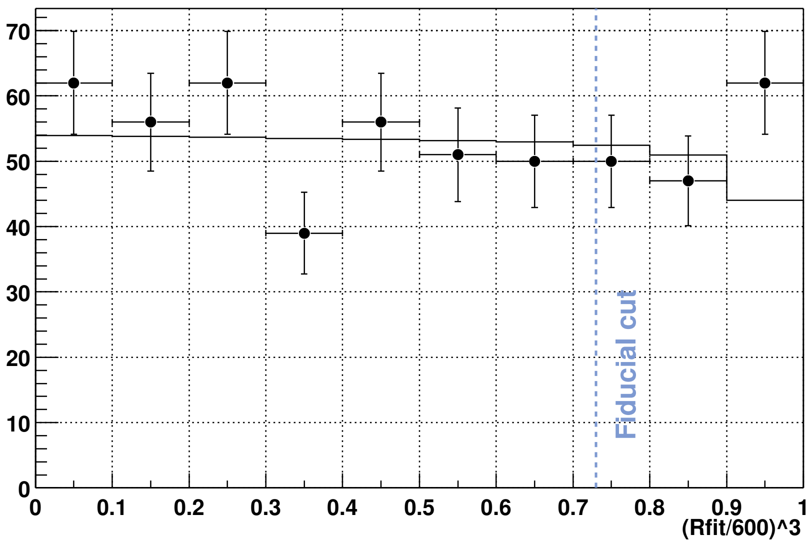

Figure 10.12: Radial profile of events selected for analysis with effective energy greater than 8 MeV (data points) and the expected profile scaled to fit results (line). The χ^2 between the data and model is 8.4 for 8 d.o.f.

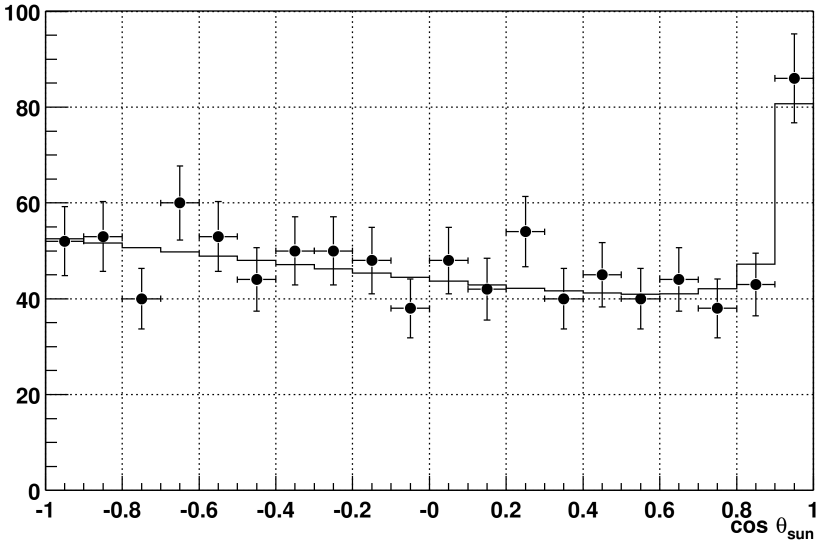

Figure 10.13: $\cos\theta_{sun}$ distribution for events selected for analysis (data points) and the expected distribution scaled to the fit results (line). The χ^2 between the data and model is 12 for 8 d.o.f.

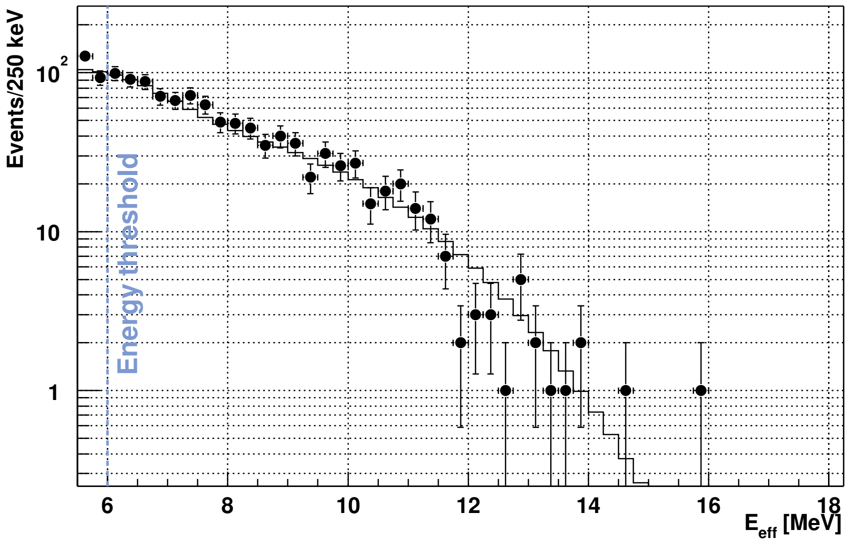

Figure 10.14: Energy spectrum for events selected for analysis (points) and the expected distribution scaled to the fit results (line). The χ^2 between the data and model is 45 for 41 d.o.f.

10.2.2 Uncertainties on Fit Results

The systematic uncertainties on the fit results presented in table 10.2 were calculated by using equation 9-26. Tabulated are the systematic uncertainties due to energy scale and resolution uncertainties (E_0, σ_E), radial profile (R^3), and angular resolution ($\alpha_M, \beta_M, \beta_S$). Also shown are the uncertainties due to uncertainty in the fiducial volume selected for analysis due an absolute radial uncertainty of 10 cm, and uncertainties due to neutron capture efficiency uncertainty. Tables 10.3- 10.5 show the derived systematic uncertainties for fit number of events, fluxes, and flux ratios. The bottom row shows the sum of all systematic uncertainties in quadrature. We can combine tables 10.2- 10.5 to derive the measured solar neutrino fluxes and flux ratios for each of the three reactions.

Variable	N_{CC}	N_{ES}	N_{NC}
E_0	$^{+0.051}_{-0.048}$	$^{+0.015}_{-0.012}$	$^{+0.146}_{-0.160}$
σ_E	$^{+0.012}_{-0.013}$	$^{+0.007}_{-0.006}$	$^{+0.041}_{-0.039}$
R^3	$^{+0.000}_{-0.000}$	$^{+0.001}_{-0.001}$	$^{+0.000}_{-0.001}$
α_M	$^{+0.003}_{-0.003}$	$^{+0.033}_{-0.032}$	$^{+0.004}_{-0.004}$
β_M	$^{+0.001}_{-0.001}$	$^{+0.013}_{-0.011}$	$^{+0.002}_{-0.001}$
β_S	$^{+0.002}_{-0.002}$	$^{+0.019}_{-0.020}$	$^{+0.002}_{-0.001}$
Volume	$^{+0.000}_{-0.000}$	$^{+0.000}_{-0.000}$	$^{+0.000}_{-0.000}$
n capture	$^{+0.000}_{-0.000}$	$^{+0.000}_{-0.000}$	$^{+0.000}_{-0.000}$
Total	$^{+0.053}_{-0.050}$	$^{+0.044}_{-0.042}$	$^{+0.152}_{-0.164}$

Table 10.3: Systematic uncertainties on fit numbers of events.

The fit values for the solar neutrino fluxes for the 6 MeV threshold are found to

Variable	Φ_{CC}	Φ_{ES}	Φ_{NC}
E_0	$^{+0.076}_{-0.076}$	$^{+0.057}_{-0.056}$	$^{+0.023}_{-0.042}$
σ_E	$^{+0.015}_{-0.016}$	$^{+0.007}_{-0.006}$	$^{+0.020}_{-0.019}$
R^3	$^{+0.000}_{-0.000}$	$^{+0.001}_{-0.001}$	$^{+0.000}_{-0.001}$
α_M	$^{+0.003}_{-0.003}$	$^{+0.033}_{-0.032}$	$^{+0.004}_{-0.004}$
β_M	$^{+0.001}_{-0.001}$	$^{+0.013}_{-0.011}$	$^{+0.002}_{-0.001}$
β_S	$^{+0.002}_{-0.002}$	$^{+0.019}_{-0.020}$	$^{+0.002}_{-0.001}$
Volume	$^{+0.057}_{-0.057}$	$^{+0.057}_{-0.057}$	$^{+0.029}_{-0.029}$
n capture	$^{+0.000}_{-0.000}$	$^{+0.000}_{-0.000}$	$^{+0.100}_{-0.100}$
Total	$^{+0.096}_{-0.096}$	$^{+0.090}_{-0.089}$	$^{+0.108}_{-0.114}$

Table 10.4: Systematic uncertainties on derived fluxes.

Variable	Φ_{CC}/Φ_{NC}	Φ_{CC}/Φ_{ES}
E_0	$^{+0.113}_{-0.100}$	$^{+0.019}_{-0.018}$
σ_E	$^{+0.033}_{-0.037}$	$^{+0.008}_{-0.010}$
R^3	$^{+0.001}_{-0.000}$	$^{+0.000}_{-0.001}$
α_M	$^{+0.001}_{-0.001}$	$^{+0.034}_{-0.037}$
β_M	$^{+0.000}_{-0.001}$	$^{+0.012}_{-0.014}$
β_S	$^{+0.000}_{-0.000}$	$^{+0.022}_{-0.021}$
Volume	$^{+0.027}_{-0.027}$	$^{+0.000}_{-0.000}$
n capture	$^{+0.100}_{-0.100}$	$^{+0.000}_{-0.000}$
Total	$^{+0.157}_{-0.149}$	$^{+0.047}_{-0.050}$

Table 10.5: Systematic uncertainties on derived flux ratios.

be

$$\Phi_{CC} = 1.61\ ^{+0.08}_{-0.08}\ \text{(stat)}\ ^{+0.15}_{-0.15}\ \text{(syst)}\ \pm 0.10\ \text{(theor)} \times 10^6 \text{cm}^{-2}\text{sec}^{-1} \quad (10\text{-}1)$$

$$\Phi_{ES} = 2.13\ ^{+0.36}_{-0.38}\ \text{(stat)}\ ^{+0.19}_{-0.19}\ \text{(syst)}\ \pm 0.02\ \text{(theor)} \times 10^6 \text{cm}^{-2}\text{sec}^{-1} \quad (10\text{-}2)$$

$$\Phi_{NC} = 6.74\ ^{+0.79}_{-0.80}\ \text{(stat)}\ ^{+0.91}_{-0.88}\ \text{(syst)}\ \pm 0.40\ \text{(theor)} \times 10^6 \text{cm}^{-2}\text{sec}^{-1} \quad (10\text{-}3)$$

where the uncertainties labelled (theor) are due to uncertainties in the interaction cross-sections.

We can also express these fluxes as ratios to the model predicted values, where we find

$$[\mathrm{CC}] = 0.31\ ^{+0.02}_{-0.02}\ (\mathrm{stat})\ ^{+0.03}_{-0.03}\ (\mathrm{syst})\ \pm 0.07\ (\mathrm{theor}) \tag{10-4}$$

$$[\mathrm{ES}] = 0.41\ ^{+0.07}_{-0.07}\ (\mathrm{stat})\ ^{+0.04}_{-0.04}\ (\mathrm{syst})\ \pm 0.08\ (\mathrm{theor}) \tag{10-5}$$

$$[\mathrm{NC}] = 1.31\ ^{+0.15}_{-0.16}\ (\mathrm{stat})\ ^{+0.18}_{-0.17}\ (\mathrm{syst})\ \pm 0.27\ (\mathrm{theor}) \tag{10-6}$$

We note that the neutral current flux is consistent with the standard model values, while the charged current flux is not. In the context of neutrino oscillations useful measures are the ratios of the fluxes measured through the different reactions. In the case of no neutrino oscillations this ratio is unity. We find for the ratios of charged current to neutral current reactions

$$[\mathrm{CC}]/[\mathrm{NC}] = 0.24\ ^{+0.03}_{-0.03}\ (\mathrm{stat})\ ^{+0.04}_{-0.04}\ (\mathrm{syst})\ \pm 0.002\ (\mathrm{theor}), \tag{10-7}$$

and for charged current to elastic scattering

$$[\mathrm{CC}]/[\mathrm{ES}] = 0.76\ ^{+0.13}_{-0.14}\ (\mathrm{stat})\ ^{+0.04}_{-0.04}\ (\mathrm{syst})\ \pm 0.05\ (\mathrm{theor}). \tag{10-8}$$

Both of these ratios provide direct evidence for neutrino oscillations. Although the ratio of [CC]/[ES] measured with SNO deviates from unity, the uncertainty in this measurement is rather large, due mostly to statistical uncertainty in the ES measurement. We can directly compare the solar neutrino flux measured with the CC reaction in SNO to that measured with the Super-Kamiokande detector through electron scattering, where we again expect a ratio of unity in the case of no neutrino oscillations. We find that Comparison to Super-Kamiokande:

$$[\mathrm{CC}]_{\mathrm{SNO}}/[\mathrm{ES}]_{\mathrm{SK}} = 0.67\ ^{+0.04}_{-0.04}\ (\mathrm{stat})\ ^{+0.08}_{-0.08}\ (\mathrm{syst})\ \pm 0.04\ (\mathrm{theor}) \tag{10-9}$$

This result also disagrees with the no-oscillations hypothesis by many standard deviations. The statistical $s\sigma$ confidence intervals defined by equation 9-23 are shown in figures 10.15 and 10.16. We see that our measurement in the [CC]-[NC] plane lies about 6σ from the line [CC] = [NC]. Our measurement in the [CC]-[ES] plane lies about 1.5σ from the line [CC]=[ES] since we are limited by the statistics of our ES signal.

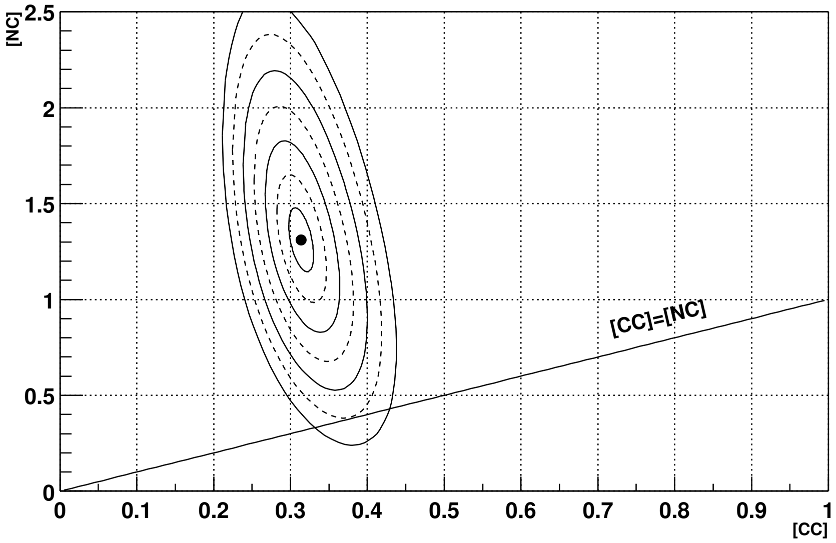

Figure 10.15: Statistical confidence intervals in the [NC] versus [CC] plane. Shown are the fit result (circular marker) and the 1σ to 7σ confidence intervals. The line [CC]=[NC] intersects the 6σ confidence region.

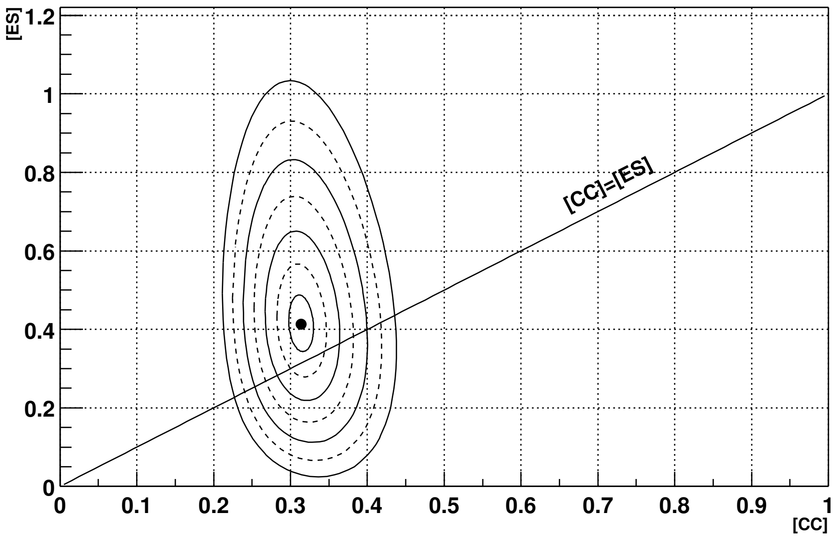

Figure 10.16: Statistical confidence intervals in the [ES] versus [CC] plane. Shown are the fit result (circular marker) and the 1σ to 7σ confidence intervals. The line [CC]=[ES] intersects the 1.5σ confidence region.

10.3 Cross-Checks

To verify that the fit results do not depend on the precise selection of the imposed cuts we have repeated the signal extraction through minimization of equation 9-22 for a range of fiducial volume cuts, angular bins, and energy thresholds. Figure 10.17 shows the extracted fluxes (as ratios of the standard model predictions) for energy thresholds ranging from 5 to 8 MeV. We find that the results are relatively insensitive to the energy threshold near 6 MeV. The large uncertainties for the NC flux for higher energy thresholds is due to the fact that the NC signal decreases rapidly with increasing threshold. Figure 10.18 shows the fit results for a fiducial volume cut ranging from 10% to 100% of the heavy water volume, where again we find that the results are insensitive to the cut used. The data were also divided into four $\cos\theta_r$

bins, and the minimization repeated for each bin. We find the results consistent within each of the four bins, as shown in figure 10.19. We are thus confident that the extracted solar neutrino fluxes are independent of the precise cuts used to the select the data for analysis.

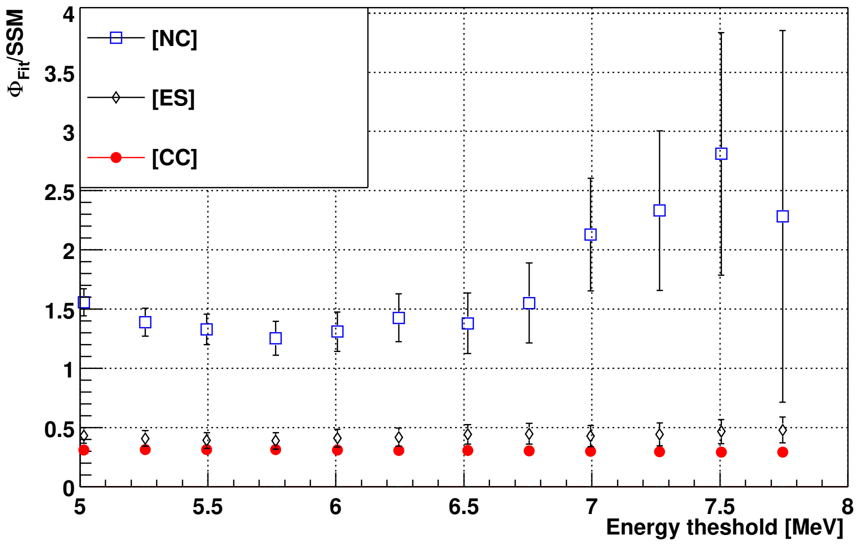

Figure 10.17: Variation of fit result with energy thresholds. The results are not dependent on the energy threshold near the analysis threshold of 6 MeV. The effects of the rapidly decreasing NC signal with energy are seen for energies greater than about 6.5 MeV, where uncertainties on the NC flux increase due to a decreased number of events in the data set.

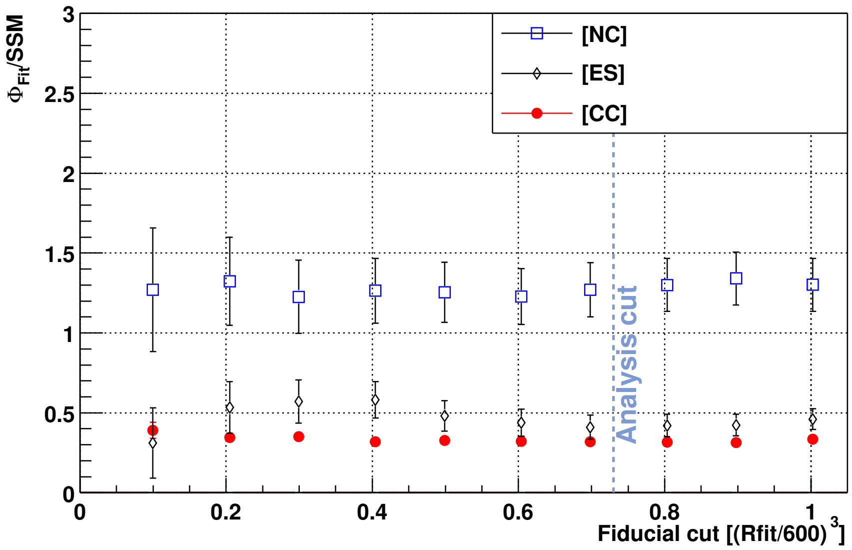

Figure 10.18: Variation of fit result with fiducial volume cut. The results are consistent for various fiducial volume cuts.

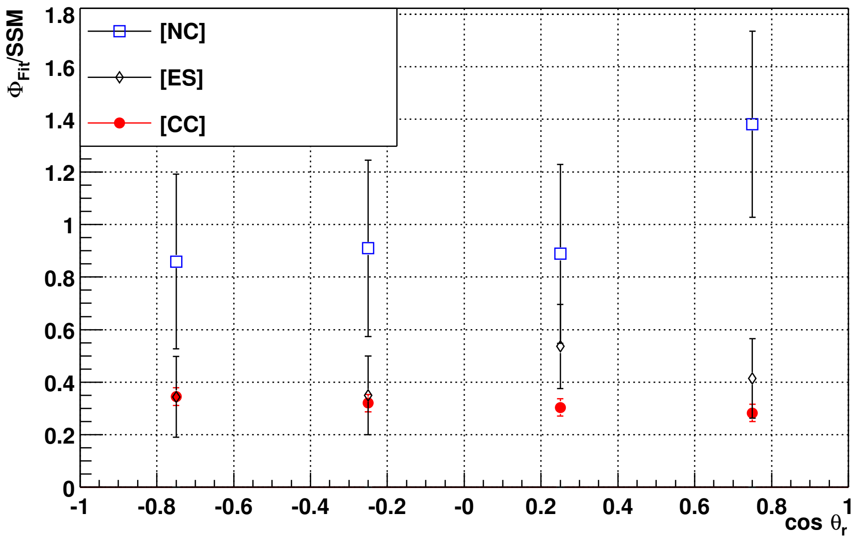

Figure 10.19: Variation of fit result with event direction ($\cos\theta_r$).

Chapter 11

Conclusion

Techniques for analysis of the solar neutrino signals in SNO have been presented and a subset of the first SNO production data has been analyzed, from which we can draw several conclusions.

The ^{8}B solar neutrino flux has for the first time been measured with a heavy water target. The measured fluxes for each of the three neutrino reactions possible in SNO are

$$\begin{aligned}
\Phi_{CC} &= 1.61\ ^{+0.08}_{-0.08}\ \text{(stat)}\ ^{+0.15}_{-0.15}\ \text{(syst)}\ \pm 0.10\ \text{(theor)} \times 10^6 \text{cm}^{-2}\text{sec}^{-1} \\
\Phi_{ES} &= 2.13\ ^{+0.36}_{-0.38}\ \text{(stat)}\ ^{+0.19}_{-0.19}\ \text{(syst)}\ \pm 0.02\ \text{(theor)} \times 10^6 \text{cm}^{-2}\text{sec}^{-1} \\
\Phi_{NC} &= 6.74\ ^{+0.79}_{-0.80}\ \text{(stat)}\ ^{+0.91}_{-0.88}\ \text{(syst)}\ \pm 0.40\ \text{(theor)} \times 10^6 \text{cm}^{-2}\text{sec}^{-1},
\end{aligned}$$

or expressed as a ratio to the standard model predictions

$$
\begin{aligned}
[\mathrm{CC}] &= 0.31 \,^{+0.02}_{-0.02}\ (\mathrm{stat}) \,^{+0.03}_{-0.03}\ (\mathrm{syst}) \ \pm 0.07\ (\mathrm{theor}) \\
[\mathrm{ES}] &= 0.41 \,^{+0.07}_{-0.07}\ (\mathrm{stat}) \,^{+0.04}_{-0.04}\ (\mathrm{syst}) \ \pm 0.08\ (\mathrm{theor}) \\
[\mathrm{NC}] &= 1.31 \,^{+0.15}_{-0.16}\ (\mathrm{stat}) \,^{+0.18}_{-0.17}\ (\mathrm{syst}) \ \pm 0.27\ (\mathrm{theor})
\end{aligned}
$$

The fact that the measured flux depends on the reaction is direct evidence for more than a simple electron neutrino flux. The neutral current flux, which is independent of neutrino flavor is consistent with the current solar model prediction of $\Phi_{SSM} = (5.15 \pm 1.03) \times 10^6$ cm^{-2} sec^{-1} to within 1σ while the charged current measurement is not. This first flavor-independent measurement of the ^{8}B solar neutrino flux along with the charged current flux measurement is direct evidence for weak flavor mixing.

We can also note that the ^{8}B flux measurements made by SNO are in agreement with the other charged current and elastic scattering measurements,

$$
\begin{aligned}
[\mathrm{CC}]_{Homestake} &= 0.33 \pm 0.02\ (\mathrm{stat}) \pm 0.02\ (\mathrm{syst}) \\
[\mathrm{ES}]_{SuperK} &= 0.465 \pm 0.005\ (\mathrm{stat})^{+0.015}_{-0.013}\ (\mathrm{syst})
\end{aligned}
$$

made with the Homestake [2] and Super-Kamiokande [6] detectors.

In the next phase of the SNO experiment salt (NaCl) will be added to the D_2O to increase the sensitivity to neutrons. In this phase a precise neutral current measurement will allow sensitive tests of the neutrino oscillation (MSW) model and detailed probing of the mixing parameters.

Bibliography

[1] John N. Bahcall and Jr. Raymond Davis. *Millenium Essay in PASP*, 112:429–433, 2000.

[2] B. T. Cleveland et al. *Astrophysics Journal*, 496:505, 1998.

[3] J. N. Abdurashitov et al. *Phys. Rev. C*, 60(055801), 1999.

[4] W. Hampel et al. *Phys. Lett. B*, 447:127, 1999.

[5] Y. Fukuda et al. *Phys. Rev. Lett.*, 77(9):1683–1683, 1996.

[6] Y. Suzuki. Talk at XIX international conference on neutrino physics and astrophysics, Sudbury, Canada, June 2000.

[7] S.P. Mikheyev and A. Yu. Smirnov. *Nuovo Cimento*, 9C(17), 1986.

[8] L. Wolfenstein. Neutrino oscillations in matter. *Physical Review D*, 17(9), 1978.

[9] The Super-Kamiokande Collaboration. *Phys. Rev. Lett.*, 81:1562–1567, 1998.

[10] John N. Bahcall. *Neutrino Astrophysics.* Cambridge University Press, Cambridge, 1989.

[11] S.A. Bludman, N. Hata, D.C. Kennedy, and P.G. Langacker. *Physical Review D*, 47(6), 1993.

[12] M. C. Gonzalez-Garcia. *Nucl. Phys. Proc. Suppl.*, 95:100–107, 2001.

[13] M. C. Gonzalez-Garcia et al. *Phys. Rev. D*, 63:33005, 2001.

[14] John N. Bahcall et al. *Phys. Lett. B*, 477:401–409, 2000.

[15] John N. Bahcall, Sarbini Basu, and M. H. Pinsonneault. *Physics Letters B*, 433(1):1–8, 1998.

[16] The SNO Collaboration. *Nucl. Inst. Meth.*, A449:172–207, 2000.

[17] Bryce Moffat. *Optical Calibration of SNO.* PhD thesis, Queens' University, Kingston, Ontario, Canada, 2001.

[18] André Stephane Hamer. *Energy Calibration of SNO for Measurement of the Charged-Current Neutrino Reaction.* PhD thesis, Queen's University, Kingston, Ontario, Canada, 1999.

[19] Phil Harvey. XSNOED SNO event display software, 2001. Queen's University.

[20] Chris Jillings. *The Electron-Scattering Reaction in the Sudbury Neutrino Observatory.* PhD thesis, Queens' University, Kingston, Ontario, Canada, 1999.

[21] Michael David Lay. *Creation and Detection of Čerenkov Light in the Sudbury Neutrino Observatory.* PhD thesis, Oxford University, 1994.

[22] J.J. Simpson and J.-X. Wang. Determination of NC/CC ratio during the pure D_2O stage of operation. Report SNO-STR-98-001, University of Guelph, 1998.

[23] J.J. Simpson and J.-X. Wang. Determination of NC/CC ratio and CC shape during the pure D_2O stage of operation. Report SNO-STR-98-002, University of Guelph, 1998.

[24] Judith F. Briesmeister. *MCNP (tm) – A General Monte Carlo N-Particle Transport Code.* Los Alamos National Laboratory, 2000. Report LA-13709-M.

[25] H-P Wellisch et al. *GEANT4 Physics Reference Manual.* CERN, 2000. On-line documentation is available at http://wwwinfo.cern.ch/asd/geant4.

[26] P.F. Rose. *ENDF/B-VI: Cross Section Evaluation Working Group, ENDF/B-VI Summary Document.* National Nuclear Data Center, Brookhaven National Laboratory, 1991. Report BNL-NCS-17541 (ENDF-201).

[27] Ekstrom S.Y.F. Chu, L.P and R.B. Firestone. WWW table of radioactive isotopes, 2000.

[28] J.F. Wild et al. *Phys. Rev. C*, 41(2):640–646, 1990.

[29] George Ewan. Source strength of ^{252}Cf calibration neutron sources by gamma counting. SNO Internal Report, Queen's University, 2001.

[30] A. Lajtai et al. *Nucl. Inst. Meth.*, A293:555–561, 1990.

[31] Richard James Ford. *Calibration of SNO for the Detection of ^{8}B Neutrinos.* PhD thesis, Queen's University, Kingston, Ontario, Canada, 1998.

[32] Josh Klein. Data cleaning : An analog measurement board cut. SNO Internal Report, University of Pennsylvania, Aug. 1999.

[33] Xin Chen. *Monte Carlo Simulations and Analyses of Backgrounds in the Sudbury Neutrino Observatory.* PhD thesis, University of Oxford, 1997.

[34] Mark Chen. Bifurcated analysis 2.0. SNO Internal Report, Queen's University, Feb. 2001.

[35] Jacques Farine and Henry Lee for the SNO water group. Results of SNO water assays. Results prented at Nu2000 conference, 2000.

[36] SNO collaboration. Sudbury Neutrino Observatory Proposal, 1987.

[37] SNO collaboration. Design specifications for the Mark II SNO detector, 1989.

[38] Peter Skensved and Barry Robertson. Summary of backgrounds in SNO. Report SNO-STR-94-13, Queen's University, 1994.

[39] Davis Earle, Ron Deal, and Earl Gaudette. Polycast acrylic sheets. Report SNO-STR-93-42, Sudbury Neutrino Observatory, 1993.

[40] Hugh Evans. Acrylic dust tape lift results. personal communication, 2000.

[41] Matthew Jeremy Lyon. *Neutron transport in the Sudbury Neutrino Detector*. PhD thesis, Balliol College, Oxford University, 1996.

[42] C. W. Nally. Atmospheric neutrino induced backgrounds in the solar neutrino energy range. SNO Internal Report, University of British Columbia, August 2000.

[43] Nathaniel Tagg. *The ^{8}Li Calibration source and through-going muon analysis in the Sudbury Neutrino Observatory*. PhD thesis, University of Guelph, Guelph, Ontario, Canada, 2001.

[44] Nathaniel Tagg. Data cleaning : The muon tag. SNO Internal Report, University of Guelph, Nov. 1999.

[45] A. D. Marino. Muon-induced spallation products in the SNO detector. SNO Internal Report, Lawrence Berkely National Laboratory, May 2000.

[46] K. Kubodera and S. Nozawa. *Int. J. Mod. Phys.*, E3, 1994.

[47] S. Ying, W.C. Haxton, and E.M. Henly. *Physical Review C*, 45, 1992.

[48] G. 't HOOFT. *Physics Letters B*, 37(2), 1971.

[49] J. Bartels et al. Review of particle physics. *The European Physics Journal C*, 15, 2000.

[50] Louis Lyons. *Statistics for nuclear and particle physicists.* Cambridge University Press, Cambridge University, Great Britain, 1992.

[51] F. James. *MINUIT – Function Minimization and Error Analysis.* CERN Computing and Networks Division, Geneva, Switzerland, 1998.

[52] Mark G. Boulay. QSNO : An object oriented package for manipulation and analysis of SNO data. SNO Internal Report, Queen's University, 2001.

Curriculum Vitae

Name:	Mark G. Boulay
Place and Year of Birth:	Sturgeon Falls, Ontario, 1971
Education:	Laurentian University, 1990-1996 B.Sc. (Honours, Physics) 1994 M.Sc. (Applied Physics) 1996 Queen's University, 1996-2001 (PhD)
Experience:	Teaching Assistant, Physics Department, Laurentian University, 1993-1996 Teaching Assistant and Laboratory Demonstrator, Physics Department, Queens University 1996-2000
Awards:	Ontario Graduate Scholarship, 1994 and 1995 Natural Sciences and Engineering Research Council (NSERC) scholarship for doctoral studies, 1996-1998
Publications:	"The Sudbury Neutrino Observatory", Nucl. Inst. Meth. A449 172-207, 2000